SUPPORTING INFORMATION

Table of content:

---

1 SI Experimental Procedures

1.1 Methods

1.1.1 Experimental conditions

We performed the experiments over 5 to 14 days following electrode implantation surgery while patients were undergoing 24-hours/day seizure monitoring. Experimental data were recorded simultaneously with clinical data from separate electrodes. In the following sections, we refer to a day of consecutive recordings as a 'recording session' and to one virtual navigation trial played in a given environment as a 'game'. Each recording session took place in the hospital ICU while the patients were awake and fully alert. The patient was sitting or lying in a chair or bed in a dimly lit room in the presence of the experimentalist and an assistant. Recording sessions involved the patients' active participation for between 15 and 30 min.

Our goal was to obtain continuous recordings of single unit activity from the entorhinal cortex (EC) in consecutive days during games played in 4 virtual environments specifically designed for spatial navigation task in four patients implanted by research electrodes. However, we only present data from the two patients who provided complete sessions over consecutive days, while the other two patients provided fragmented data sets not included in this study.

During the research-related recordings the clinical ECoG electrodes were also monitored through a separate clinical recording system for abnormalities. No clinical seizures were experienced during our experimental recordings. Occasional high frequency ripples occurred but in localized frontal areas far from the EC or hippocampal electrodes. They did not affect our recordings.

1.1.2 Behavioral task

Subjects were instructed to perform a virtual navigation task presented as a game on a tablet PC. The game's repeated objective was to 1) find a randomly placed space alien, holding either a blue or yellow briefcase, and to 2) drop off each alien at a spaceship matching the briefcase's color (Supplemental Video).

The game encouraged active engagement and provided the user with a measure of relative success by displaying a counter of the number of aliens returned (out of a set goal of 40) along with a timer. Timely completion of the tasks required maintaining memory of object identity (color of briefcase) and location (of the target spaceships). However, we usually terminated recordings after 5 min to ensure that all four environments could be played within the 30-minute time frame of uninterrupted patient availability. Exceptions to this occurred when we opted to increase trajectory coverage of an environment by allowing a game to be played for 10 minutes. The game environments were played in random order in each recording session. We occasionally performed cross-validations on neurons by repeating a game in the same environment non-consecutively during the same session.

1.1.3 Game control

The task was performed on a tablet PC (ASUS Transformer 201 running Android 4.0 at 1280 x 800-pixel resolution). Subjects maneuvered by pressing a "GO" button with their left thumb and controlled direction by pressing either a "LEFT" or "RIGHT" button with their right thumb. Before experimental data was collected, subjects were allowed to practice playing the game until they were accustomed to the game controls. The subjects' virtual trajectory and heading (relative to the N-S axis in each game environment) were recorded.

1.1.4 Virtual reality environments

The virtual reality environments were designed using Unity 3D (version 3.5.6.) and were compiled for Android 4.0. The game rendered the 3D environment from the player's point of view. The player was constrained to the flat ground surface of each map and their movement speed was a constant 5 m/s, unless the "GO" button was released or an obstacle inhibited movement.

1.1.5 Properties of environments

Virtual navigation was simulated in four environments: Backyard (BY), Louvre (LV), Luxor (LX) and Open Space (OS). The dimensions of the environments in virtual meters ranged from 18 x 18 to 70 x 70 (specific dimensions given in Supplemental Table 1.1 along with other relevant parameters). No shadows were rendered in order to minimize absolute directional cues. The geometry of and sample views from the four environments are depicted in Fig. S1. On all maps except OS, a skybox with a sun, mountains and clouds (generated by Terragen, Planetside Software, UK) simulated the outside environment and provided distant spatial cues.

- *Backyard:* The backyard was a relatively small (18 x18 m), square area bounded by a shed and tall stone walls. A mountain-covered terrain was visible over the walls, providing distant spatial cues. The ground was covered with a repetitive grassy pattern.

- *The Louvre:* Modeled after one of the Louvre's courtyards, the navigation area was confined by the three walls of a U-shaped building and a pedestal with a fence. This was the only rectangular environment (50 x 70 m). The ground was randomly patterned with irregularly shaped blocks.
- *The Luxor:* This environment was a relatively large (52 x 52 m), square-shaped indoor space modeled after the ancient temple in Luxor, Egypt. The space was enclosed by walls on all four sides and by a ceiling above. A single large opening in one wall revealed the outside scenery but acted only as a visual cue and not as an exit path. More importantly, 36 equidistantly spaced pillars obstructed the navigable space and obscured the player's view. The floor was covered with a sand-like texture (Supplemental Video).
- *Open Space:* This environment served as a control with minimal external cues. It was a desert-like, flat environment with a boundless horizon and no landmarks other than the two target space ships. The sky was rendered a uniform blue, devoid of any spatial cues. An irregular and dried out texture patterned the ground. The area of possible alien placement, a 70 x 70 m square, was the largest among the four environments.

1.1.6 Alignment of environments

Since the rectangular edges of the bounded environments (BY, LV, LX) and the spaceships in the OS environment were all aligned to the North-South axis, the orientation of the player in the game was quantified relative to these axes for analysis. For all recording sessions and virtual navigation trials, the game always started with the player's invisible avatar facing 60° from 0 on the XY analysis plane. The subjects' orientation relative to the hospital room was also unchanged. This consistency of starting-view orientation in each game allowed us to compare grid orientation across different environments within the same recording session as well as in the same environment across different days.

1.1.7 Surgical procedures and electrode implantation and deplantation

We recorded wide-band signals from no deeper than layer II-III (given the < .8 mm tissue penetration and the average 5 mm cortical thickness of human EC, though lacking histological verification) of the EC using AD-TECH macro/micro subdural electrodes and PMT micro-wire plugin arrays (Catalog code: CMMS-22PX-F478 and 2112-00-18-004, respectively), custom made per our specifications (Fig. 1A). The microelectrodes were made of 35 μm platinum iridium wires that were arranged in 4 groups of 2 x 2 wire grids cut to .8 mm length from the electrode base and with nominal impedance < 3 MOhm. The craniotomy and electrode implantations were performed under general anesthesia. After craniotomy, the electrodes were inserted subdurally to the surface of the entorhinal cortex by the neurosurgeon with stereotactic control. The dura was hermetically closed in a watertight fashion and the bone flap was reattached. The patient remained in the hospital ICU under continuous epilepsy monitoring for 5 to 14 days following the surgery. After sufficient evidence for seizure origin had been collected, electrode explantation and surgical resection of the seizure foci were performed under general anesthesia.

1.1.8 Experimental subjects

The diagnoses of the four subjects from whom we obtained entorhinal cortical recordings can be found in Supplemental Table 1.2. Only two patients (subject H and subject K) yielded stable, high quality recordings over consecutive days.

1.2. Data analysis

1.2.1 Synchronizing spatial navigation with neuronal data logging

The subjects' navigation data, recorded on the tablet, was associated with the neuronal data by sending a 25 ms duration square wave from the tablet's audio output port to the analog auxiliary input port of the data acquisition system each time the "START" button for the game was released. The precision of data synchronization between the tablet and the neuronal data logging was < 20 ms (SD=18 ms). This resulted in a spatial localization error of less than 25 cm virtual distance ($< .48\%$ of average map width).

1.2.2 Recording neuronal data

Sixteen microelectrodes were implanted in the medial entorhinal cortex of the right temporal lobe for both patients. Signals were recorded from five microelectrodes at 24 kHz sampling frequency using an FHC Guideline 4000 system, an FDA approved amplifier for neuronal data acquisition in the human brain. The 5 electrodes varied across the days and were selected before the recording session based on the largest amplitude and best single unit isolation. The 5 or 10 min traces were band-pass filtered (300 to 6,000 Hz) by using a noncausal elliptic filter off-line. Because we selected 5 out of 16 electrodes with the highest unit activity each day before data logging we are unable to claim identity of single units across different days. Nevertheless, because the electrodes were unlikely to move, some of the cells we recorded across multiple days might be the same neurons. Therefore, the total number of cells recorded is probably an overestimation of the independent neurons in our sample.

1.2.3 Spike detection

We applied WaveClus off-line spike detection and spike sorting (Fig. S2) (1). Spike detection was followed by isolation of single-unit activity using an unsupervised spike-sorting method . For spike detection we applied a threshold fitted to the median standard deviation of the data (1):

$$Thr = 4\sigma_n; \qquad \sigma_n = median\left\{\frac{|x|}{0.6745}\right\}, \qquad (1.2.3.1)$$

where x is the bandpass-filtered signal and σ_n is an estimate of the standard deviation of the background noise. In cases when the amplitude nthreshold did not provide a clear separation between spikes and multiunit activity, the multiunit contamination generated a large “noise cluster” in the wavelet coefficient space at near zero amplitude. This isolated noise cluster enabled us to separate single unit clusters from noise with high confidence (example Figs. S10-28). We only included single unit activity in our dataset that was unambiguously distinct from the noise cluster (Figs. S12-16 and S18-28) or unambiguously separable from each other (Figs. S2, S5, S17).

1.2.4 Spike sorting

Spikes different from noise were sorted using an enhanced version of the WaveClus algorithm that uses superparamagnetic clustering as a non-parametric classifying engine (Fig. S2) (1). WaveClus is the second most popular semi-supervised method worldwide, used by more than 110 publications and the most efficient among the benchmarked spike sorting methods (2). The wavelet transform is defined as the convolution between the signal *x(t)* and a Haar wavelet functions $\psi_{a,b}(t)$,

$$W_\psi X(a,b) = x(t)|\,\psi_{a,b}(t), \qquad (1.2.4.1)$$

where $\psi_{a,b}(t)$ are dilated (contracted), and shifted versions of a unique wavelet function $\psi(t)$,

$$\psi_{a,b}(t) = |a|^{-\frac{1}{2}}\psi\left(\frac{t-b}{a}\right), \qquad (1.2.4.2)$$

where *a* and *b* are the scale and translation parameters, respectively. We used a computational shortcut that accelerated the computation of wavelet coefficients. Finally, we obtained 12 wavelet coefficients and reduced those to 4 dimensions with the highest multimodality and deviation from normal distribution. These were the dimensions best discriminating the spikes in wavelet coefficient space. Each spike was associated with a combination of these *k* most informative wavelet coefficients, hence represented by a point in the *k*-dimensional space. The data using superparamagnetic clustering resulted in clusters associated with spikes of similar waveforms, where $k=12$ for all present datasets. The spike times of classified waveforms were tested against 4 ms refractoriness before associated with putative neurons. We only included neurons where the Mahalanobis distance between noise cluster and single unit cluster and between single unit clusters were $x > 20$. We refer to these single unit clusters as ‘neurons’ (Fig. S2). Spike times were rounded to the nearest 1 ms interval and expressed in 1 ms precision.

1.2.5 Validation of stability and quality of spike sorting

Spike waveforms were extracted from the *continuous signal* recorded from 5 microelectrodes, which comprised the navigation epochs in all different environments presented on a given day. If the recording started at T_0, then the first, second third and fourth game started at T_1, T_2, T_3 and T_4, respectively, and each ended at $T_i+5\ min$. The complete session ended at T_5. We performed the spike sorting between the entire T_0-T_5 interval (20-30 min), and associated the games with the spike trains between T_1, T_2, T_3 and T_4 after spike sorting. Hence, spike sorting artifacts due to electrode movement and confusion of spike cluster identifiers across environments were ruled out. To support this claim and verify stability of spike sorting and identity of single units across different environments we tracked the quality of unit isolation and neuronal identity across recordings of different environments each day. Figure S2 illustrates the integrity (stability and consistency) of waveform classification across environments.

In addition, in 3 sessions (one day for subject H and two days for subject K) we played the same 5 min game twice with a 10-minute separation and recorded the activity of the same neurons in the same virtual environment twice during the same recording session. This allowed for cross-validation between the spatial firing fields of the isolated neurons (Fig. S5). We observed a satisfactory consistency with respect to both single unit waveforms and their spatial mapping on the environments.

1.3. Computational methods

1.3.1 Computing head direction

By analyzing each cell's average firing rate versus head direction (in 5° bins), we assessed the direction-tuning of neurons in each environment. We computed the Resultant vector length, the mean direction and Rayleigh's test for non-uniformity. We classified a neuron as direction-tuned when $p_{Rayleigh} < .05$.

1.3.2 Construction of spatial mapping of single unit activity

The navigation data stored by the tablet consisted of the player's trajectory (X and Y coordinates, and head direction) and a time-stamp so that any deviations from the intended 500 Hz sampling frequency could be accounted for. The trajectory data was interpolated up to 1 kHz to match the 1 ms precision of spike times. After synchronizing the virtual trajectory data with the neuronal data (Supplemental Experimental Procedures 1.2.1), spikes of putative neurons were projected onto the navigation area according to the player's location at the time of each spike (Supplemental Video).

1.3.3 Spatial firing rate maps and Autocorrelation (AC)

To identify topographically consistent firing fields before characterizing their spatial coherence, it was necessary to create a spatial firing rate map and compute its autocorrelation. For the firing rate map, the game area was binned into 1 x 1, 2 x 2 or 3 x 3 m areas, depending on the virtual environment (Supplemental Table 1), and the average firing rate was computed within each tile. Binning had no significant effect on the grid parameters (Fig. S34). This was accomplished by dividing the number of spikes occurring within each bin by the time spent within it. To compute the autocorrelation, the firing rate map was first smoothed with a Gaussian filter (5 x 5 bin neighborhood, sigma=.8) and unvisited bins were assigned a firing rate of 0. Autocorrelograms were computed as follows. Given that the original firing rate map is (*f*) and the number of overlapping bins between the original and shifted firing rate maps at a given τ_x, τ_y offset is *n*, the equation for the two-dimensional discrete autocorrelation is

$$r(\tau_x, \tau_y) = \frac{n\sum f(x,y) f(x-\tau_x, y-\tau_y) - \sum f(x,y) f(x-\tau_x, y-\tau_y)}{\sqrt{n\sum f(x,y)^2 - (\sum f(x,y))^2}\sqrt{n\sum f(x-\tau_x, y-\tau_y)^2 - (\sum f(x-\tau_x, y-\tau_y))^2}}, \qquad (1.3.3.1)$$

where $r(\tau_x, \tau_y)$ is the autocorrelation. Correlations were estimated for all values of *n*. The central peak of the autocorrelogram was removed by before computing the gridness (3, 4).

1.3.4.1 Quantifying "gridness" (gridness score)

We quantified canonical "gridness" based on the autocorrelograms (ACs) by computing a 60° gridness score (***g***) step-by-step following the exact procedure outlined by Barry et al (5), Sargolini et al (6) and Krupic et al (7) as illustrated in Fig. S3D. We first normalized the firing-rate maps by the sizes of environments that allowed for equal spatial resolutions for the ACs of different environments, but we kept the aspect ratio differences. Next, we computed the 2-dimensional ACs by applying 2D cross-correlation to the firing-rate maps (Fig. S3B). After centering and clipping the AC to a 100 x 100 matrix, we located the largest peak after the removal of central peak, which defined a concentric ring containing the circular or ellipsoid arrangement of the first set of autocorrelation peaks at radius *R*. The outer radius of the ring was, based on the BK method, chosen to be 2.5**R* (5, 7) (Fig. S3C). For the computation of gridness scores we followed the method by Sargolini et al (6). Accordingly, we filtered the AC with the above-defined ring. Then we rotated the extracted ring from 1 to 180°, and computed the Pearson's correlation coefficients $\overline{r_{1^\circ \ldots 180^\circ}}$ between the original and rotated matrix with an 8-point moving average applied to it (Fig. S3D). We determined gridness (***g***) as the difference between the minimum of r_{60° *or* r_{120° and the maximum of r_{30°, r_{90° or r_{150°. This function of gridness assumed a 60° modulation of AC as it expresses the modulation depth relative to 60° rotation symmetry. Because *r*-modulation was limited between 0 and 1, ***g*** was bounded between 0 and 1, inclusive.

1.3.4.2 Quantifying "general spatial periodicity" (*gsp* score)

In addition to gridness, we also defined a "general spatial periodicity" score (*gsp*) by computing the depth of modulation of the correlation between the original and the rotated ACs at a broader range or rotations that captured any rotational symmetry between 10° and 90°. Technically, instead of taking the minimum r at predefined angles, as in Barry et al. (5) and Sargolini et al. (6) outlined in 1.3.4.1, we quantified the modulation depth of spatial periodicity over 1° to 90° of rotations on the $\overline{r_{10°\ldots90°}}$ curve (Fig. S3D). We computed *gsp* score as the difference between the first >0° positive peak and the first negative peak of of $\overline{r_{10°\ldots90°}}$ and located the positive peak in angle space (γ). The angle providing the best registration of AC peaks between the original and the rotated AC defined the rotational symmetry of AC. The difference between r_{+peak} and r_{-peak} served as the general spatial periodicity score *gsp* (Fig. S3D). Because r-modulation was limited between 0 and 1, *gsp* was also bounded between 0 and 1, inclusive. This allowed for the detection of a broader range of grid geometries beyond hexagonal.

1.3.5 Statistical validations

1.3.5.1 Statistical validation of gridness scores by Poisson spike processes

In order to statistically validate each cell's gridness score ($\boldsymbol{g}$) with a known confidence we determined the confidence interval ($\boldsymbol{g}_{conf}$) for each cell individually based on Monte Carlo randomization of the cell's own original spike trains. With a set confidence level (5%) we could determine whether a given gridness parameter ($\boldsymbol{g}$) can be drawn from the spatial configuration of Poisson spike processes (H_0) or, alternatively, from a configuration that is spatially-periodically clustered with 60° rotational symmetry (H_1). To allow a margin of $p < .05$ probability for false positives, we compared each cell's $\boldsymbol{g}$ with the 95 percentile of the distribution of $\boldsymbol{g}_{RND}$ computed from 1,000 randomized spike trains derived from the original single unit activity. The randomization was done by random assignment of every spike to a randomly chosen different time during the navigation in that specific environment with 1 ms precision by also paying attention to preserving the original inter-spike-interval statistics. We computed individual $\boldsymbol{g}_{RND}$ values for each surrogate spike train. The 95 percentile of the distribution of 1,000 $\boldsymbol{g}_{RND}$ values provided the confidence limit ($\boldsymbol{g}_{conf}$) at which the likelihood that a $\boldsymbol{g}$ score was considered different from a random process while it was drawn from a distribution of random spike times was exactly .05. If the actual $\boldsymbol{g}$ was larger than $\boldsymbol{g}_{conf}$, then we accepted H_1 with a confidence of $p < .05$ and concluded that the spike train was generated by a spatially controlled process (Fig. S3E).

The same procedure was applied to test the significance of general spatial periodicity (*gsp*), but instead of computing $\boldsymbol{g}_{RND}$ from the randomized spike trains we computed gsp_{RND}.

1.3.5.2 Statistical validation of gridness scores by theta modulated and directionally tuned spike process

In addition to the validation of gridness scores by Poisson spike processes (**1.3.5.1)**, we constructed random spike trains from specific physiologically constrained distributions. Entorhinal cortical neurons exhibit temporal modulation by theta (4-7 Hz) and intrinsic subthreshold membrane potential oscillation at alpha (8-15 Hz) frequency bands (8–10). They also display various degrees of directional tuning. In order to rule out that the observed spatially periodic activity statistically emerged as a byproduct of theta- or alpha-modulation of firing probability combined with directionally tuned spike process we subjected the gridness scores to a more rigorous validation process. Namely, we constructed surrogate spike trains with temporal periodicity and directional tuning combined. Firstly, we took the original spike train of a neuron (Fig. S4A) and we computed the circular distribution of direction vectors from the typically 5-minute navigation (Fig. S4 B). Next, we reassigned the original spikes to path segments of the navigation that fell within a 15° range centered around a randomly selected direction from the heading direction distribution (Fig. S4C-D). We used the same number of spikes as in the original spike train, hence the overall firing rate of the cells remained unchanged. Next, we dispersed the spikes according to a interspike intervals sampled from a Poisson process (1.3.5.2.1) with λ=200 ms (5 Hz). Then we combined them with spike processes sampled from a Poisson process modulated by λ =83.333 ms (12 Hz).

$$\boldsymbol{f}(\boldsymbol{x}|\lambda) = \frac{\lambda^x}{x!} e^{-\lambda}; x = 0, 1, 2, \dots, \infty. \qquad (1.3.5.2.1)$$

In addition, we introduced burst firing with 5 ms refractoriness, also typical of EC neurons. The combination of these resulted in a complex periodically modulated spike train endowed with directional tuning except spatially coherent periodic activity (Fig. S4). We verified the statistics of the new spike train by autocorrelograms (Fig. S4F,G). finally firing rate maps an autocorrelograms verified the correctness of the statistical procedure.

To obtain confidence intervals for the computed gridness score of each single unit, we generated 1,000 theta/alpha-modulated and directionally tuned spike-trains based on the previously described procedure. The distribution served as a Null to compare the gridness score of the recorded single unit with. The gridness of a single unit in this population was qualified to be significant if it exceeded the upper 95% ($\mu \pm 2\sigma$) of the Null distribution.

1.3.5.3 Statistical validation of spatially periodic processes

In addition to validating each single unit train to its own randomized sequence (1.3.5.1), we generated 1,000 surrogate firing rate maps constructed from a mixture of randomly displaced 2D Gaussians. We carefully modeled random firing rate maps by generating 100 randomly positioned instances of 2D Gaussians with a 2xSD = 5 m. While 100 patches may seem too many, they tend to form clusters by random superposition, most similar to the observed firing rate maps. When the Gaussians overlapped, we merged them to a larger mixed cloud of Gaussians resulting in average 7 +/- 2 clouds typical in the observed firing rate maps. We normalized the Gaussians by the average firing rate of neurons in each environment. We found that the sizes and shapes of mixed Gaussians reproduced the statistics of the observed firing rate maps well. The 50 percentile (median) and 95 percentile of *gsp* scores of the random Gaussian mixture model were at $gsp_{(50)}$= .2400 and $gsp_{(95)}$= .3355, respectively (Fig. S3F).

1.3.5.4 Cross-validation of firing rate maps

The environmental coverage in our experiment was less complete than is typical in similar animal studies (11–13) owning to the clinically constrained 20-30 min recording sessions per day. When an incomplete coverage combines with a low firing rate cell, especially when the navigation paths during the first and the second half of the task are non-overlapping, chances for high spatial covariance of neuronal activity between the two intervals are very low. Despite the overall low firing rate of neurons, the spatial coherence of single spikes was evident from individual examples (Fig. S36). Therefore in our experiment, the method of two-fold cross-validation widely used (11, 14), when dividing the recording time into a first and a second half (in our experiment 2 x 2'30") and computing correlations between the two firing rate maps, was biased toward negative correlations. To manage the inherent bias, we performed two tests for stability, cross-validation and stationarity analysis and applied them on two types of datasets, the SPC and $\mathrm{PGC}_{\text{hi-conf}}$ datasets from both subjects combined. The concordance of two tests are shown in Figure S5F,G.

1.3.5.5 Two-fold cross-validation of firing rate maps

The first type of cross-validation we applied was the standard *k*-fold method of dividing each navigation trial into k non-overlapping and equal-duration segments (in our case *k*=2 leading to two intervals of 2'30") and constructed corresponding firing rate maps from the two spike trains. Without trying to predict the second segment from the first, we computed a 2D correlation between the two firing rate maps:

$$r = \frac{\sum_m \sum_n (A_{mn} - \bar{A})(B_{mn} - \bar{B})}{\sqrt{(\sum_m \sum_n (A_{mn} - A)^2) - (\sum_m \sum_n (B_{mn} - \bar{B})^2)}} \qquad (1.3.5.5.1)$$

where $\bar{A}$ and $\bar{B}$ were the means of A and B firing rate maps, respectively. The distribution of *r* relative to 0 median provided an estimate of the overall stability of grids evident from the firing rate maps.

1.3.5.6 Testing stationarity of firing rate maps

Because of the randomized placement of targets (i.e. space aliens in the game) and incomplete coverage of the environment made navigation paths often uncorrelated between the first and second time intervals, and to gain a confidence on the stability of grid patterns over time, we sought for an alternative method of cross-validation. Since the stability of firing rate distributions is dependent on the stationarity of the underlying spike processes, we tested for stationarity of the firing rate maps as an estimate for temporal consistency of grid patterns. Stationarity is less affected by the low-firing rate of neurons, the uncorrelated trajectories, the relatively short time window (5 minutes) then cross-validation and it does not depend on repeated visits of the same locations of virtual environments. A time series is considered strictly stationary when $\mathbf{X}_1^{k}$ and $\mathbf{X}_t^{t+k-1}$ have the same distribution, for all *k* and *t,* the distribution of blocks of length *k* is time-invariant (15, 16). In our case $\mathbf{X}_1^{k}$ and $\mathbf{X}_t^{t+k-1}$ were matrices of firing rates in the spatial domain. We maximized the overlap of navigation pathways between the two samples by assigning the odd numbered spikes and even numbered spikes to separate groups of spikes (Fig. S37B) and computed the firing rate maps $\mathbf{X}_1^{k}$ and $\mathbf{X}_t^{t+k-1}$ for the two spike groups. Next, we computed the element-wise 2D correlation coefficients between the two matrices (Eq. 1.3.5.5.1). Although slow drifts in the firing properties of the neurons might not be detected by this method, we were able to test the consistency of firing rate maps and compared those correlations with the results of two-fold cross-validation. The other slight difference between stationarity and cross-validation (1.3.5.5) was that the latter method balances the time but not the number of spikes, while the former method balances the number of spikes but not the time intervals.

1.3.6 Computing grid period

Grid period is the wavelength of the spatially periodic single unit activity. It is equivalent with distance between adjacent nodes of the autocorrelogram. Since autocorrelograms are periodic by construction, this spatial wavelength is defined as the inverse of the predominant spatial frequency component, also could be measured by hand as the average grid distance (11). When grids deviate from the 60° symmetry, the grid distance becomes multimodal. To estimate the exact unbiased grid periods, we performed a 2D spectral analysis on the ACs. Because the AC of spatial activity does not always generate a map with discrete patches when a spatially periodic pattern is still apparent, we characterized grid periods on spectral domain and derived the grid frequency from the AC periodograms. We refer to the periodograms computed from ACs as autoperiodograms. After the removal of the central peak from the AC (as described in 1.3.4.1), which is non-specific to the spatial pattern, we computed the 2D spectral density of the ACs by taking the complex conjugate of the inverse 2D Fourier transform (7). We next averaged the 2D spectral distribution across the X and Y coordinates and determined the largest amplitude peak positions. The peak position corresponds to the predominant spatial frequency component of the grid. This method was chosen because it is more precise and less biased than measuring the distance between the nodes by hand. Dividing the dimensions of the AC by the spatial frequency provided the distance of the X-Y peak in spatial bins. We then computed the Euclidian distance of the peak (defined by its X and Y coordinates) from the origin, the center of the autoperiodogram. This distance was multiplied by the scalar bin size (in m) to give the main grid period (λ). Grid frequencies were computed for ACs generated by each neuron and compared between environments.

1.3.7 Computing principal grid orientation

Grid orientations were computed from the autoperiodograms (Supplemental Experimental Procedures 1.3.5). Since the tangent of the orientation angle is the ratio of the X and Y coordinates of the largest peak on the 2D spectral distribution, the principal orientation (β) is defined as:

$$\beta = \arctan\left(\frac{X}{Y}\right). \tag{1.3.7.1}$$

1.3.8 Angle of rotational symmetry of grids

Because the angle of rotational symmetry was defined by the angle (γ) of rotation that brings a rotated AC into maximal overlap with its original pattern, we computed γ together with the gridness score (Supplemental Experimental Procedures 1.3.4.1) as the angle of rotation of the AC at which the Pearson correlation between the original and rotated AC was maximal. Since β is the orientation of the grid (Eq. 4), $\beta + \gamma$ gave the orientation of the second principal axis relative to the principal axis of each grid. Plotting β and γ on the ACs allowed for visual confirmation of the computed grid orientations (Fig. 1E and Figs. S12-28). When the observed rotational symmetry was compared to 60°, we applied a 60°±*s* confidence interval, where *s* represented the upper and lower 95% confidence limit of the mean direction (17) (*s*=3.076° and 2.68° for subject H and K, respectively).

1.3.9 Statistics

For the association between environmental features and grid pattern to be clearly delineated, the most robust analysis would consider how the grids from single neurons changed across environments. However, only a fraction of cells produced qualified spatially periodic patterns in all three landmark-rich environments, and even a smaller fraction of those were considered putative grid cells with ~60° rotational symmetries (Fig. S3G). Therefore, to produce the most robust dataset possible, we created a set consisting of only those neurons that produced spatially periodic activity or hexagonal grids in all environments, including or excluding OS. We refer to these as the “persistent” datasets with a distinctive “p” prefix (pSPC and pPGC) to discriminate those from SPC and PGC datasets. The Open Scene (OS) environment was excluded from the qualification criteria because the lack of visual cues and unbound area produced much fewer grids than any of the other three environments. The same-cells dataset is thus a subset of the full collection of recordings that produced qualified grids. We refer to the full set of qualified grids as the spatially periodic (SPC) and putative grid cell (PGC) datasets, without a prefix. In these datasets, the spike trains producing significant spatial periodicity of gridness in a given environment may derive from cells that did not display significant spatial modulation in any of the other environments. Hence, these spike train datasets from different environments may consist of single unit activity deriving from partially overlapping population of neurons. The intrinsic heterogeneity of these datasets should have increased the variance of neuronal responses to environmental differences.

Instead we observed a very consistent environmental dependency within and across days that improved the robustness of the statistics. Moreover, because we had no basis to assume that neurons display uniform gridness in each environment, we treated the single unit activity in the SPC and PGC datasets as independent entities as they were generated by cells that might have contributed selectively to different environments. In contrast, cells included by pSPC and pPGC datasets were treated as non-independent entities. The inclusion of both types of data and applying two different statistical methods together minimized the potential bias in our analysis deriving from either assumption.

With all SPC and PGC datasets, the general linear model ANOVA and its non-parametric version the Kruskal-Wallis test (Matlab, Mathworks®, Nattick, MA) were applied to compare gridness scores and grid periods across environments. The main factor was the environment (BY, LV LX, OS) and the dependent variable was gridness and grid period. ANOVA with repeated measures or its non-parametric version, the Friedman test, was used on the pSPC and pPGC datasets. First, we tested each variable for normality using the Lilliefors test and determined whether ANOVA or non-parametric alternatives can be applied. The selected features of spatial periodicity, including gridness scores, grid period, orientation and rotational symmetry were treated as dependent variables, and were pooled across a variable set of neurons for an independent measure general linear models of ANOVA (or Friedman's as a non-parametric alternative) for the SPC and PGC datasets, and pooled across constant set of neurons for a repeated measure ANOVA (or non-parametric alternatives).

To compare grid orientations and grid symmetry between environments we applied circular ANOVA (Watson-Williams test) on von Mises distributions (17) or Wheeler Watson as alternative, when von Misesness did not qualify (18). We performed Rayleigh tests for testing non-uniformity of circular data and Watson's goodness of fit test for testing conformity with the von Mises distribution. The main factor of circular ANOVA was the environment (BY, LV LX, OS). The dependent variables were the grid orientation and grid symmetry. We applied the Matlab® Circular Statistics Toolbox versions of Watson-Williams test for independent samples (SPC and PGC) and for the balanced repeated measures (pSPC and pPGC) (17).

REFERENCES

1. Quiroga RQ, Nadasdy Z, Ben-Shaul Y (2004) Unsupervised spike detection and sorting with wavelets and superparamagnetic clustering. *Neural Comput* 16(8):1661–1687.
2. Wild J, Prekopcsak Z, Sieger T, Novak D, Jech R (2012) Performance comparison of extracellular spike sorting algorithms for single-channel recordings. *J Neurosci Methods* 203(2):369–376.
3. Migliore M, et al. (2003) ModelDB: making models publicly accessible to support computational neuroscience. *Neuroinformatics* 1(1):135–9.
4. Hines ML, Morse T, Migliore M, Carnevale NT, Shepherd GM (2004) ModelDB: A Database to Support Computational Neuroscience. *J Comput Neurosci* 17(1):7–11.

5. Barry C, Ginzberg LL, O'Keefe J, Burgess N (2012) Grid cell firing patterns signal environmental novelty by expansion. *Proc Natl Acad Sci U S A* 109(43):17687–17692.
6. Sargolini F, et al. (2006) Conjunctive Representation of Position, Direction, and Velocity in Entorhinal Cortex on JSTOR. *Science* 312(5774):758–62.
7. Krupic J, Burgess N, O'Keefe J (2012) Neural Representations of Location Composed of Spatially Periodic Bands. *Science (80-)* 337(6096):853–857.
8. Buzsaki G (2002) Theta oscillations in the hippocampus. *Neuron* 33(3):325–340.
9. Mizuseki K, Buzsaki G (2014) Theta oscillations decrease spike synchrony in the hippocampus and entorhinal cortex. *Philos Trans R Soc Lond B Biol Sci* 369(1635):20120530.
10. Giocomo LM, Zilli EA, Fransen E, Hasselmo ME (2007) Temporal frequency of subthreshold oscillations scales with entorhinal grid cell field spacing. *Science (80-)* 315(5819):1719–1722.
11. Hafting T, Fyhn M, Molden S, Moser M-B, Moser EI (2005) Microstructure of a spatial map in the entorhinal cortex. *Nature* 436(7052):801–806.
12. Barry C, Hayman R, Burgess N, Jeffery KJ (2007) Experience-dependent rescaling of entorhinal grids. *Nat Neurosci* 10(6):682–4.
13. Krupic J, Burgess N, O'Keefe J (2015) Spatially Periodic Cells Are Neither Formed From Grids Nor Poor Isolation. Available at: http://arxiv.org/abs/1512.06248 [Accessed July 17, 2016].
14. Killian NJ, Jutras MJ, Buffalo EA (2012) A map of visual space in the primate entorhinal cortex. *Nature* 491(7426):761–764.
15. Beutler FJ, Leneman OAZ (1966) Random sampling of random processes: Stationary point processes. *Inf Control* 9(4):325–346.
16. Shumway RH, Stoffer DS (2006) *Time Series Analysis and Its Applications* doi:10.1007/978-1-4419-7865-3.
17. Berens P (2009) CircStat: A MATLAB Toolbox for Circular Statistics. *J Stat Softw* 31(10):1–21.
18. Mardia K V (1969) On Wheeler and Watson's Two-Sample Test on a Circle. *Sankhyā Indian J Stat Ser A* 31(2):177–190.

2 SI Tables

Table of Content:

2 SI: Tables

1 Tables related to Experimental Procedures

Scene	Size [m]	Area $[m^2]$	Bin size [m]	Shape	Boundaries	Obstacles	External cues	Topology (roof)
Backyard (BY)	18 x 18	324	1 x 1	square	✔	none	✔	open
Louvre (LV)	50 x 70	3,500	2 x 2	rectangle	✔	none	✔	open
Luxor (LX)	52 x 52 x 10	2,704	2 x 2	square	✔	✔	✔	closed
Open Space (OS)	(70 x 70) [*]	4,900	3 x 3	N/A	None	none	Space-ships	open

Table S1.1 Dimensions and features of the virtual environments.

[*] Because the open space environment did not have boundaries, the above dimensions indicate the area within which aliens might appear in the game.

Patient code	Diagnosis	Symptoms	Hemis-phere of eizure origin	Dominant Hemis-phere	Electrode implantation	Recording (days)
K	Complex partial epilepsy due to cavernous angiomas in the right mesial temporal lobe and in the inferior aspect of the right frontal lobe	Intractable seizures	Right	Left	An array of subdural electrodes over the right convexity temporal lobe and EC Bilateral hippocampal depth electrodes.	8
H	Complex partial epilepsy	Intractable seizures	Right	Left	An array of subdural electrodes over the right convexity temporal lobe and EC Bilateral hippocampal depth electrodes.	7
S	Chronic refractory partial and bilateral hippocampal sclerosis The patient had a VNS implant	Intractable seizures	Right	Left	Array of subdural electrodes grid placement, two posterior and anterior depth electrodes terminating in the right temporal pole and right lateral orbitofrontal gyri.	2
W	Chronic partial epilepsy	Altered mental status with syncope. Seizures and non-epileptic seizures	Right	Left	Right temporal frontal grid placement and bilateral hippocampal depth electrodes.	4

Table S1.2. Patients' data and diagnoses

2. Data Types

Types of cells	Description	Short name	trials	cells
Single units	Total single unit activity isolated		1,588	~397
Spatially periodic cells	Defined by spectral method	**SPC**	824	206
Spatially periodic cells with hexagonal firing fields	Spatially periodic cells with 60° rotational symmetry	pSPC60°	141	47
Permanent spatially periodic cells	Permanent spatial activity in 3 environments	**pSPC**	276	92
High-confidence putative grid cells	Defined based on spatially periodic activity distinguished from theta-modulation and directional tuning.	**PGC$_{\text{hi-conf}}$**	262	65
Permanent High-confidence putative grid cells	Defined based on spatially periodic activity distinguished from theta-modulation and directional tuning active in 2 or more environments.	**pPGC$_{\text{hi-conf}}$**	260	65
Putative grid cells	Putative grid cells with significant grid scores determined by using the Barry and Krupic method (7).	**PGC**	292	73
Permanent putative grid cells	Putative grid cells active in 2 or more environments	**pPGC**	156	39

Table S2. Types of cells recorded and classified. Numburs represent trials and cells after combining them from two subjects (H,K). Trials represent spike trains recorded from a given cell type during one navigation session in one environment. Colors associate individual tables with data types in the rest of the Supplemental Material. We refer to the datasets in the text with their short names. We only used SPC, pSPC, PGC and pPGC. The pSPC60° dataset was used only in one statistical analysis.

Stat#	Dataset	Test	Subject	Segments	Factors	d.f.	F	*P*	H
3.1	**SPC**	Three-way ANOVA with independent samples.	H	378	Env.	3	429.0304	<0.001 (1.1158e^{-120})	***
					Electrodes	4	0.8367	0.5025	
					Neurons	6	0.1679	0.9852	
			K	425	Env.	3	581.4083	<0.001 (3.4310e^{-154})	***
					Electrodes	4	0.6290	0.6420	
					Neurons	6	1.6721	0.1399	
			Grid period as dependent variable.						
3.2		Two-way ANOVA with independent samples.	**Subj.**	**Segm.**	**Fact.**	**d.f.**	**F**	***P***	**H**
			H	378	Env.	3	13.28	<0.001 (1.6839e^{-05})	***
					Days	6	0.9031	0.4680	
			K	425	Env.	3	7.8888	<0.001 (9.0850e^{-04})	***
					Days	6	1.8398	0.1330	
			Grid period as dependent variable, Environments and Days as factors.						
3.3		Two-way ANOVA with independent samples.	**Subj.**	**Segm.**	**Fact.**	**d.f.**	**F**	***P***	**H**
			H	378	Env.	3	1.0733	0.3483	
					Days	6	1.1295	0.3512	
			K	425	Env.	3	0.4317	0.6514	
					Days	6	2.8501	0.0313	*
			Normalized grid period as dependent variable, Environments and Days as factors.						
3.4	**SPC60°**	Kruskal–Wallis one-way ANOVA to test the effect of environment on the normalized grid cell periods scaled by the size of environment. across two subjects (H,K).	**Subj.**	**Neurons**	**Fact.**	**d.f.**	**Chi-square**	***P***	**H**
			Comb	41	Env.	2,38	5.9547	0.0509	
			Normalization involved scaling the grid periods by the size of the environment. Data are from the pSPC60° dataset. The dataset included neurons displaying hexagonal autocorrelogram and 60 ±10 ° symmetry. Data were combined.						
3.5	**SPC**	Kruskal–Wallis one-way ANOVA to test the effect of environment on the grid cell period.	Comb	824	Env.	3,820	621.24	<0.001 (2.49831e^{-134})	***
			SPC dataset combined across two subjects (H,K).						
3.6		Kruskal–Wallis one-way ANOVA to test the effect of days on the grid cell period. SPC dataset separately for subjects H and K.	**Subj.**	**Segm.**	**Fact.**	**d.f.**	**Chi-square**	***P***	**H**
			H	123	Days Env: BY	5	7.1130	0.2124	
			H	110	Days Env: LV	6	4.0413	0.6711	
			H	114	Days Env: LX	6	4.3685	0.6269	
			H	41	Days Env: OS	5	3.7068	0.5923	
	SPC		K	206	Days Env: BY	7	5.4195	0.6089	
			K	96	Days Env: LV	6	7.0305	0.3180	
			K	109	Days Env: LX	6	4.4495	0.6161	
			K	25	Days Env: OS	2	0.4960	0.7804	
			SPC dataset separately for subjects H and K.						
3.7	**pSPC**	Friedman’s non-parametric repeated measures test for the effect of days on the grid cell period.	**Subj.**	**Neurons**	**Fact.**	**d.f.**	**Chi-square**	***P***	**H**
			H	73	Days	4	1.5532	0.8172	
			K	73	Days	4	0.4505	0.9781	
			The pSPC dataset combined separately for subjects H and K.						
3.8		Friedman’s test for non-parametric repeated measures data to test	**Subj.**	**Neurons**	**Fact.**	**d.f.**	**Chi-square**	***P***	**H**
			Comb	73	Env.	3,216	147.6575	<0.001 (8.4344e^{-32})	***

		the effect of environment on the grid cell period.	Data are from the pSPC dataset combined across two subjects (H,K).						
3.9		Friedman's test for non-parametric repeated measures dataset.	Comb	115	Env. (BY-LX,LV,OS)	3,342	122.5536	<0.0001 (2.1748e^{-26})	***
			Testing the effect of environment ([BY] – [LV, LX, OS]). on the grid cell period from the pSPC dataset combined across two subjects (H,K).						
3.9.1	**PGC$_{hi\text{-}conf}$**	Kruskal-Wallis non-parametric test for the effect of environment (BY, LV, LX, OS) on the grid cell period.	H	113	Env. (BY,LX,LV,OS)	3,109	68.1321	<0.0001 (1.0719e^{-14})	***
			K	85	Env. (BY,LX,LV,OS)	3,81	70.2800	<0.0001 (3.7179e^{-15})	***
			Data from the PGC$_{hi\text{-}conf}$ dataset from two subjects (H,K).						
3.9.2	**pPGC$_{hi\text{-}conf}$**	Friedman's test for non-parametric repeated measures dataset to test the effect of environment ([BY, LV, LX, OS]) on the grid cell period	**Subj.**	**Neurons**	**Fact.**	**d.f.**	**Chi-square**	***P***	**H**
			Comb	10	Env.	3,27	27.1200	<0.0001 (5.5560e^{-06})	***
			Data from the pPGC$_{hi\text{-}conf}$ dataset combined across two subjects (H,K).						
3.9.3		Friedman's test for non-parametric repeated measure datasets.	Comb	10	Env.: BY-[LV, LX, OS]	1,9	10	0.0016	**
			Testing the effect of environment (BY-[LV, LX, OS]) on the grid cell period. Data from the pPGC$_{hi\text{-}conf}$ dataset combined across two subjects (H,K).						
3.9.4		Wilcoxon rank sum test for non-parametric repeated measures dataset.	Comb	10	Env.: large (LV-LX)	1,31	0.6015	0.5475	
			Testing the effect of environment (LV-LX) on the grid cell period. Data from the pPGC$_{hi\text{-}conf}$ dataset combined across two subjects (H,K).						
3.10	**pPGC**	Wilcoxon signed rank test a non-parametric repeated measures dataset.	**Subj.**	**Neurons**	**Fact.**	**d.f.**	**Zval (Wilcoxon)**	***P***	**H**
			Comb	19	Env. BY-[LV, LX, OS]	18	3.8277	<0.001 (1.2937e^{-04})	***
			Testing the effect of environment (BY – [LV, LX, OS]) on the grid cell period from the pPGC dataset. Grid distances were combined across two subjects (H,K). In order to achieve a sufficient sample size, we combined data from the large environments (LX,LV,OS) before comparing them to the small (BY).						
3.11		Wilcoxon signed rank test a non-parametric repeated measures dataset.	Comb	5	Env. (LX-LV)	1,4	12	>0.05 (0.3125)	
			Testing the effect of environment on the grid cell period from pPGC dataset. Grid distances were combined across two subjects (H,K). This test compares the grid sizes between two large environments (LX and LV).						
3.12		Friedman's test for non-parametric repeated measures dataset.	Comb	20	Env. (BY- LX,LV,OS)	19	-2.5413	<0.05 (0.011)	*
			Testing the effect of environment ([BY] – [LV, LX]) on the <u>normalized</u> grid cell period from the pPGC dataset combined across two subjects (H,K). Normalization involved scaling the grid periods by the size of the emvironment.						
3.13		Friedman's test for T-test repeated measures dataset to test the effect of environment.	Comb	5	Env. (LX,LV)	4	-0.1346	0.9165	
			Comparing environments (LV, LX) on the <u>normalized</u> grid cell period from the pPGC dataset combined across two subjects (H,K). Normalization involved scaling the grid periods by the size of the emvironment.						
3.14		A 2-ways ANOVA	K	26	Env.	3	0.9147	0.4547	
					Days	6	1.7560	0.1685	
			H	28	Env.	3	1.0819	0.3819	
					Days	7	0.2148	0.9772	
			Testing the factors of Environment and Days on <u>normalized</u> grid distances in the PGC data set for the two subjects separately. Normalization involved scaling the grid periods by the size of the emvironment.						
3.15	**SPC**	Median grid periods in different environments	**Subj.**	**BY (18 x 18 m)**		**LX (52 x 52 m)**	**LV (50 x 70 m)**	**OS (70 x 70 m)**	

		for two subjects in [m].	H	4.9624	< 16.9613	≈ 17.3384	< 26.3877
			K	5.4801	< 17.5989	≈ 17.5089	< 23.6084
			The less-than signs represent significant differences. Equals signs mean no significant difference.				

Table S3. Environmental dependency of grid period

Stat #	**Dataset**	**Test**	**Subject**	**Segments**	**Factors**	**d.f.**	**F**	***P***	**H**
4.1	**SPC**	ANOVA with independent measures, gridness as dependent variable in the SpC dataset.	H	384	Env.	3	18.6852	<0.001 ($2.4727e^{-11}$)	***
			H	223	Env. LV-LX	1	0.0245	0.1072	
			K	229	Env.	3	39.457	<0.001 ($1.9651e^{-15}$)	***
			K	204	Env. LV-LX	1	0.0563	0.8127	
			Average gridness across different environments for two subjects. Gridness was determined by spectral methods.						
4.2	**pSPC**	One-way ANOVA with repeated measures, gridness as dependent variable in the pSPC dataset.	H	26	Env.	3,25	0.9647	0.4248	
			K	24	Env.	3,23	1.4380	0.2575	
			Variance of average gridness across different environments for two subjects.						
4.3	**$\text{pPGC}_{\text{hi-conf}}$**	One-way ANOVA with repeated measures.	K	12	Env.	3	2.4970	0.1258	
			H	16	Env.	3	2.2323	0.1330	
			Testing the effect of Environments on the gridness score as dependent variable in the $\text{pPGC}_{\text{hi-conf}}$ dataset. Average gridness across different environments for two subjects.						

Table S4. Environmental dependency of gridness

			Subject	**Segments**	**Factors**	**d.f.**	**F**	***P***	**H**
5.1	**SPC**	ANOVA with independent measure on the complete SPC dataset.	H	389	Env.	3	1.8147	0.1441	
			K	435	Env.	3	2.1640	0.0919	
			Using firing rate as dependent variable. Average firing rate across different environments for two subjects.						
5.2	**pSPC**	Two-way ANOVA with repeated measures applied to the pSpC dataset.	H	74	Days	4	0.7577	0.5569	
					Env.	2	1.9692	0.1485	
					Interaction	8	0.7577	0.6408	
			K	74	Days	2	1.2694	0.2920	
					Env.	4	0.9291	0.4005	
					Interaction	8	0.6364	0.7440	
			Average firing rate across different days and environments for two subjects. Dataset containes a subset of neurons neurons that displayed significant gridness in 3 environments.						
5.3	**pPGC**	ANOVA independent measure on the pPGC dataset.	H	26	Env.	3	1.3881	0.2695	
			K	24	Env.	3	0.0100	0.9986	
			Using firing rate as dependent variable. Average firing rate across different environments for two subjects.						

Table S5. Average firing rate across environments

Stat#	**Test**		**Subject**	**Sessions**	**Factors**	**d.f.**	**F**	***P***	**H**
6.1	One-way ANOVA repeated measures (5 days 4 tasks) on environment coverage as dependent vaiable.		H	20	Env. % coverage 71.24 > 54.74 ≈ 51.57 > 31.64	3	106.15	<0.001 ($8.9612e^{-11}$)	***
			K	20	Env. % coverage 72.45 > 49.94 < 52.93 > 19.23	3	23.65	<0.001 ($4.0125e^{-6}$)	***
			Coverage was expressed as percent of the total area visited during the spatial navigation session.						
6.2	One-sample T-test to compare the difference in coverage between the LV and LX environments.		**Subj.**	**days**	**Factors**	**d.f.**	**T-stat**	***P***	**H**
			H	5	Env.	1	1.6567	>0.05 (0.1729)	
			K	5	Env.	1	-3.7323	<0.05 (0.0203)	*
			Subj.	**Sess.**	**Fact.**	**d.f.**	**F**	***P***	**H**
6.3	Two-Factor repeated measure ANOVA on coverage as dependent variable.		H	20	Env.	3	19.4820	<0.001 ($6.6206e^{-05}$)	***
					Days	4	0.2949	0.8757	
			K	20	Env.	3	23.65	<0.001 ($4.0125e^{-6}$)	***
					Days	4	3.2498	0.0504	
6.4	**Dataset**	**Test**	**Subj.**	**Neurons**	**Fact.**	**d.f.**	**Chi-square**	***P***	**H**
	pSPC	Kruskal-Wallis non-parametric multiple comparision.	H	79	Env. (BY,LX,LV,OS)	3,75	64.6974	<0.0001 ($5.8221e^{-14}$)	***
			K	164	Env. (BY,LX,LV,OS)	3,160	121.1995	<0.0001 ($4.2568e^{-26}$)	***
			Testing for the effect of environment on grid distances under balanced environmental coverage for the two subjects separately.						

Table S6. The variation in areal coverage

<table>
<tr><th>Stat#</th><th>Dataset</th><th>Test</th><th>Subject</th><th>Segment</th><th>Factors</th><th>d.f.</th><th>F</th><th><i>P</i></th><th>H</th></tr>
<tr><td rowspan="5">7.1</td><td rowspan="5">SPC</td><td rowspan="5">Two-way circular ANOVA (Watson & Williams) results on grid orientation from the SPC dataset.</td><td rowspan="2">H</td><td rowspan="2">311</td><td>Env.</td><td>2</td><td>35.4449</td><td><0.001 (1.6209e^{-14})</td><td>***</td></tr>
<tr><td>Days</td><td>5</td><td>2.5680</td><td>0.0271</td><td>*</td></tr>
<tr><td rowspan="2">K</td><td rowspan="2">376</td><td>Env.</td><td>2</td><td>12.9579</td><td><0.001 (3.7015e^{-6})</td><td>***</td></tr>
<tr><td>Days</td><td>6</td><td>1.8633</td><td>0.9281</td><td></td></tr>
<tr><td colspan="7">Factor 1: Environments (BY, LV, LX) Days: 1-7 consecutive days (Fig. S25).</td></tr>
<tr><td rowspan="5">7.2</td><td rowspan="9">pSPC</td><td rowspan="5">Two-way circular ANOVA (Watson & Williams) with repeated measures.</td><td rowspan="2">H</td><td rowspan="2">47</td><td>Env.</td><td>2</td><td>4.4184</td><td>0.0162</td><td>*</td></tr>
<tr><td>Days</td><td>4</td><td>0.7737</td><td>0.5466</td><td></td></tr>
<tr><td rowspan="2">K</td><td rowspan="2">47</td><td>Env.</td><td>2</td><td>4.8958</td><td>0.0107</td><td>*</td></tr>
<tr><td>Days</td><td>4</td><td>1.0595</td><td>0.3845</td><td></td></tr>
<tr><td colspan="7">From the pSPC dataset, grid orientation as dependent variable.
Factor 1: Environments (BY, LV, LX), Factor 2: Days: 1-5 days.</td></tr>
<tr><td rowspan="4">7.3</td><td colspan="3" rowspan="4">The angular mean orientations of grids in the three different envieonments with respect to external orientation cues (pSPC dataset).</td><td>Subj</td><td>n</td><td>BY</td><td>LV</td><td>LX</td></tr>
<tr><td>H</td><td>74</td><td>44.9502°</td><td>33.3972°</td><td>47.9038°</td></tr>
<tr><td>K</td><td>74</td><td>45.2648°</td><td>36.3928°</td><td>45.2994°</td></tr>
<tr><td colspan="5">The cells from the pSPC dataset included spatially periodic cells that were active in all 3 environments.</td></tr>
<tr><td rowspan="3">7.4</td><td rowspan="7">pPGC</td><td rowspan="3">Circular ANOVA (Watson & Williams) results on pPGC dataset.</td><td>Subject</td><td>Neurons</td><td>Fact</td><td>d.f.</td><td>F</td><td><i>P</i></td><td>H</td></tr>
<tr><td>[H,K]</td><td>30</td><td>Env.</td><td>3,26</td><td>4.2524</td><td>0.0143</td><td>*</td></tr>
<tr><td colspan="7">Data were combined from the two patients.</td></tr>
<tr><td rowspan="3">7.5</td><td colspan="3" rowspan="3">The angular mean orientations of grids in the three different envieonments relative to external orientation cues.</td><td>Subj</td><td>n</td><td>BY</td><td>LV</td><td>LX</td></tr>
<tr><td>[H,K]</td><td>30</td><td>56.1092°</td><td>36.2281°</td><td>61.0761°</td></tr>
<tr><td colspan="5">The cells in the sample included spatially periodic cells that were active in all 3 environments from the pPGC dataset.</td></tr>
<tr><td rowspan="4">7.6</td><td rowspan="8">pSPC</td><td rowspan="4">Watson-Williams test for the equality of mean grid orientation on the pSPC same-cells dataset.</td><td>Subject</td><td>Segm</td><td>Env.</td><td>d.f.</td><td>F</td><td><i>P</i></td><td>H</td></tr>
<tr><td>H -K</td><td>49</td><td>BY</td><td>1, 48</td><td>0.4029</td><td>0.5286</td><td></td></tr>
<tr><td>H -K</td><td>49</td><td>LV</td><td>1, 48</td><td>2.0493</td><td>0.1588</td><td></td></tr>
<tr><td>H -K</td><td>49</td><td>LX</td><td>1, 48</td><td>3.2680</td><td>0.0769</td><td></td></tr>
<tr><td rowspan="4">7.7.</td><td rowspan="4">Watson-Williams test for the equality of mean grid orientation.</td><td>Comb</td><td>49</td><td>Env.
BY-LV</td><td>1,97</td><td>15.6364</td><td><0.001 (01.4511e^{-4})</td><td>***</td></tr>
<tr><td>Comb</td><td>49</td><td>Env.
LV-LX</td><td>1,97</td><td>5.1152</td><td><0.05 (0.0259)</td><td>*</td></tr>
<tr><td>Comb</td><td>49</td><td>Env.
BY-LX</td><td>1,97</td><td>1.7934</td><td>0.1836</td><td></td></tr>
<tr><td colspan="7">Test between BY-LV, LV-LX and BY-LX environments on the pSPC same-cells dataset combined across subjects.</td></tr>
<tr><td>7.8</td><td>SPC</td><td>Watson-Williams test for the equality of mean grid</td><td>Comb</td><td>436</td><td>Env.
BY-LV</td><td>1,434</td><td>69.2849</td><td><0.001 (1.1102e^{-15})</td><td>***</td></tr>
</table>

		orientation.	Comb	289	Env. LV-LX	1,287	55.5930	<0.001 $(1.0603e^{-12})$	***
			Comb	445	Env. BY-LX	1,443	1.3459	0.2466	
			Test between BY-LV, LV-LX and BY-LX environments on the SPC dataset combined across subjects.						
7.9	**$PGC_{hi\text{-}conf}$**	The angular mean orientations of grids.	**Subject**		**n**	**BY**	**LV**	**LX**	
			K		112	40.7707°	29.3931°	48.2491°	
			H		117	48.4061°	40.5197°	43.0110°	
			Data from the $PGC_{hi\text{-}conf}$ dataset in three different envieonments relative to external orientation cues for the two subjects.						
7.10		Circular ANOVA (Watson Williams test) of differences in angular mean orientations of grids.	**Subject**	**Segments**	**Env.**	**d.f.**	**F**	***P***	**H**
			K	112	BY, LV, LX	2, 109	5.1829	*P*<0.01 (0.0071)	**
			H	117	BY, LV, LX	2,114	7.9491	*P*<0.001 $(5.8643e^{-04})$	***
			From the $PGC_{hi\text{-}conf}$ dataset in three different envieonments relative to external orientation cues.						
7.11	**$pPGC_{hi\text{-}conf}$**	Circular ANOVA (Watson Williams test) applied to mean orientations of grids.	[H, K]	39	BY, LV, LX	3, 152	3.2626	*P*<0.05 (0.0232)	*
			Data from the $pPGC_{hi\text{-}conf}$ dataset combined from two subjects for testing differences between three environments relative to external orientation cues.						
7.12		Parametric Two-way Circular ANOVA (HK test) applied to mean orientations of grids.	[H, K]	116	Env. (BY, LV, LX)	2	4.3472	*P*<0.05 (0.0161)	*
					Days	11	1.4320	*P*= 0.1748	
			From the $pPGC_{hi\text{-}conf}$ dataset combined from two subjects. The factors were Environments and Days.						
7.13		Repeated-sample circular test for mean grid orientation in differently sized and shaped environments using the $pPGC_{hi\text{-}conf}$ dataset.	**Subject**	**Neurons**	**Env.**	**d.f.**	**Mu (conf. interval)**	***P***	**H**
			[H, K]	39	BY, LV	1, 38	-0.1161 (-0.2067,-0.0255)	*P*<0.05	*
			[H, K]	39	LV, LX	1, 38	-0.1153 (-0.2077,-0.0229)	*P*<0.05	*
			[H, K]	39	BY, LX	1, 38	-0.1161 (-0.0661,0.0640)	P>0.5	
			Testing the effect of environmental-geometry on the grid orientation. BY and LX are both square shaped, LV is rectangular.						

Table S7. Environmental dependency of grid orientation

<table>
<tr><th>Stat #</th><th>Dataset</th><th>Test</th><th>Subject</th><th>Segments</th><th colspan="2">Factors</th><th>d.f.</th><th>F</th><th colspan="2"><i>P</i></th><th>H</th></tr>
<tr><td rowspan="3">8.1</td><td rowspan="10">SPC</td><td rowspan="3">One-way circular ANOVA (Watson-Williams test) with independent samples on the SPC dataset.</td><td>H</td><td>213</td><td colspan="2">Env.</td><td>3</td><td>13.2597</td><td colspan="2"><0.001 ($5.9108e^{-8}$)</td><td>***</td></tr>
<tr><td>K</td><td>214</td><td colspan="2">Env.</td><td>3</td><td>21.9569</td><td colspan="2"><0.001 ($1.1520e^{-12}$)</td><td>***</td></tr>
<tr><td colspan="9">Dependent variable: grid rotational symmetry. Factor: Environments (BY, LV, LX, OS).</td></tr>
<tr><td rowspan="3">8.2</td><td rowspan="3">Circular ANOVA (Watson-Williams test).</td><td>H</td><td>74</td><td colspan="2">Env. (LV,LX)</td><td>1,132</td><td></td><td colspan="2">0.8875</td><td>*</td></tr>
<tr><td>K</td><td>74</td><td colspan="2">Env. (LV,LX)</td><td>1,136</td><td></td><td colspan="2">0.1640</td><td>**</td></tr>
<tr><td colspan="9">Comparison of grid rotational symmetry between LV and LX environments in the SPC dataset.</td></tr>
<tr><td rowspan="4">8.3</td><td rowspan="4">Average angle of grid rotational symmetry by environment for two subjects in angular degree.</td><td>Subj.</td><td>BY
(18 x 18 m)</td><td>H$_a$</td><td>LX
(52 x 52 m)</td><td>H$_a$</td><td>LV
(50 x 70 m)</td><td>H$_a$</td><td colspan="2">OS
(70 x 70 m)</td></tr>
<tr><td>H</td><td>61.59°</td><td>>></td><td>45.28°</td><td>≈</td><td>44.77°</td><td>></td><td colspan="2">32.98°</td></tr>
<tr><td>K</td><td>59.08°</td><td>>></td><td>47.89°</td><td>≈</td><td>43.06°</td><td>>></td><td colspan="2">27.81°</td></tr>
<tr><td colspan="9">SPC dataset. Ha is the accepted alternative hypothesis of inequality in rotational symmetry between environments (‘≈’ <i>P</i>>0.05; ‘>’ <i>P</i><0.01; ‘>>’ <i>P</i><0.001).</td></tr>
<tr><td rowspan="3">8.4</td><td rowspan="8">pSPC</td><td rowspan="3">Repeated measure one-way circular ANOVA (Watson-Williams test) on the rotational symmetry in the pSPC dataset.</td><td>H</td><td>74</td><td colspan="2">Environments (BY,LV,LX)</td><td>2,72</td><td>5.7739</td><td colspan="2"><i>P</i><0.01 (0.0047)</td><td>**</td></tr>
<tr><td>K</td><td>71</td><td colspan="2">Environments (BY,LV,LX)</td><td>2,69</td><td>20.5694</td><td colspan="2"><i>P</i><0.001 ($9.8483e^{-08}$)</td><td>***</td></tr>
<tr><td colspan="9">Dependent variable: grid rotational symmetry. Factor: Environments (BY, LV, LX).</td></tr>
<tr><td rowspan="5">8.5</td><td rowspan="5">Repeated measure two-way circular ANOVA (Watson-Williams test) on the rotational symmetry in the pSPC dataset.</td><td>H</td><td>74</td><td colspan="2">Environments (BY,LV,LX)</td><td>2</td><td>5.6501</td><td colspan="2"><i>P</i><0.01 (0.0059)</td><td>**</td></tr>
<tr><td></td><td>74</td><td colspan="2">Days</td><td>6</td><td>0.9213</td><td colspan="2">0.4871</td><td></td></tr>
<tr><td>K</td><td>71</td><td colspan="2">Environments (BY,LV,LX)</td><td>2</td><td>19.7765</td><td colspan="2"><i>P</i><0.001 ($9.8483e^{-08}$)</td><td>***</td></tr>
<tr><td></td><td>71</td><td colspan="2">Days</td><td>4</td><td>1.7248</td><td colspan="2">0.1571</td><td></td></tr>
<tr><td colspan="9">Dependent variable: grid rotational symmetry and days. Factor: Environments (BY, LV, LX).</td></tr>
<tr><td rowspan="3">8.6</td><td rowspan="6">pPGC$_{\text{hi-conf}}$</td><td rowspan="3">Circular ANOVA (Watson-Williams test) on the rotational symmetry in the PGChi-conf dataset with balanced coverage</td><td>H</td><td>78</td><td colspan="2">BY, LV, LX, OS</td><td>3, 75</td><td>9.034</td><td colspan="2"><i>P</i><0.001 ($3.5194e^{-05}$)</td><td>***</td></tr>
<tr><td>K</td><td>140</td><td colspan="2">BY, LV, LX, OS</td><td>3,134</td><td>23.7839</td><td colspan="2"><i>P</i><0.001 ($2.1031e^{-12}$)</td><td>***</td></tr>
<tr><td colspan="9">After 50% reduction of trajectory in the BY environment. Factor: Environments (BY, LV, LX, OS).</td></tr>
<tr><td rowspan="3">8.7</td><td rowspan="3">Pairwise Circular ANOVA (Watson-Williams test) on the rotational symmetry in the PGChi-conf dataset with balanced coverage.</td><td>H</td><td>50</td><td colspan="2">BY, LV</td><td>1,49</td><td>15.7497</td><td colspan="2"><i>P</i><0.001 ($2.3587e^{-04}$)</td><td>***</td></tr>
<tr><td>H</td><td>32</td><td colspan="2">LV, LX</td><td>1,31</td><td>0.0329</td><td colspan="2"><i>P</i>=0.8573</td><td></td></tr>
<tr><td>H</td><td>27</td><td colspan="2">LX, OS</td><td>1,26</td><td>0.3311</td><td colspan="2"><i>P</i>=0.5700</td><td></td></tr>
</table>

			K	79	BY, LV	1,78	40.2528	*P*<0.001 ($1.3508e^{-08}$)	***
			K	42	LV, LX	1,41	0.1320	*P*=0.7183	
			K	57	LX, OS	1,56	0.6542	*P*=0.4220	
			After 50% reduction of trajectory in the BY environment. Factor: Environments (BY-LV,LV- LX and LX-OS).						

Table S8. Environmental dependency of grid rotational symmetry

Stat #	**Dataset**	**Test**	**Subject**	**Segments**	**Factors**	**d.f.**	**F**	***P***	**H**
9.1	**PGC$_{hi\text{-}conf}$**	One-way ANOVA for testing the environment-dependent variation of heading directions of all neurons in the PGChi-conf dataset.	H	85	BY, LV, LX, OS	3, 81	2.6122	0.0569	
			Dependent variable: average tuning direction; Environments: BY, LV, LX, and OS.						
9.2		One-way ANOVA for testing the environment-dependent variation of resultant vectors of the direction-tuning of neurons in the PGC$_{hi\text{-}conf}$ dataset.	H	85	BY, LV, LX, OS	3, 81	0.1616	0.9219	
			Dependent variable: resultant vector; Environments: BY, LV, LX, and OS.						
9.3	**pPGC$_{hi\text{-}conf}$**	Repeated sample ANOVA for testing the environment-dependent variation of resultant vectors of the direction-tuning of neurons active in multiple environments from the pPGC$_{hi\text{-}conf}$ dataset	H	74	Days	4	1.2264	0.3092	
					Environments: BY, LV, LX, OS	2	0.2782	0.7581	
			Dependent variable: resultant vector; Environments: BY, LV, LX, and OS.						

Table S9. Direction tuning of putative grid cells

Stat #	Dataset	Test	Subject	Segments	Environ-ments	d.f.	Median r	*P*	H
10.1	**SPC**	Wilcoxon signed rank test for testing the hypothesis that the distribution median is equal to 0.	Comb.	879	BY, LV, LX, OS	1,878	0.093181	$4.726e^{-49}$	***
			Two-fold cross-validation: Dependent variable: 2D correlation coefficient between firing rate maps of the first and second half of the 5 min navigation trial.						
10.2	**$\text{PGC}_{\text{hi-}}$**	Wilcoxon signed rank test for testing the hypothesis that the distribution median is equal to 0.	Comb.	285	BY, LV, LX, OS	1,284	0.1412	$1.4887e^{-19}$	***
			Two-fold cross-validation: Dependent variable: 2D correlation coefficient between firing rate maps of the first and second half of the 5 min navigation trial.						
10.3	**SPC**	Wilcoxon signed rank test for testing the hypothesis that the distribution median is equal to 0.	Comb.	969	BY, LV, LX, OS	1,968	0.13829	$1.2137e^{-86}$	***
			Stationarity: Dependent variable: 2D correlation coefficient between firing rate maps constructed from odd and even numbered spikes.						
10.4	**$\text{PGC}_{\text{hi-}}$**	Wilcoxon signed rank test for testing the hypothesis that the distribution median is equal to 0.	Comb.	311	BY, LV, LX, OS	1,310	0.20958	$1.1556e^{-35}$	***
			Stationarity: Dependent variable: 2D correlation coefficient between firing rate maps constructed from odd and even numbered spikes.						

Table S10. Stability of grids estimated by cross-validation and stationarity of firing rate maps.

3 SI Figures

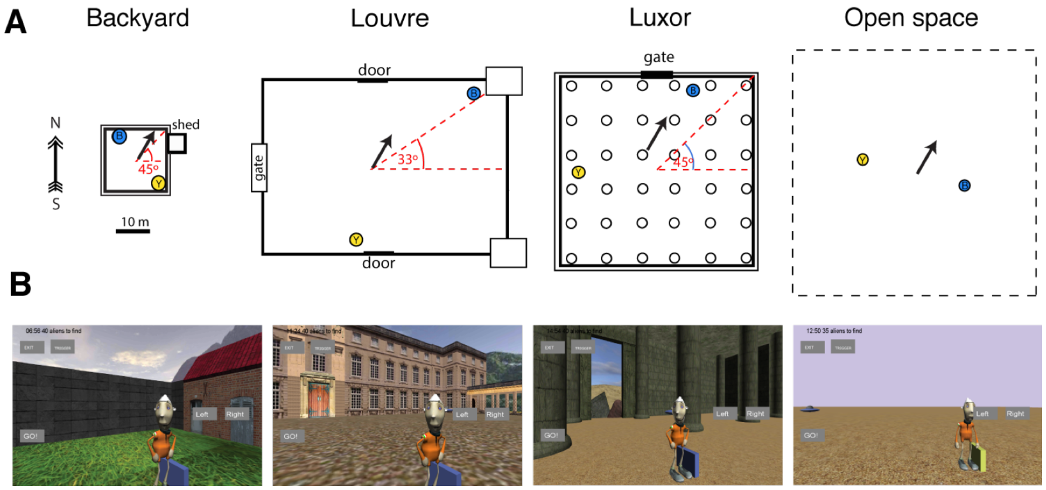

Fig. S1: Layout of the four virtual environments. (A) Scale invariant representations of the four environments. Bolded circles indicate the position of space ships. Bolded lines outline the navigable area of each map. The open space environment did not have physical boundaries so the dashed area represents the range of alien placements. Arrows in the middle of environments indicate the initial orientation of the player. Red dashed lines indicate the angle of corners from the center. (B) Corresponding screen shots (backyard, Louvre, Luxor, open space).

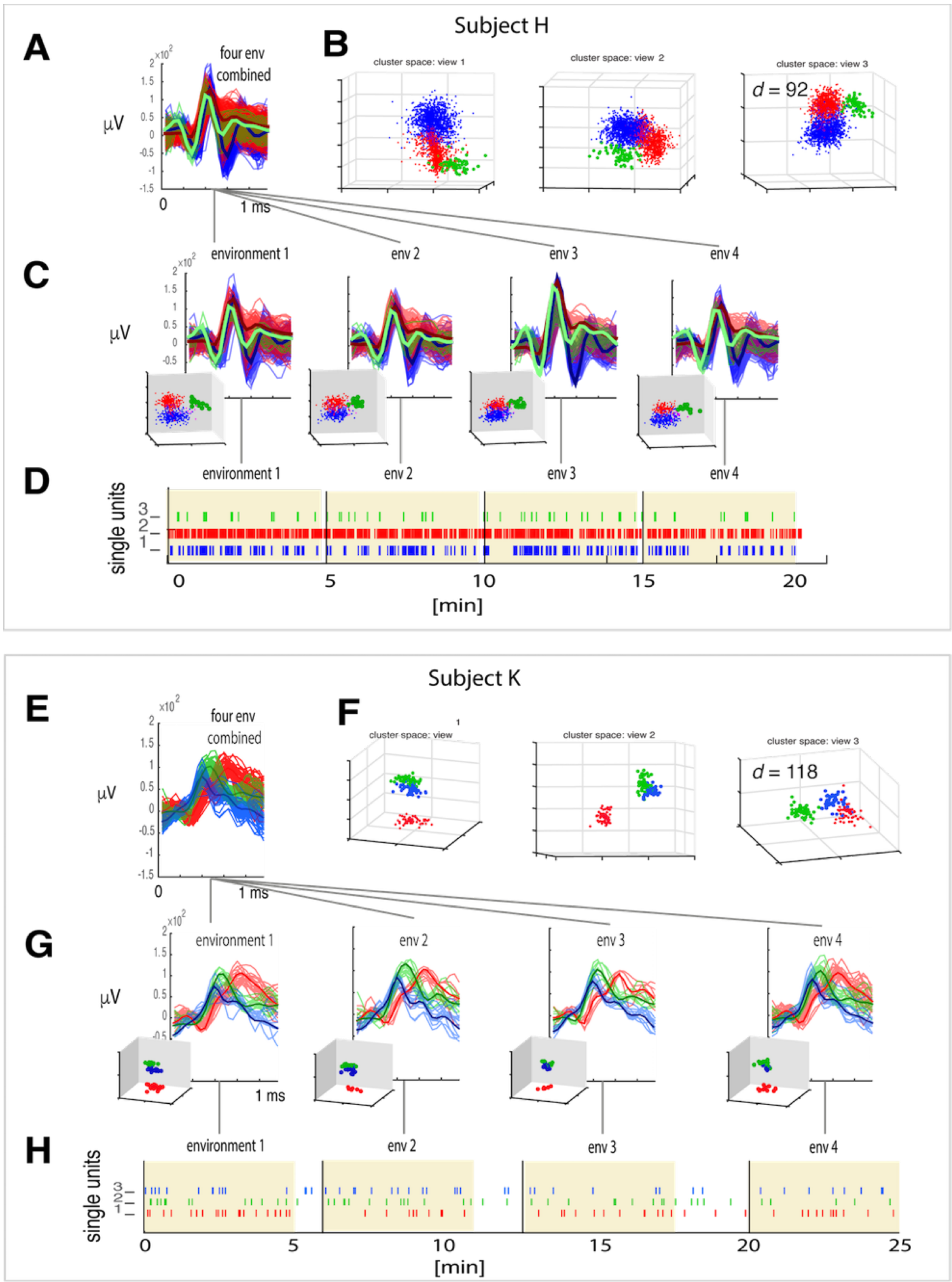

Fig. S2. Spike sorting and integrity of single-unit activity across environments. Single unit activity extracted from continuous recordings, including navigation in four different virtual environments, illustrated with examples from two patients (S-D: patient 1; E-H: patient 2). (A) Classification of spike waveforms collected during a 20 min recording session. (B) Clustering of wavelet coefficients indicate spikes originating from 3 putative neurons shown with 3 of their wavelet coefficients. (C) The same 3 waveforms clusters superimposed and sorted according to the environments (env 1-4). The 3D insets illustrate the consistent quality of unit isolation during the navigation in each environment. (D) The raster plot of three single-unit cluster during the four blocks of navigation in the four different environments. (E-H) Same representation as in (A-D), except these single units were isolated from a different subject during a 25 min recording session. For the sake of illustration only the first 100 waveforms are plotted. Heavy lines over waveforms represent means. Spikes were amplitude and time aligned within a 1.166 ms window (28 sampling points after smoothing and down-sampling the 48 kHz recordings to 24 kHz).

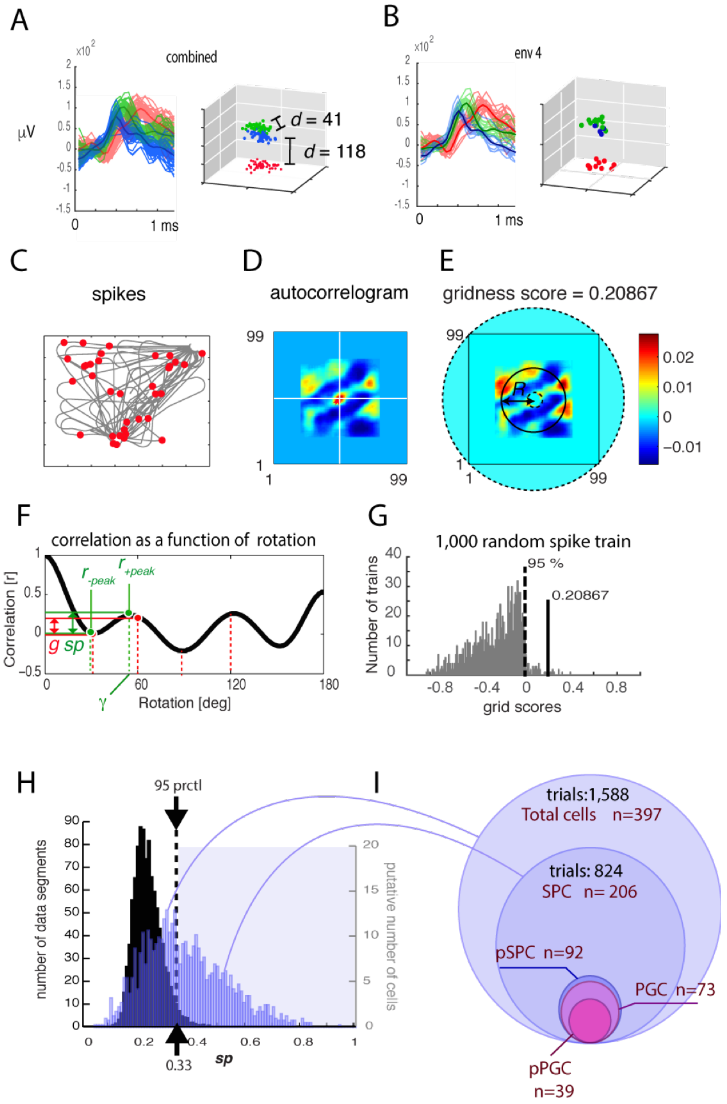

Fig. S3. Definition gridness and spatial periodicity. (A) Single unit activity detected and classified based on wavelet coefficients extracted from a 20 min recording session. (B) A subset of those single units was active in the LV environment. (C) Traces of 5 min navigation in the LV environment (gray lines) with single unit activity superimposed (red markers). (D) Autocorrelogram constructed based on the firing rate map (not shown). (E) The normalized autocorrelogram after removal of the central peak. The inner and outer circles represent the omission of the central peak and the 2.5-times the radius of largest peaks around the center, respectively. In this example, the outer ring is beyond the boundaries of the autocorrelogram. (F) Correlation coefficients as a function of rotation of the autocorrelograms. The autocorrelogram was rotated from 1° to 180°. The modulation depth of correlation defined as the difference between the maximum of troughs at 30, 90 and 150°, and the minimum of peaks, served as the gridness score ***g*** (red arrow). Spatial periodicity, in contrast, was defined as the difference between the local minimum (r_{-peak}) closest to the 0° and the first local maximum (r_{+peak}) at an angle larger than the angle of local minimum of correlation. The angles at which the peak correlation occurred (green dashed lines) defined the angle (γ) of spatial periodicity (sp).

(G) The distribution ***g*** after shuffling the spatial firing configurations of single unit activity 1,000-times. Dashed line near zero represents the 95 percentile confidence of the distribution. Because for the single unit in this example ***g***=0.20867 > 95 percentile, we rejected the Null and accepted the alternative that the spatial activity of this unit was periodically modulated. (H) We computed the distribution of grid scores from 1,000 randomized autocorrelograms as well as the distribution of observed spatial periodicity (sp) and the two histograms were superimposed. Blue bars represent the combined distribution of spatial periodicity (***sp***) from n=2,008 single unit data segments. The black histogram represents the distribution of ***sp*** over a population of 1,000 randomly generated autocorrelograms. Dashed line signifies the 95 percentile of the random gridness distribution. The left side ordinate represents the number of segments at a given ***sp***, while the right ordinate represents the approximate number of cells these data segments derive from. (I) The proportional Euler diagram represents the number of trials and neurons used in this study (Supplemental Table 3). The largest circle corresponds to the whole sample of isolated single units and trials, also correspond to the blue histogram in (H). A fraction of these cells was identified containing spatially periodic (SPC) cells and they correspond to the right side of the distribution (***sp***>0.33) where the overlap with the ***sp*** computed from the randomized firing rate maps was less than 5 percent. A subset of those cells displayed persistent activity in at least 3 environments, labeled as persistent spatially periodic (pSPC). The inner two circles represent the subset of putative grid cells (PGC) and persistent putative grid cell (pPGC) populations. Fractions are proportional to the total number of trials and isolated single units (outer circle).

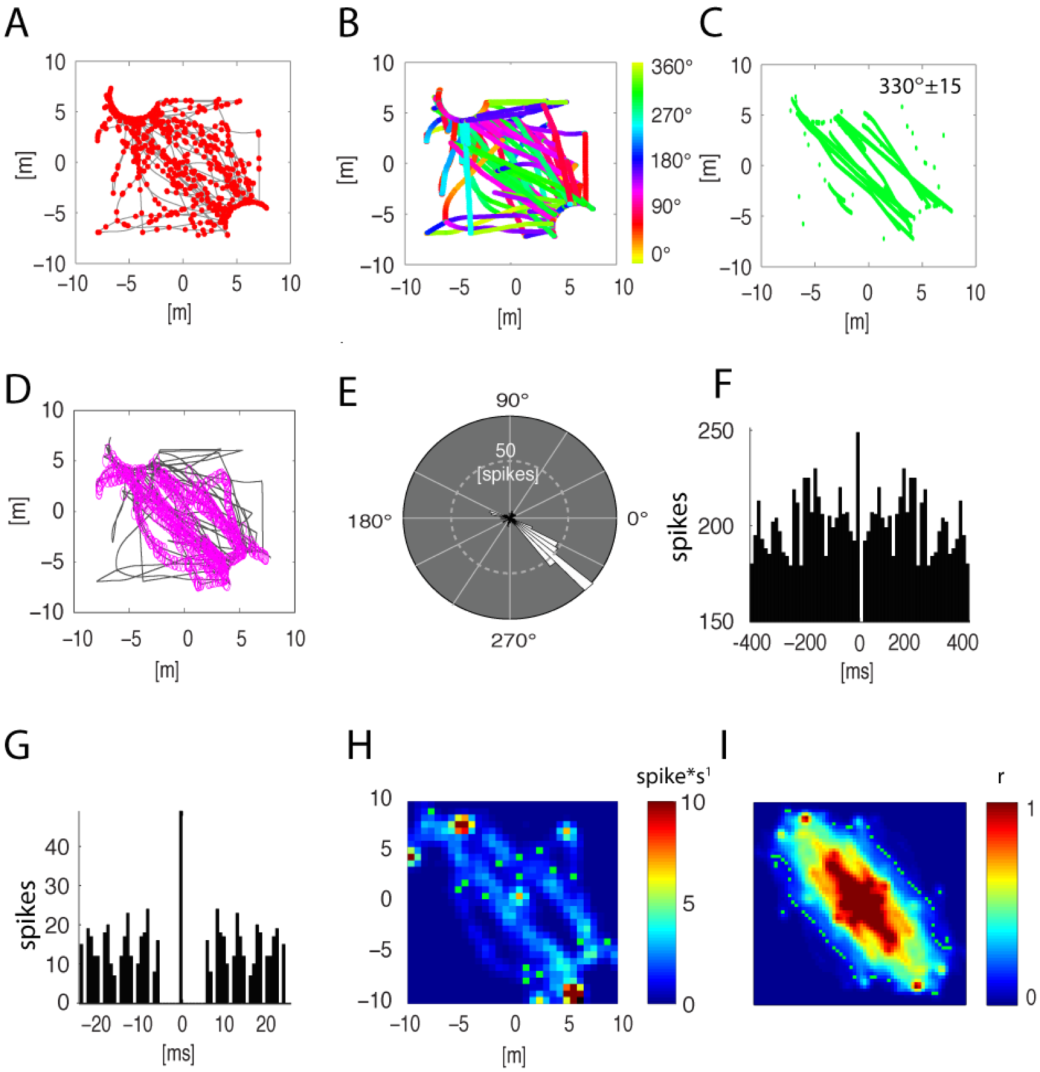

Fig. S4. Modeling and verifying theta-frequency modulated spike trains combined with directional but no spatial tuning. (A) Recorded spikes (red symbols) and the path of virtual navigation overlaid. Data were collected over 5 min of spatial navigation in the BY environment. (B) Heading directions of the navigation are color-coded. (C) Iso-directional pathway segments (330°+/-15 in this example) extracted from the original pathway in (A and B). (D) Spikes dispersed along the iso-directional segments constrained by a sharp direction tuning and a combination of theta and alpha frequency modulation. Bursts firing and 5 ms refractoriness was added to the temporal modulation of the spike train. (E) Angular histogram verified the direction tuning of the simulated spike train. The direction tuning for a given spike train was sampled from a uniform von Mises distribution. (F) The autocorrelogram spikes reflects a periodic ~5 Hz theta frequency modulation and a smaller amount of 10 Hz modulation. (G) Autocorrelogram at small timescale verified a ~5 ms burst firing. (H) Spatial firing rate map of the simulated neuron's activity. (I) Spatial autocorrelogram of the firing rate map on (H).

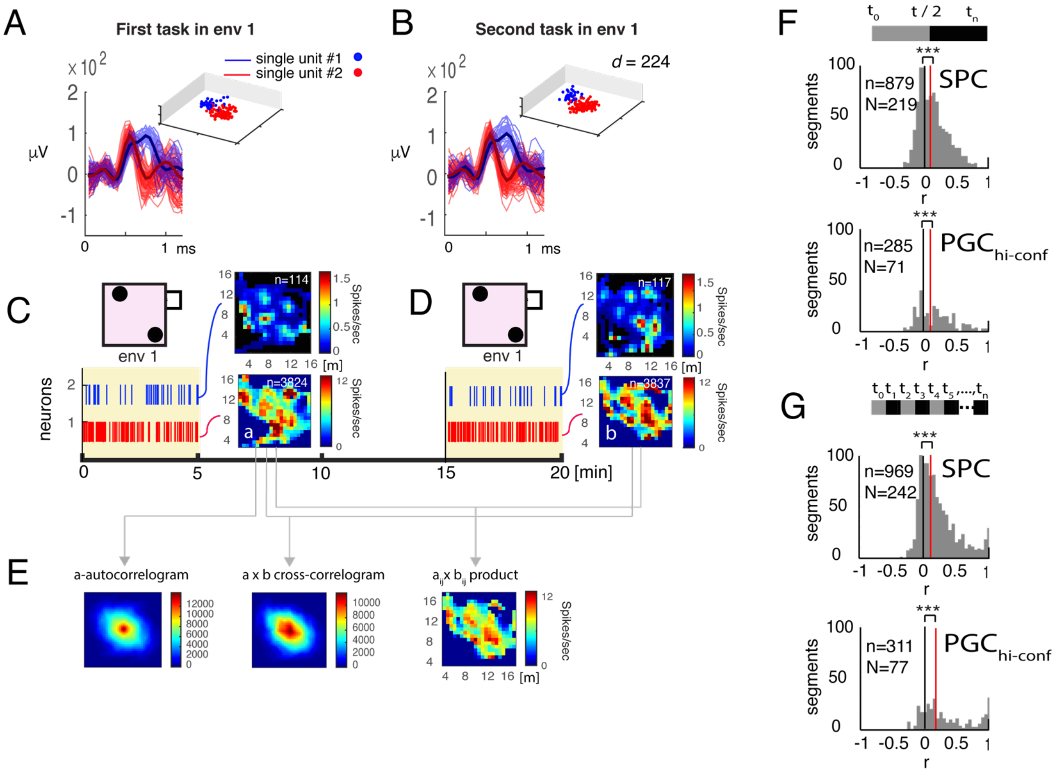

Fig. S5. Cross-validation of the spatial mapping of single unit activity. In this example, we were monitoring the spatial activity of the same two putative neurons during the same but non-contiguous navigation session in two identical environments separated by 10 min. (A) Single unit waveforms associated with the first 5 min game session and (B) the other 5 min game time in the same environment (B). The waveforms are superimposed and their wavelet coefficient clusters are shown in 3D insets. (C,D) the spatial activity of single unit #2 was mapped during the two non-contiguous navigation sessions. (C) Raster plots of spike times associated with the two single unit clusters (consistent color coding) during the two navigation sessions. The associated heat maps represent the topography of the firing rates of the two single units during 5 min spatial navigation. Hot colors indicate high firing probability. The two-dimensional correlation coefficients between the two firing rate maps were significant (r> .5, $p_{(n=22,22)}$ <.0001) for both single units. (E) The spatial autocorrelogram of firing rate map a, the spatial cross-correlogram of firing rate map a and b and the element-by-element product of firing rate maps a and b of panel (C) and (D). Neither the spatial autocorrelogram nor the *a* x *b* cross-correlogram differed significantly (Student's paired-sample t-test, t= .3072 $p_{(n=22,22)}$= .7588). Conversely, the element-by-element product of *a* and *b* unraveled the grid structure shared between the two navigation trials. Pink insets represent the layout of the BY environment where the 5 min navigation took place. (F) Two-fold cross-validation of the stability of firing rate maps across two populations of spike trains. Histograms represent the distribution of 2D correlation coefficients between firing rate maps computed from the first 2.5 minutes and second 2.5 minutes of every navigations session in combined across different environments, days and subjects. SPC dataset on top and $\text{PGC}_{\text{hi-conf}}$ dataset below. (G) Stationarity analysis. Histograms represent correlation coefficients computed between firing rate maps from single units sampled every odd numbered and every even numbered spike, recorded during the same recording session. Vertical black lines mark r=0 and vertical red lines represent the medians of distributions. R > 0 predominates in all distributions. Y axes: number of spike train segments; X axes: 2D Pearson's correlation on pixels. (F,G) 68-83% of cells achieved *r*>0.2 correlations between the first and second intervals. (n: the total number of data segments; N: the number of neurons). See further examples for cross-validation and stationarity analysis in Fig. S37.

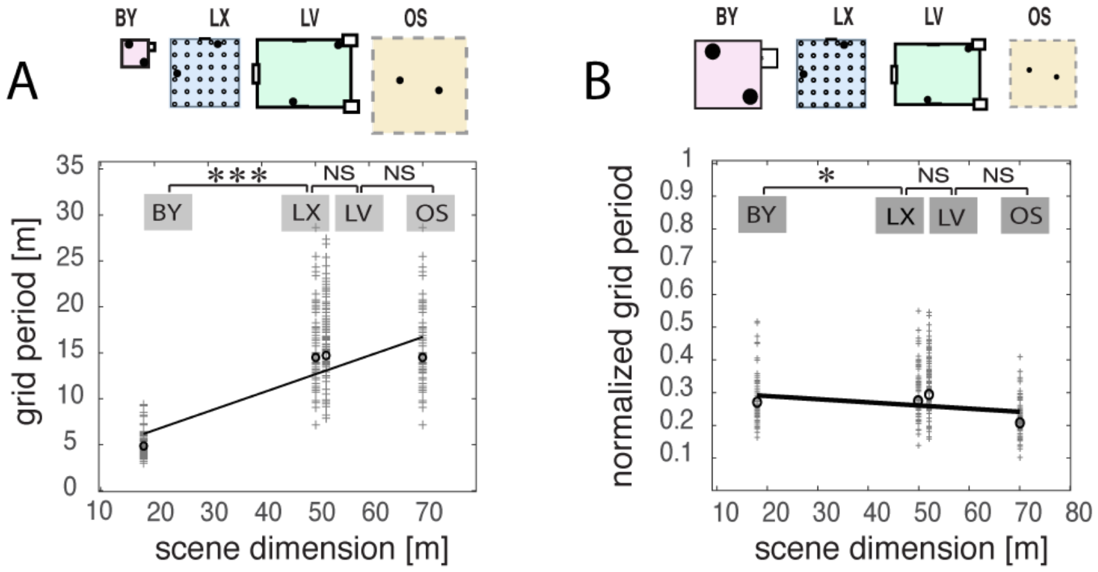

Fig. S6. Correlation between grid period and environmental size at actual and normalized scales in the SPC dataset. (A) Correlation between grid periods and scene dimension. Data points at 18, 50, 52 and 70 correspond with the edge lengths of the four environments. This plot further emphasizes the linear relationship between environment size and grid distance depicted in Fig.3A except this was constructed from the pSPC dataset after combining data from the two subjects (92 neurons that showed significant spatial periodicity in at least 3 environments during the same day). Environments were backyard [BY], Luxor [LX], Louvre [LV], and open space [OS]. The length of the shorter axes of given environments (x) is plotted against the grid period (y). (B) Correlation between grid frequency (normalized grid size) and scene dimension. Same as in (A) except grid periods were normalized by the environment size. After normalization, grid size differences between the small and large environments decreased yet remained significant ($p<0.05$). At the top are the layouts for illustration of the scale differences before and after normalization.

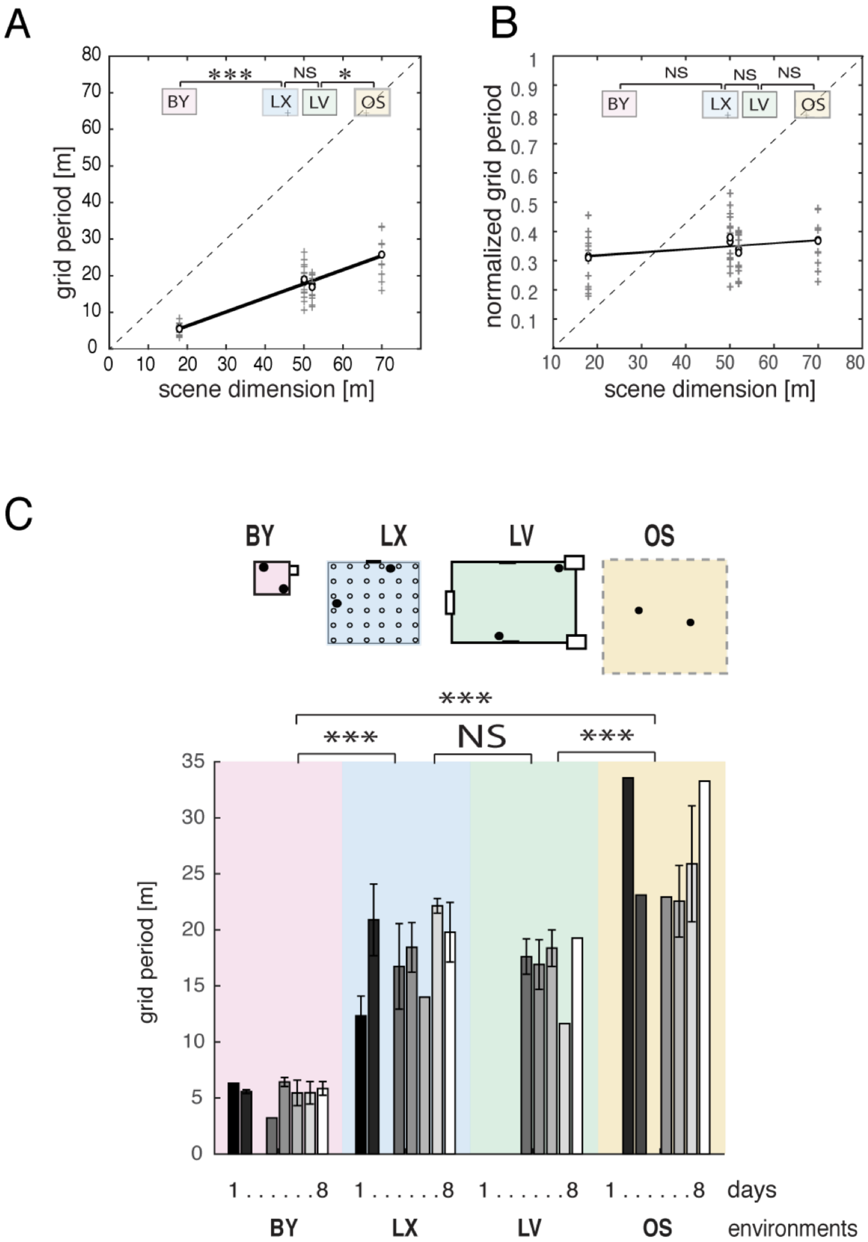

Fig. S7. Correlation between grid period and environmental size at actual and normalized scales within the PGC dataset. (A) Correlation between grid periods and scene dimension. Data points at 18, 50, 52 and 70 correspond with the edge lengths of the four environments in meters. The relationship between environment size and grid distance is linear as also depicted in Fig.3A, except this was constructed from the PGC dataset after combining data from the two subjects (n=73 neurons and 292 trials collected over multiple days). Environments were backyard [BY], Luxor [LX], Louvre [LV], and open space [OS]. The length of the shorter axis of the environment (x) is plotted against the grid period (y). (B) Correlation between grid frequency (normalized grid size) and scene dimension. Same as in (A) except grid periods were normalized by the environment size. After normalization, grid size differences between the small and large environments disappeared (NS). The straight lines represent linear regression of the data points. (C) Daily variation of grid periods grouped according to environments. Black bars represent first days and open bars represent last days. Missing bars correspond to days when no putative grid cells were observed. Error bars are SE of the mean. The insets above the bars illustrate the scale-proportionate layouts of the environments corresponding to the four groups of grid periods.

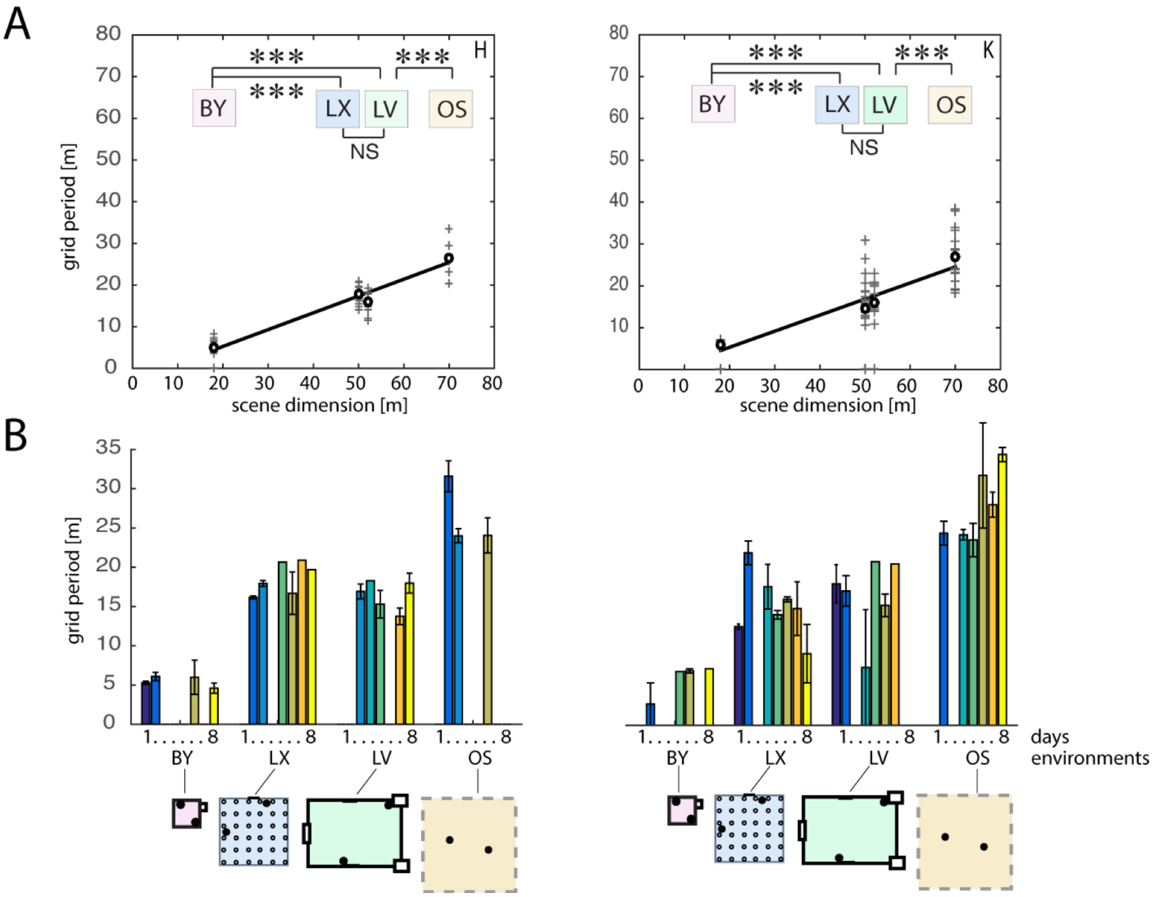

Fig. S8. Correlation between grid period and environmental in the PGC$_{hi\text{-}conf}$ dataset. (A) Correlation between grid periods and scene dimension for subject H and K (left and right side plot, respectively). Open circles represent mean grid periods. Lines depict the linear regression of the data points represented by + symbols. Data points at 18, 50, 52 and 70 correspond with the edge lengths of the four environments in meters. The relationship between environment size and grid distance is linear as also depicted in Fig.3A S5 and S6, except this was constructed from the PGC$_{hi\text{-}conf}$ dataset. Environments were backyard [BY], Luxor [LX], Louvre [LV], and open space [OS]. The length of the shorter axis of the environment (x) is plotted against the grid period (y). (B) Daily variation of grid periods grouped according to environments. Dark blue bars represent the first days and yellow bars represent last days. Missing bars correspond to days when none of the single units classified as PGC$_{hi\text{-}conf}$. Error bars are SE of the mean. The insets below the bar charts illustrate the scale-proportionate layouts of the environments.

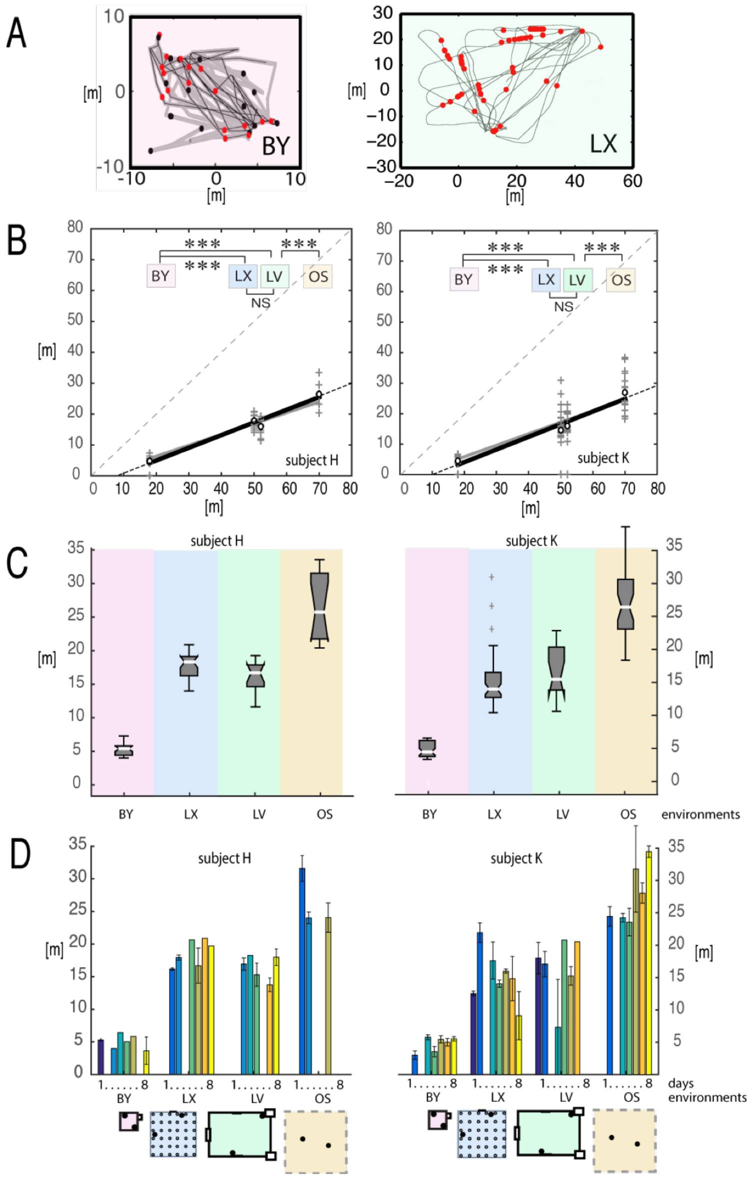

Fig. S9. Correlation between grid period and environmental size in the PGC$_{hi\text{-}conf}$ dataset under balanced environmental coverages. (A) The layouts of the backyard (BY) and Louvre (LV) environments with trajectories and single unit activity, indicated by red and black symbols, during 5 virtual navigations. Environments are scaled differently. To balance the differential density of spatial coverages between the BY and LX, LV and OS environments, we reduced the navigation path in the BY environment to the 50% its original length (black lines overlaid on gray trajectories). This resulted in a reduction of single unit activity recorded as well (red symbols) relative to the total single unit activity (red and black symbols) without changing the average firing rate. (B) Correlation of grid distance with environment size under balanced spatial coverage for the two subjects shown separately (subject H and K at the left and right, respectively). The slopes of linear regressions (f(x)=.4108x-3.241 and f(x)=.4153x-4.218) did not change relative to the slopes obtained from the complete datasets (dotted gray line from Fig. 3, also Fig. S5 and S6). (C) Median grid sizes and quartiles in four different environments. The central notches are medians and boxes contain the 2nd and 3rd quartiles of data. (D) Daily average grid distances and SE of the mean for the two patient participants side by side. At the bottom, we illustrate the size differences between virtual environments on the same scale.

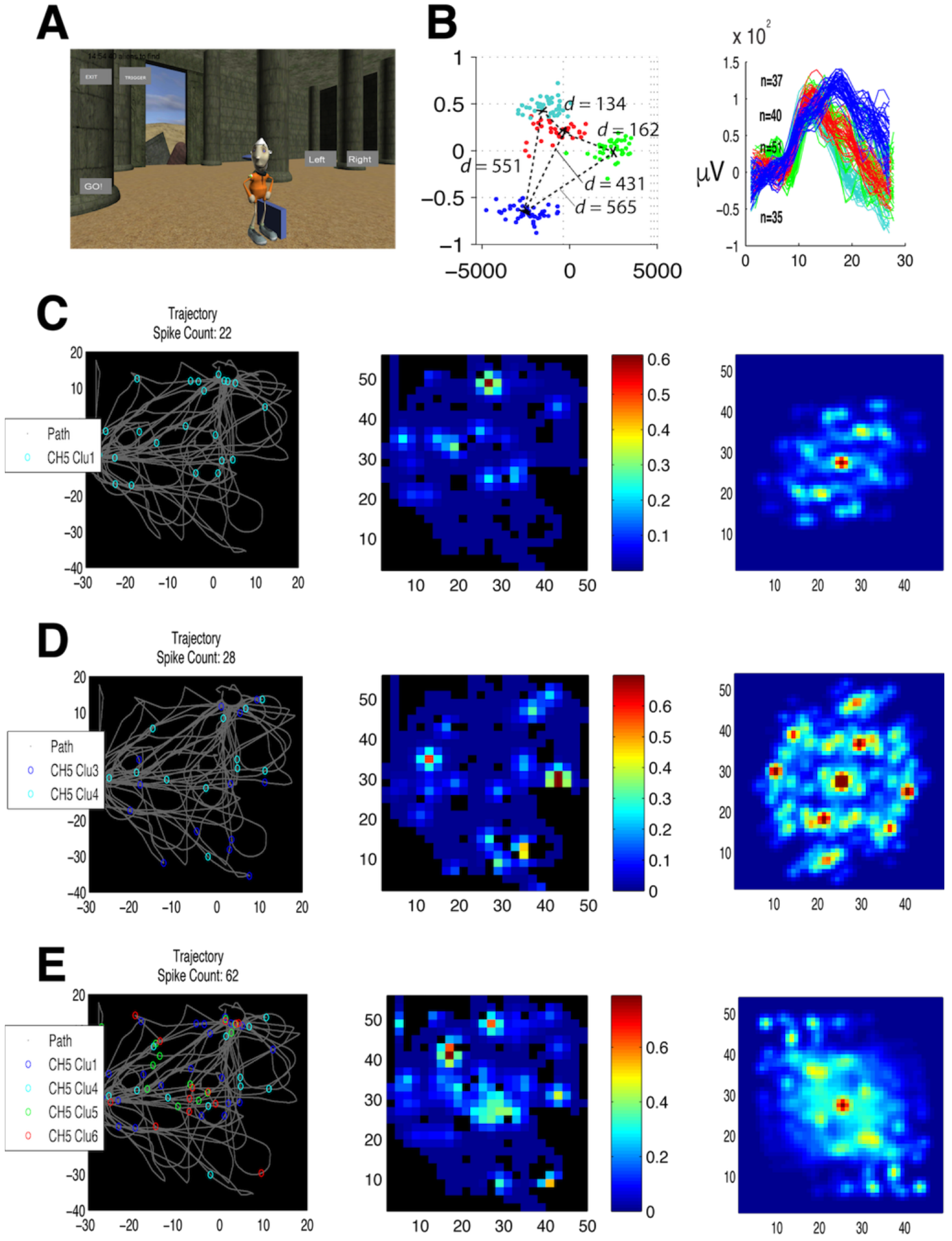

Fig. S10. Combination of simultaneously recorded SUA from the same electrode in the same environment completes grid-like firing-rate maps. (A) All maps were derived from the same 5 min recording session during navigation in the Luxor environment. (B) The two-dimensional projection of four clusters of single unit activity (SUA) isolated from recordings across 4 environments and their corresponding waveforms. Cluster separation was quantified by Mahalanobis distance *d*. (C-E) Incremental combination of SUA derived from SUA clusters 1, 2, 3, 4, respectively. Panels in the first column represent the spatial map of SU activity. The second column depicts the corresponding spatial firing-rate maps from the combined SUA. The third column displays the corresponding spatial ACs. The hexagonal grid in the third column of (c-e) illustrates that the combined SUA nodes are consistent with a hexagonal tessellation pattern. Note the increasing coverage of space while the hexagonal tessellation of the autocorrelation alters the grid geometry in the ACs. Scales are in [m].

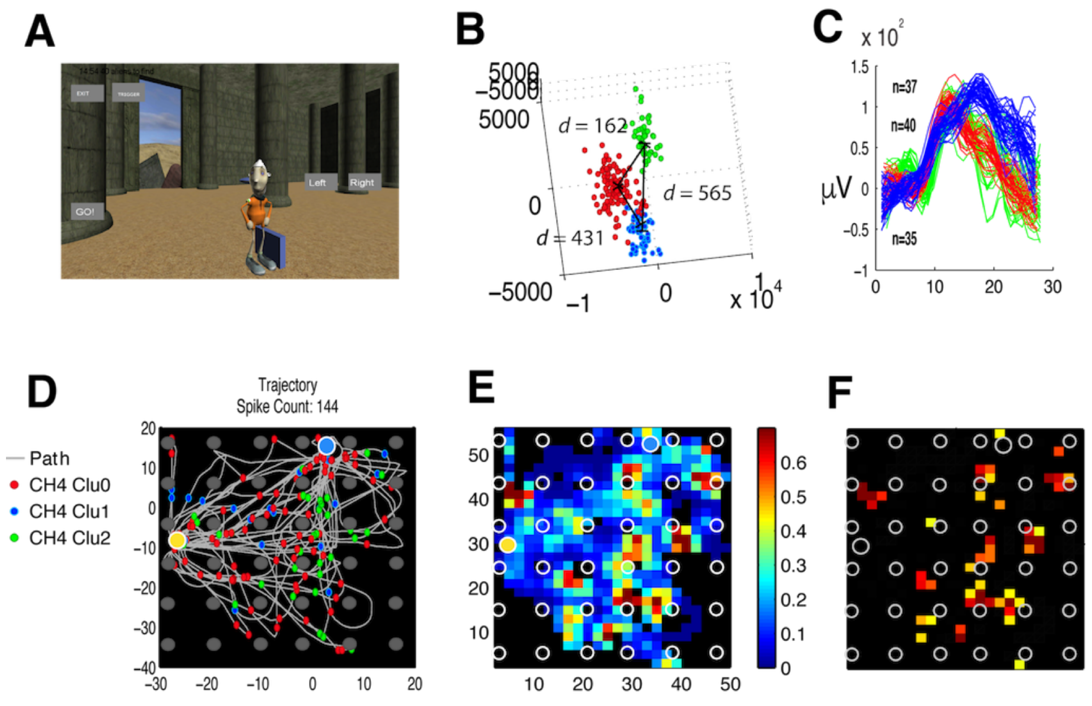

Fig. S11. Independence of grid scaling from obstacles. (A) Maps were computed from a 10 min recording session during navigation in the Luxor environment. (B,C) Three single unit activity (SUA) clusters and their corresponding waveforms are shown out of the four cells isolated from the same electrode (three of the same SUAs as on Fig. S5). Mahalanobis distances between pairs of single unit clusters are indicated (*d*). (D) The superimposed firing locations of the three putative neurons projected on the layout of the environment. Gray circles represent pillars in the space. (E) Spatial firing rate map of the combined activity of 3 putative neurons on the full scale of firing rates and (F) when the firing rates are clipped to the upper third. The observation that grid density appears to be less than the density of obstacles suggests the independence of grid scaling from the obstacles in the environment. Scales are in [m].

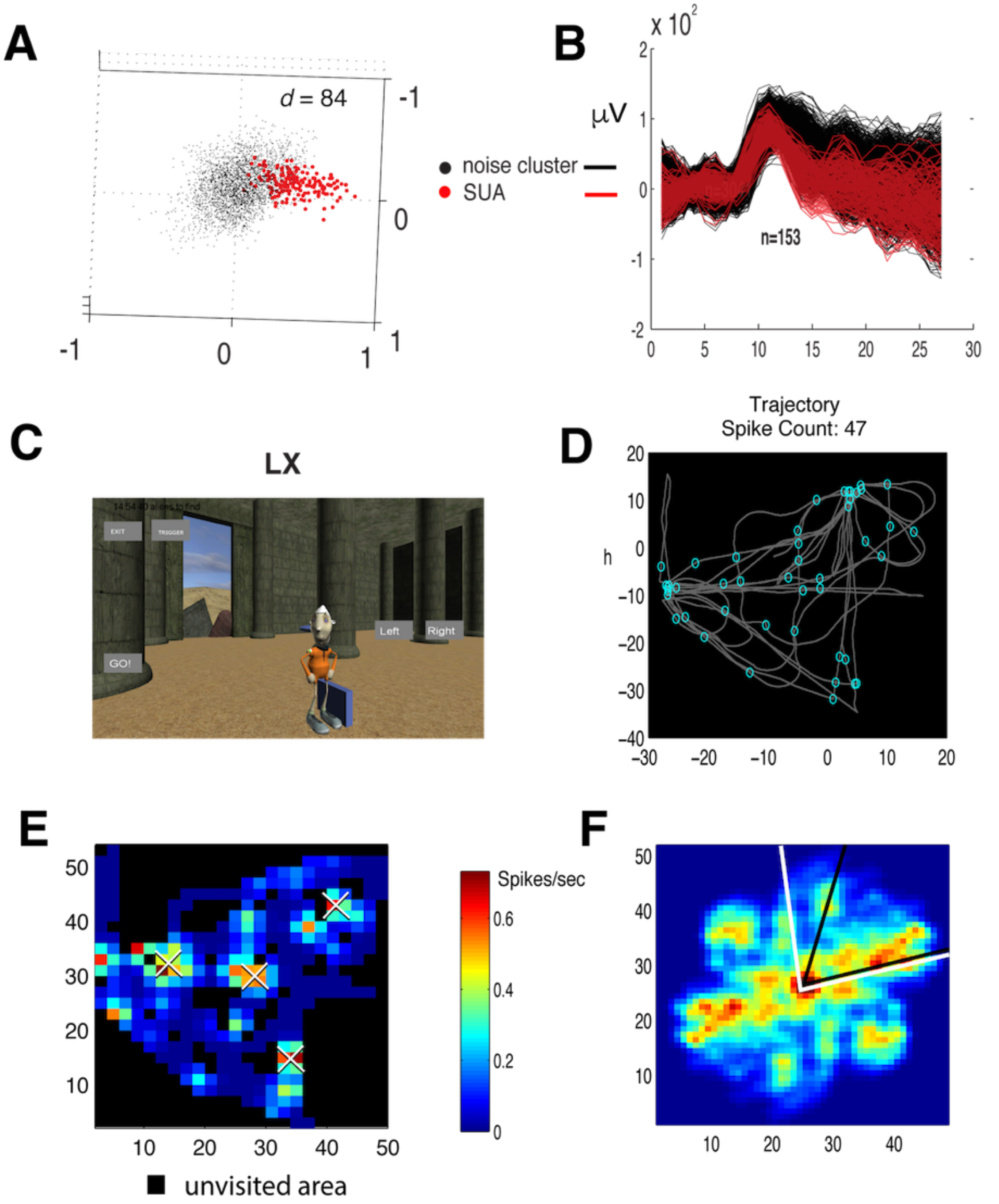

Bin Size: 2x2m, D: 20.8087m, Grid Angle: 54.7824

Bin Size: 2x2m Avg FR: 0.15705 Max FR: 2.8409 Grid Mod: 0.28353 Grid Spokes: 2 Spoke Angles: 58 87 Peaks: 8

Fig. S12. Example cell #01. (A) Spike waveforms were classified into feature clusters. A 3D subspace of the multidimensional feature-space is shown. A cluster of spikes (red dots) was isolated against the noise (black cloud) by using superparamagnetic clustering (see Methods). This cluster captures single-unit activity of a putative neuron that is mapped in (D-F). Cluster separation was quantified by Mahalanobis distance *d.* (B) The corresponding waveforms of the SUA and noise clusters superimposed. (C) The SUA was recorded during a 5 min session in the Luxor environment. (D) The firing locations of the SUA projected on the layout of the environment. Cyan circles represent the spatial registration of SUA and the gray line is the path taken. (E) Spatial firing rate map of the SUA. (F) Corresponding spatial autocorrelogram shows 60° rotational symmetry. Scales are in [m].

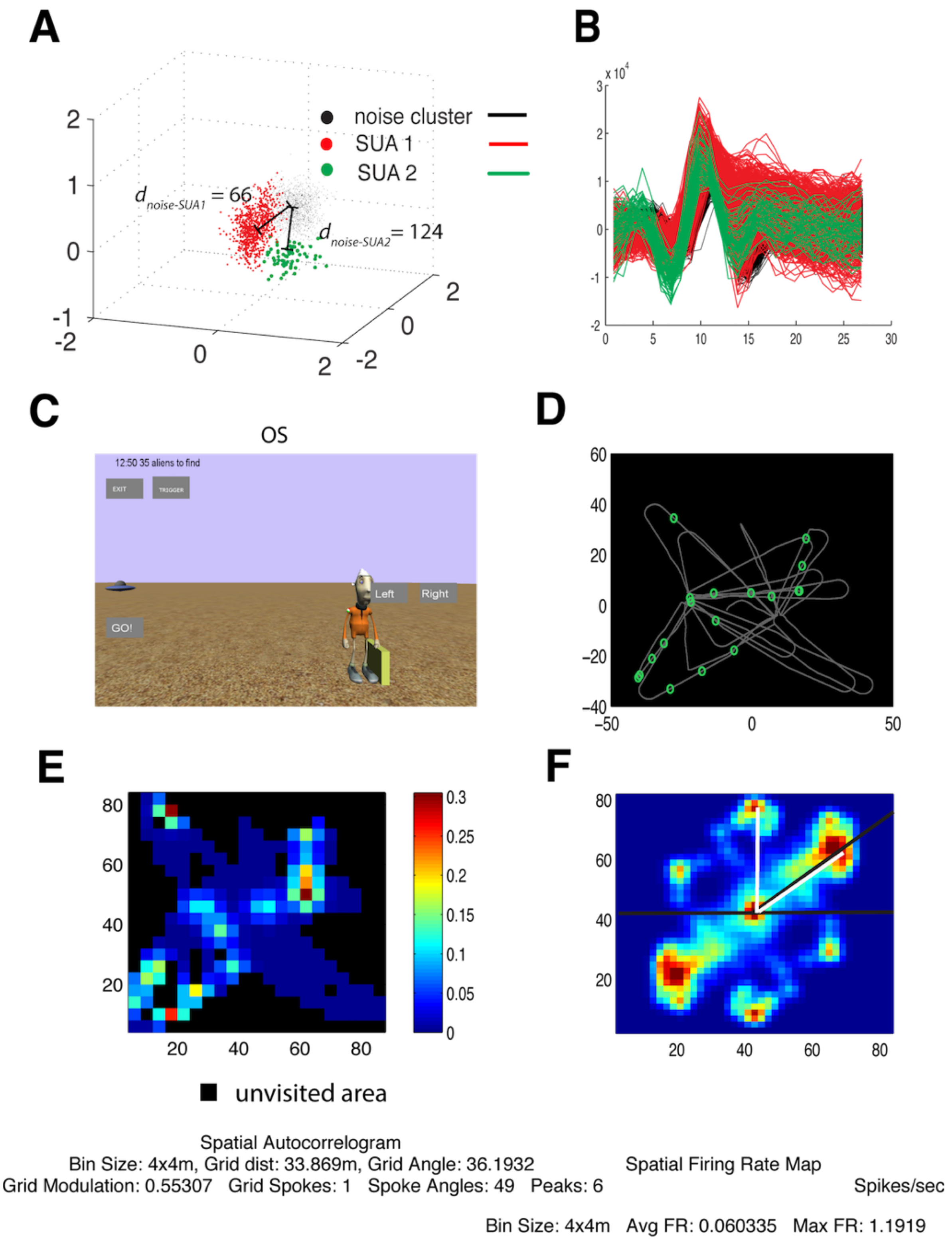

Spatial Autocorrelogram

Bin Size: 4x4m, Grid dist: 33.869m, Grid Angle: 36.1932

Grid Modulation: 0.55307 Grid Spokes: 1 Spoke Angles: 49 Peaks: 6

Spatial Firing Rate Map

Spikes/sec

Bin Size: 4x4m Avg FR: 0.060335 Max FR: 1.1919

Fig. S13. Example cell #02. The organization of the panels is the same as in example Cell#01. (A) Two putative neurons were discriminated (SUA1 and SUA2 as red and green dots, respectively) against the noise cluster (black dots). Cluster separation was quantified by Mahalanobis distance *d.* (B) Corresponding waveforms. (C) Cells were recorded during a 5 min session in the Open environment. (D) The firing locations of putative neuron identified as SUA 2 projected on the layout of the environment. Green circles represent SUA2, gray line is the path taken. (E) Spatial firing rate map of the SUA. (F) Corresponding spatial autocorrelogram shows 45° rotational symmetry. Scales are in [m].

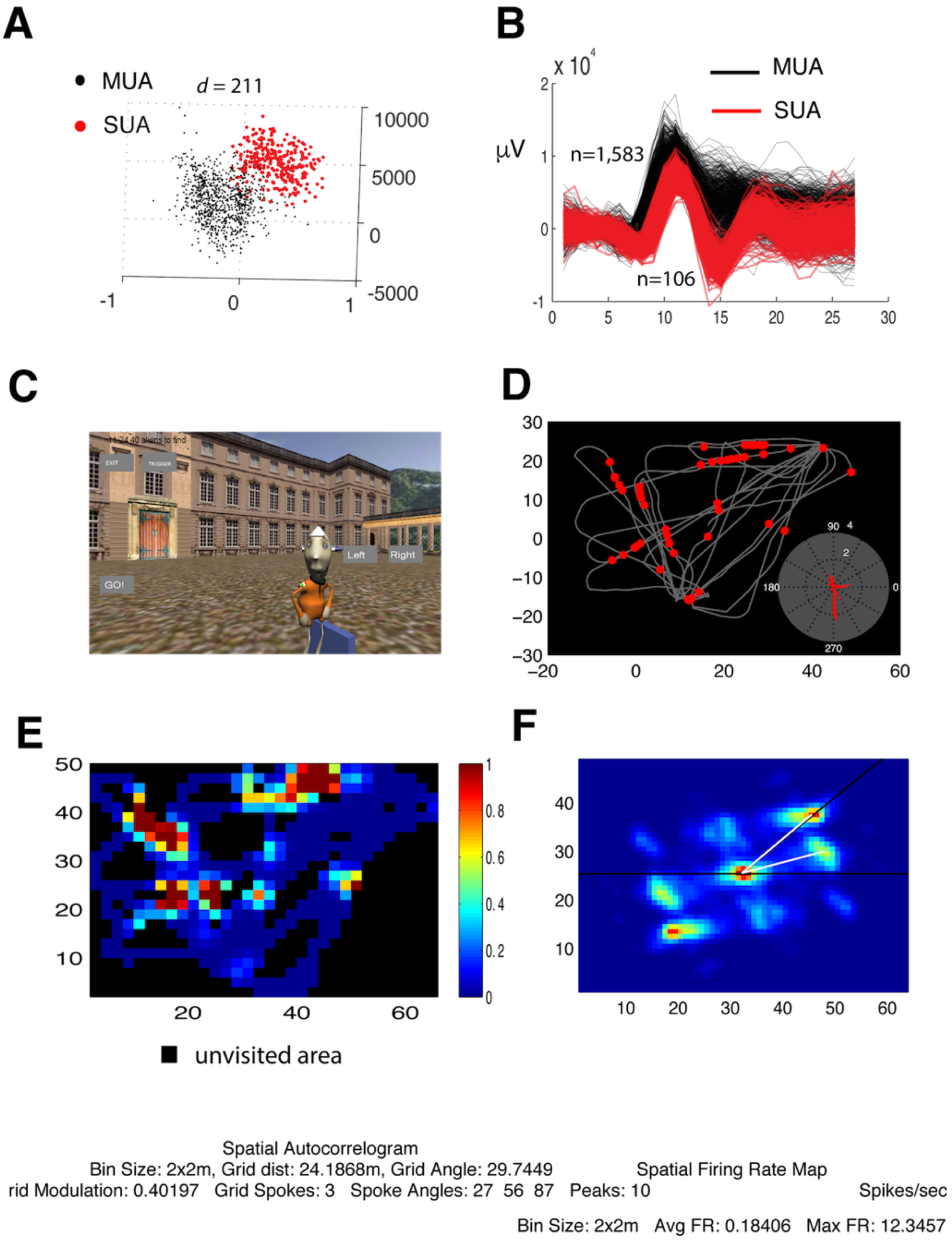

Fig. S14. Example cell #03. The organization of the panels is the same as in example Cell#01. (A) One putative neuron was discriminated (red markers: SUA) against the noise cluster (black markers: MUA). Cluster separation was quantified by Mahalanobis distance *d.* (B) Corresponding waveforms. (C) Cells were recorded during a 5 min session in the Louvre environment. (D) The firing locations of the SUA projected on the layout of the environment. Red circles represent SUA, gray line is the path traveled. Inset represent head direction tuning. (E) Spatial firing rate map of the SUA. (F) Corresponding spatial autocorrelogram shows 29° rotational symmetry. Scales are in [m].

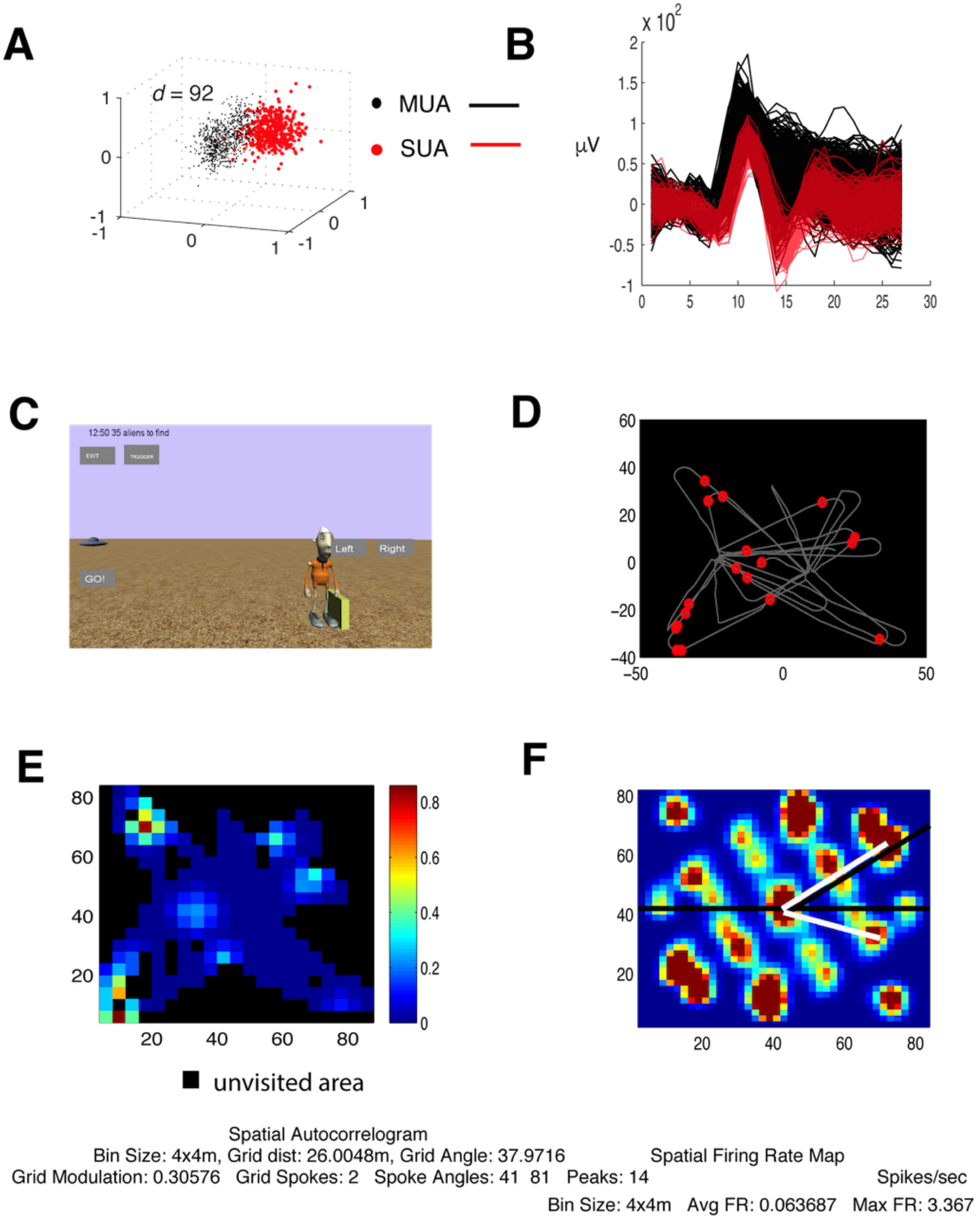

Fig. S15. Example cell #04. The organization of the panels is the same as in example Cell#01. (A) One putative neuron was discriminated (red markers: SUA) against the noise cluster (black markers: MUA). Cluster separation was quantified by Mahalanobis distance *d.* (B) Corresponding waveforms. (C) Cells were recorded during a 5 min session in open environment (OS). (D) The firing locations of the SUA projected on the layout of the environment. Red circles represent SUA, gray line is the path traveled. (E) Spatial firing rate map of the SUA. (F) Corresponding spatial autocorrelogram shows 38° rotational symmetry. Scales are in [m].

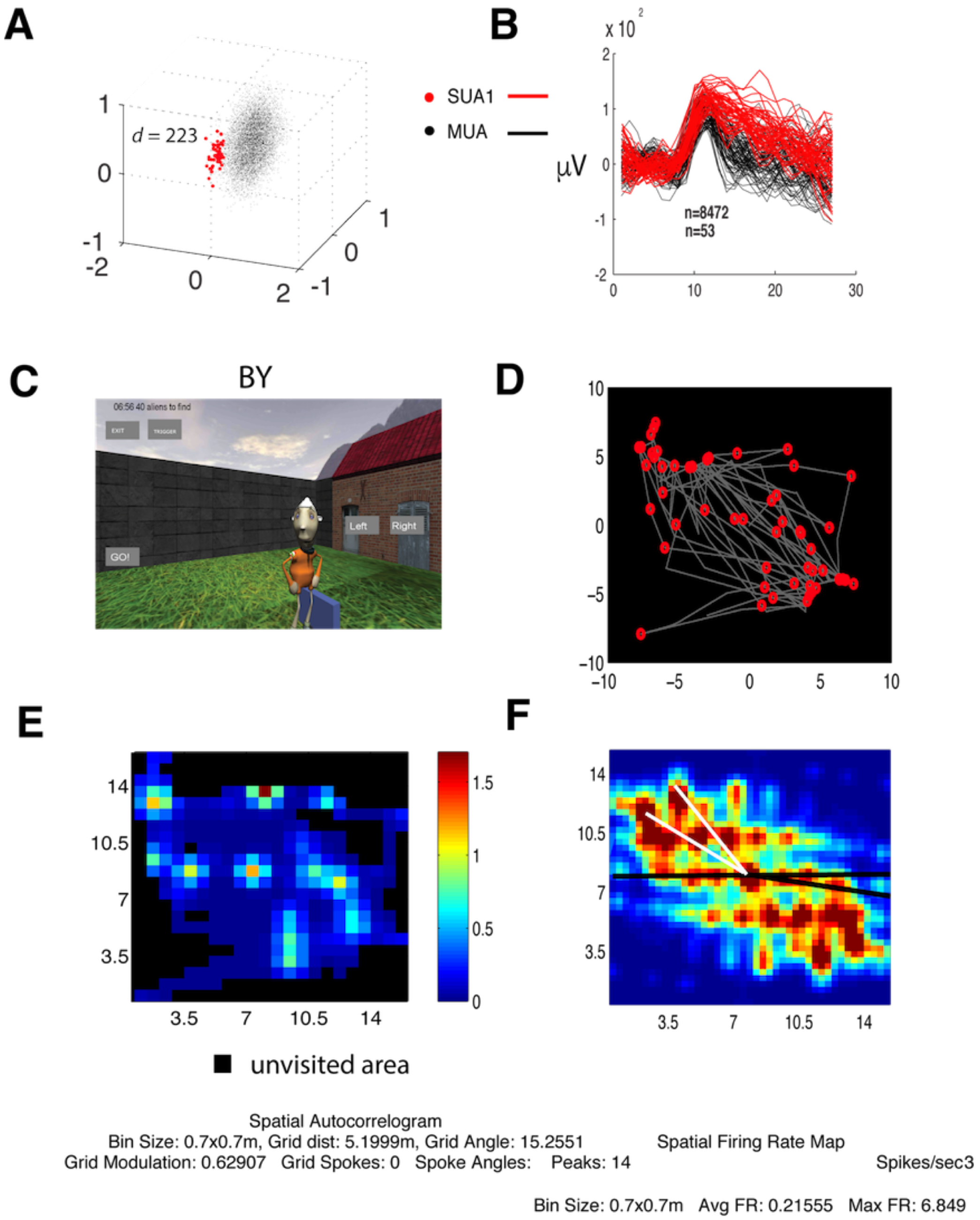

Fig. S16. Example cell #05. The organization of the panels is the same as in example Cell#01. (A) Waveform clustering displays a well-isolated SUA1 (red dots) and a homogeneous multiunit cluster (black cloud). Cluster separation was quantified by Mahalanobis distance *d.* (B) Corresponding waveforms superimposed. (C) The spatial maps of the neuronal activity were constructed during a 5 min spatial task in the Backyard environment. (D) The firing locations of the SUA1 projected on the layout of the environment. Red circles represent SUA1, gray line is the path taken. (E) Spatial firing rate map of the SUA and (F) the corresponding spatial autocorrelogram, displaying 14, 28, and 42° rotational symmetries. Scales are in [m].

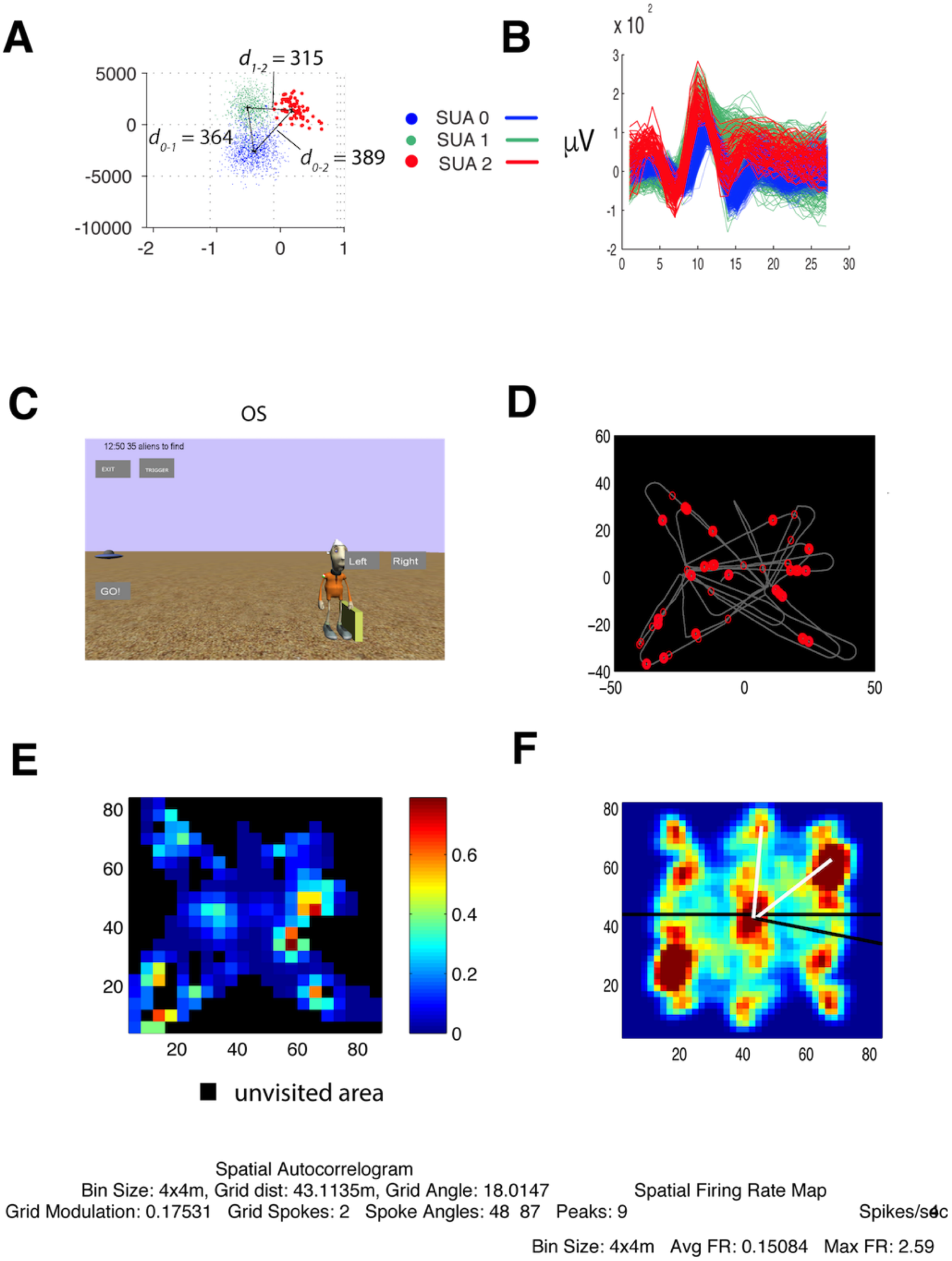

Fig. S17. Example cell #06. The organization of the panels is the same as in example Cell#01. (A) Waveform clustering discriminated three well-isolated single unit clusters (red, green and blue dots). Pairwise Mahalanobis distances between clusters are indicated by *d* values. (B) Corresponding waveforms superimposed. (C) Spatial maps were derived from 5 min navigation in the Open environment. (D) The firing locations of the SUA2 projected on the layout of the environment. Red circles represent spikes of SUA2, gray line is the path taken. (E) Spatial firing rate map of the SUA2 and (F) the corresponding spatial autocorrelogram, displaying 48° and 87° rotational symmetries. Scales are in [m].

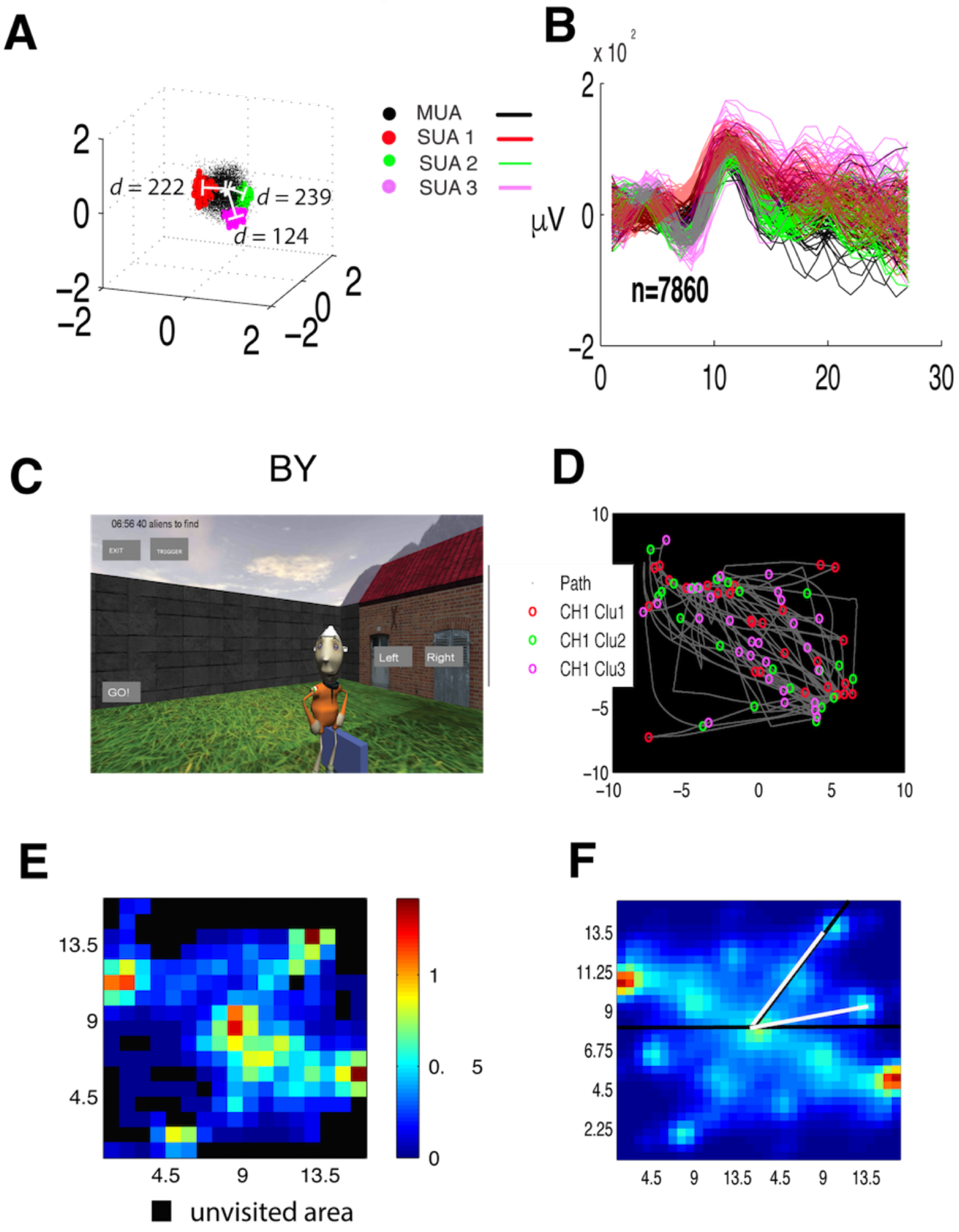

Spatial Autocorrelogram

Bin Size: 0.9x0.9m, Grid dist: 4.7543m, Grid Angle: 51.3402 Spatial Firing Rate Map

Grid Modulation: 0.26879 Grid Spokes: 2 Spoke Angles: 43 80 Peaks: 9 Spikes/sec

Bin Size: 0.9x0.9m Avg FR: 0.29573 Max FR: 5.4054

Fig. S18. Example cell #07. The organization of the panels is the same as in example Cell#01. (A) Waveform clustering discriminated three single unit clusters (red, green and magenta dots) that were isolated from one another as well as from the noise cluster (black cloud). Cluster separations between the central noise and individual clusters indicated by the Mahalanobis distances *d.* (B) Corresponding waveforms superimposed. (C) Spatial maps were derived from 5 min navigation in the Backyard environment. (D) The firing locations of the SUA1-2-3 projected on the layout of the environment. Red, green and magenta circles represent spikes of SUA1,2 and 3, respectively. Gray line is the path taken. (E) Spatial firing rate map of the combined SUA spikes and (F) the corresponding spatial autocorrelogram, displaying 43° and 80° rotational symmetries. Scales are in [m].

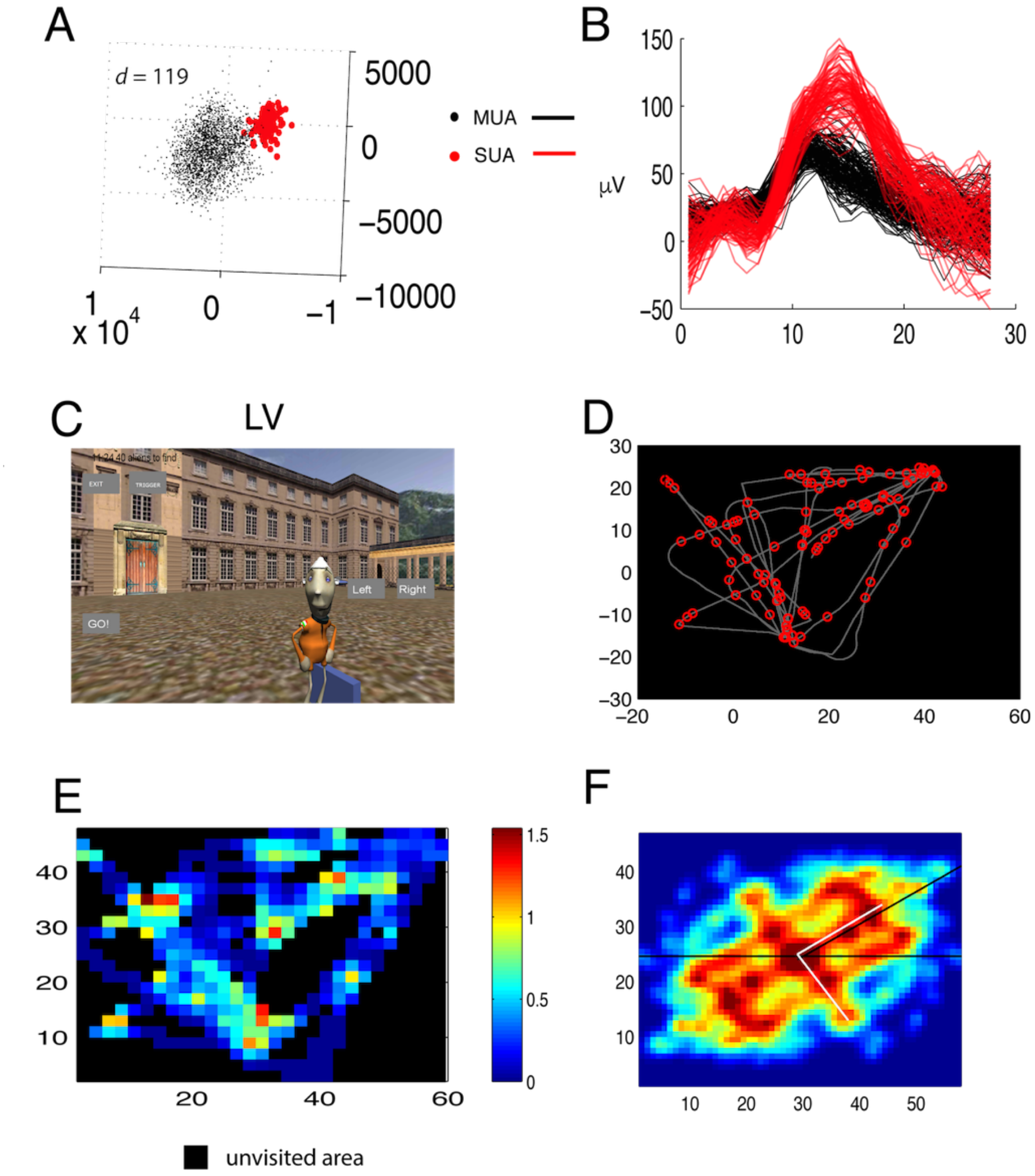

Spatial Autocorrelogram
Bin Size: 2x2m, Grid dist: 21.1102m, Grid Angle: 25.8368
Grid Modulation: 0.40016 Grid Spokes: 1 Spoke Angles: 87 Peaks: 7

Spatial Firing Rate Map
Spikes/sec
Bin Size: 2x2m Avg FR: 0.39475 Max FR: 5

Fig. S19. Example cell #08. The organization of the panels is the same as in example Cell#01. (A) One single unit cluster (red dots) was isolated from the noise cluster (black cloud). Cluster separation was quantified by Mahalanobis distance *d.* (B) Corresponding waveforms superimposed. (C) Spatial maps were derived from 5 min navigation in the Louvre environment. (D) The firing locations of the SUA projected on the layout of the environment. Red circles represent spikes of SUA. Gray line is the path taken. (E) Spatial firing rate map of the SUA spikes and (F) the corresponding spatial autocorrelogram, displaying 87° rotational symmetry. Scales are in [m].

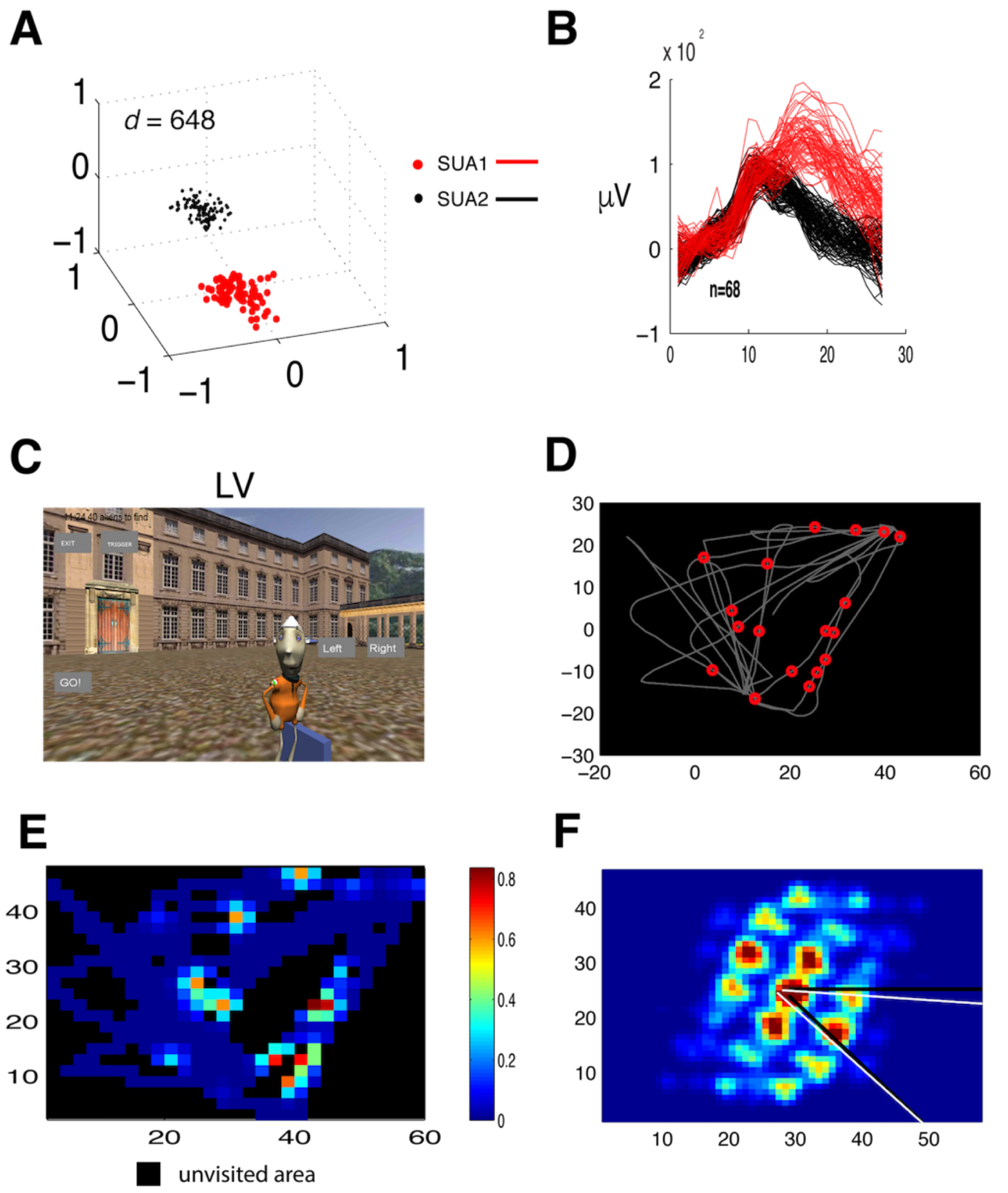

Spatial Autocorrelogram
Bin Size: 2x2m, Grid dist: 20.9326m, Grid Angle: 47.0972
Grid Modulation: 0.25685 Grid Spokes: 2 Spoke Angles: 45 87 Peaks: 12

Spatial Firing Rate Map
Spikes/sec
Bin Size: 2x2m Avg FR: 0.064105 Max FR: 2.7027

Fig. S20. Example cell #09. The organization of the panels is the same as in example Cell#01. (A) The waveform clustering shows two well-isolated single unit clusters (red and black cloud of dots). Cluster separation was quantified by Mahalanobis distance *d.* (B) Corresponding waveforms superimposed. (C) The spatial activity of cells was tracked during a 5 min memory driven navigation task in the Louvre environment. (D) The firing locations of the SUA2 projected on the layout of the environment. Red circles represent SUA2, gray line is the path taken. (E) Spatial firing rate map of the SUA and (F) the corresponding spatial autocorrelogram, displaying 45° rotational symmetry. Scales are in [m].

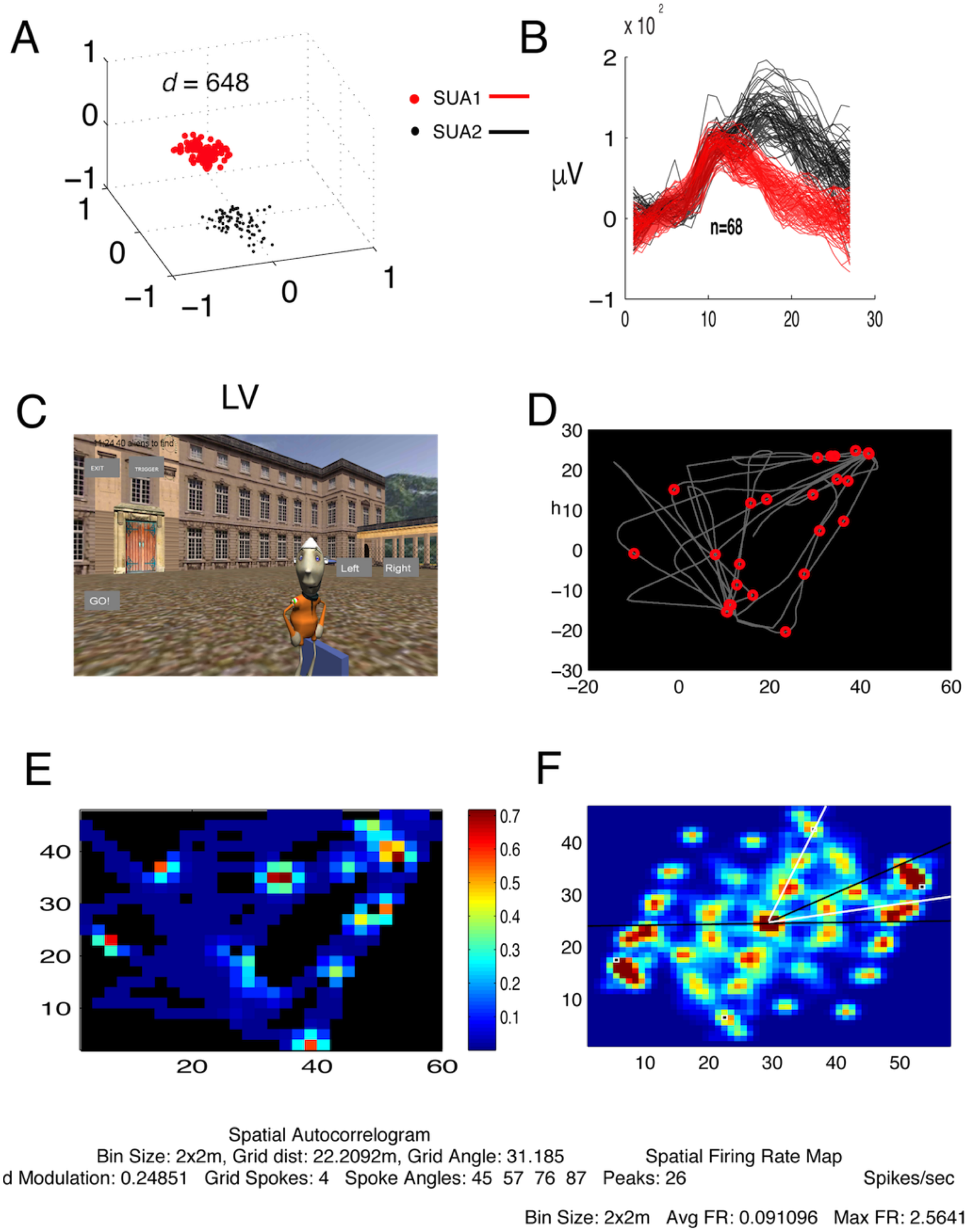

Fig. S21. Example cell #10. The organization of the panels is the same as in example Cell#01. (A) Same cell clusters as shown in Fig. S17: Example cell #9. The waveform clustering shows two well-isolated single unit clusters (red and black cloud of dots). Cluster separation was quantified by Mahalanobis distance *d.* (B) Corresponding waveforms superimposed. (C) The spatial maps of the neuronal activity were constructed during a 5 min spatial task in the Louvre environment. (D) The firing locations of the SUA1 projected on the layout of the environment. Red circles represent SUA1, gray line is the path taken. (E) Spatial firing rate map of the SUA and (F) the corresponding spatial autocorrelogram, displaying 57° rotational symmetry. Scales are in [m].

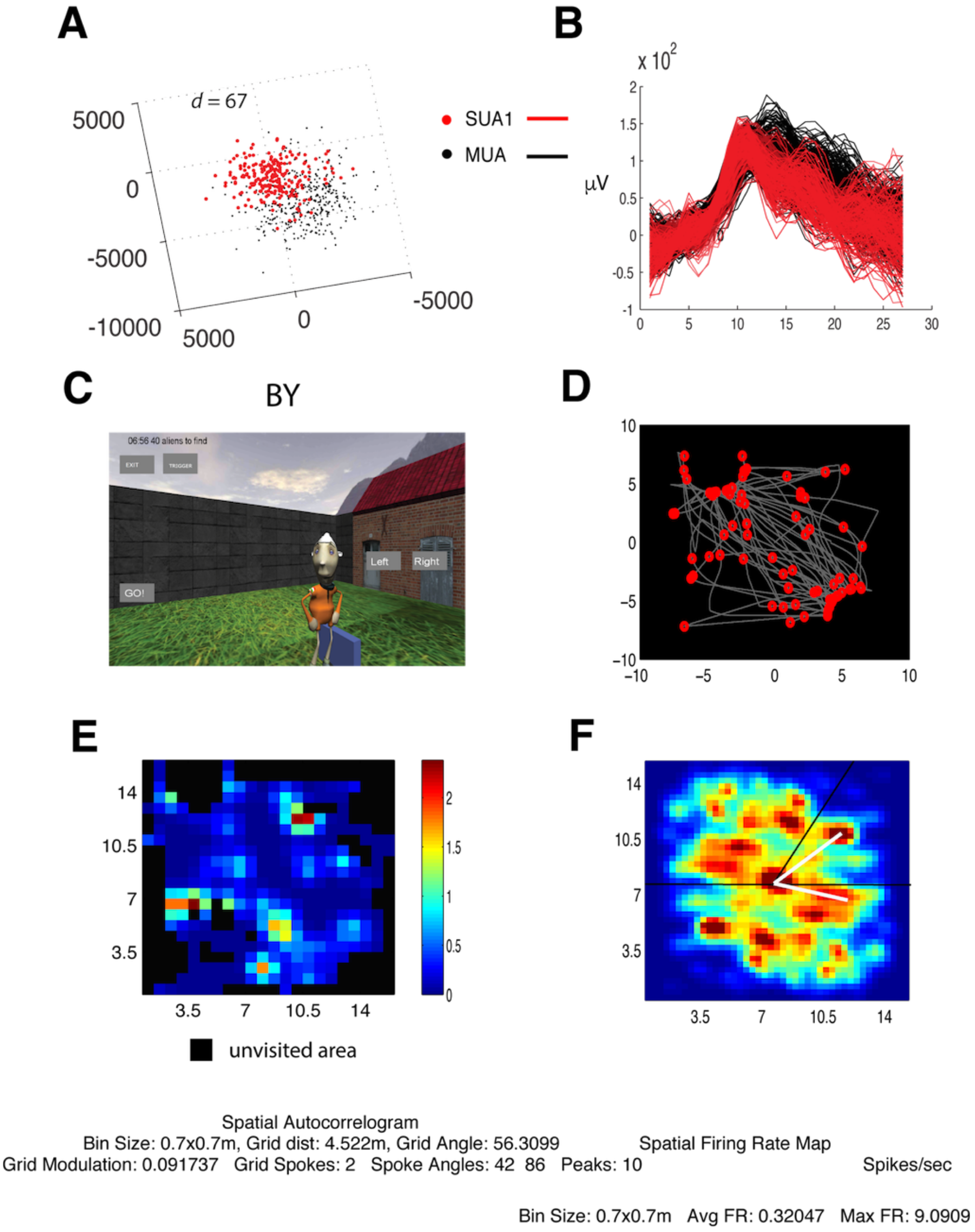

Fig. S22. Example cell #11. The organization of the panels is the same as in example Cell#01. (A) A single unit cluster (red dots) isolated from the noise cluster (black cloud of dots) is shown. Cluster separation was quantified by Mahalanobis distance *d.* (B) Corresponding waveforms superimposed. (C) The SUA1 neuronal activity was recorded during a 5 min session in the Backyard environment. (D) The firing locations of the SUA projected on the layout of the environment. Red circles represent SUA, gray line is the path taken. (E) Spatial firing rate map of the SUA. (F) Corresponding spatial autocorrelogram shows 42° rotational symmetry. Scales are in [m].

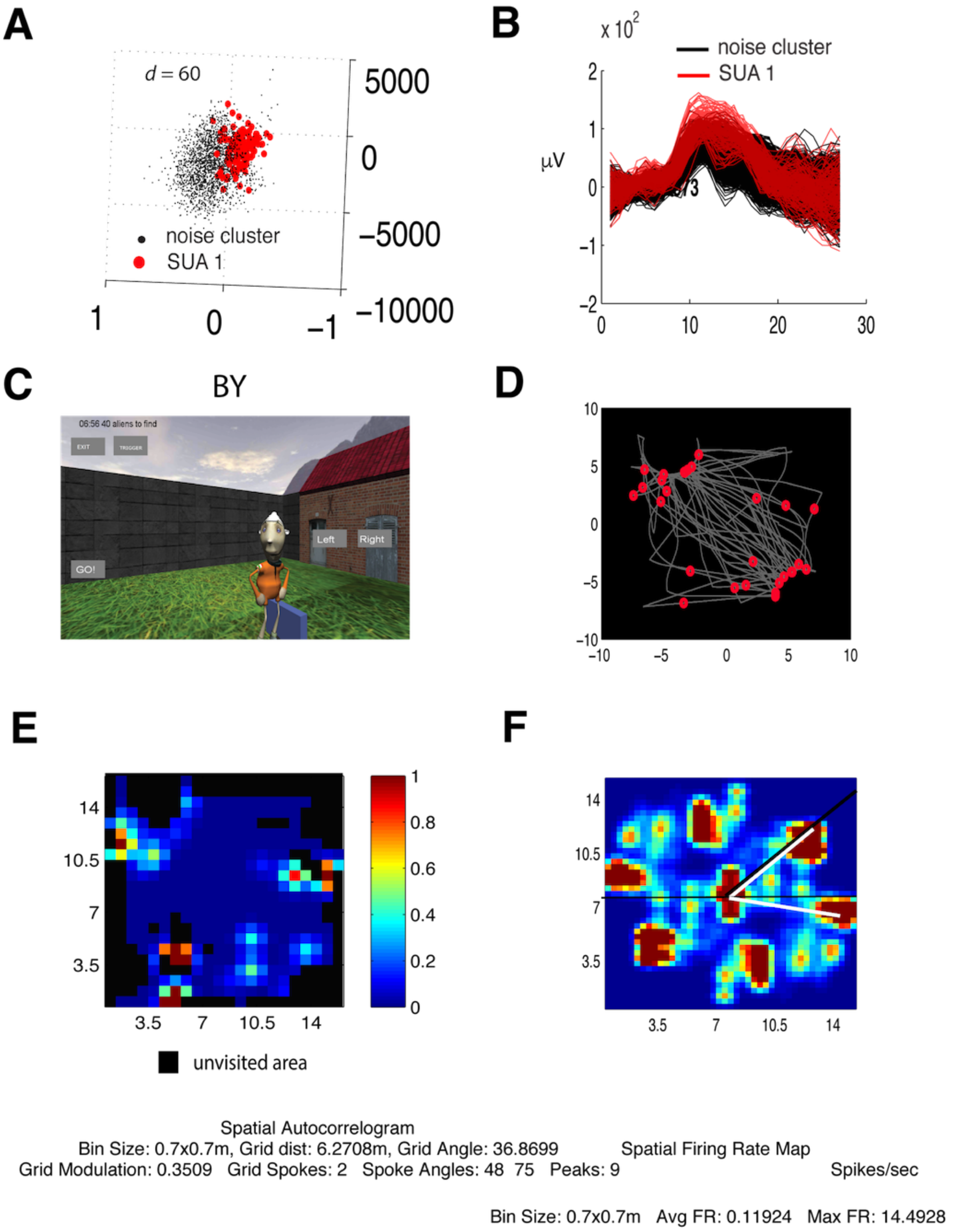

Fig. S23. Example cell #12. The organization of the panels is the same as in example Cell#01. (A) The waveform clustering shows the isolation of a single unit cluster (red) from the background multiunit noise cloud (black dots). Cluster separation was quantified by Mahalanobis distance *d.* (B) Corresponding waveforms superimposed. (C) The spatial maps on (d-f) were derived from neuronal activity recorded during a 5 min spatial task in the Backyard environment. (D) The firing locations of the SUA projected on the layout of the environment. Red circles represent SUA, gray line is the path taken. (E) Spatial firing rate map of the SUA. (F) Corresponding spatial autocorrelogram shows 48° rotational symmetry. Scales are in [m].

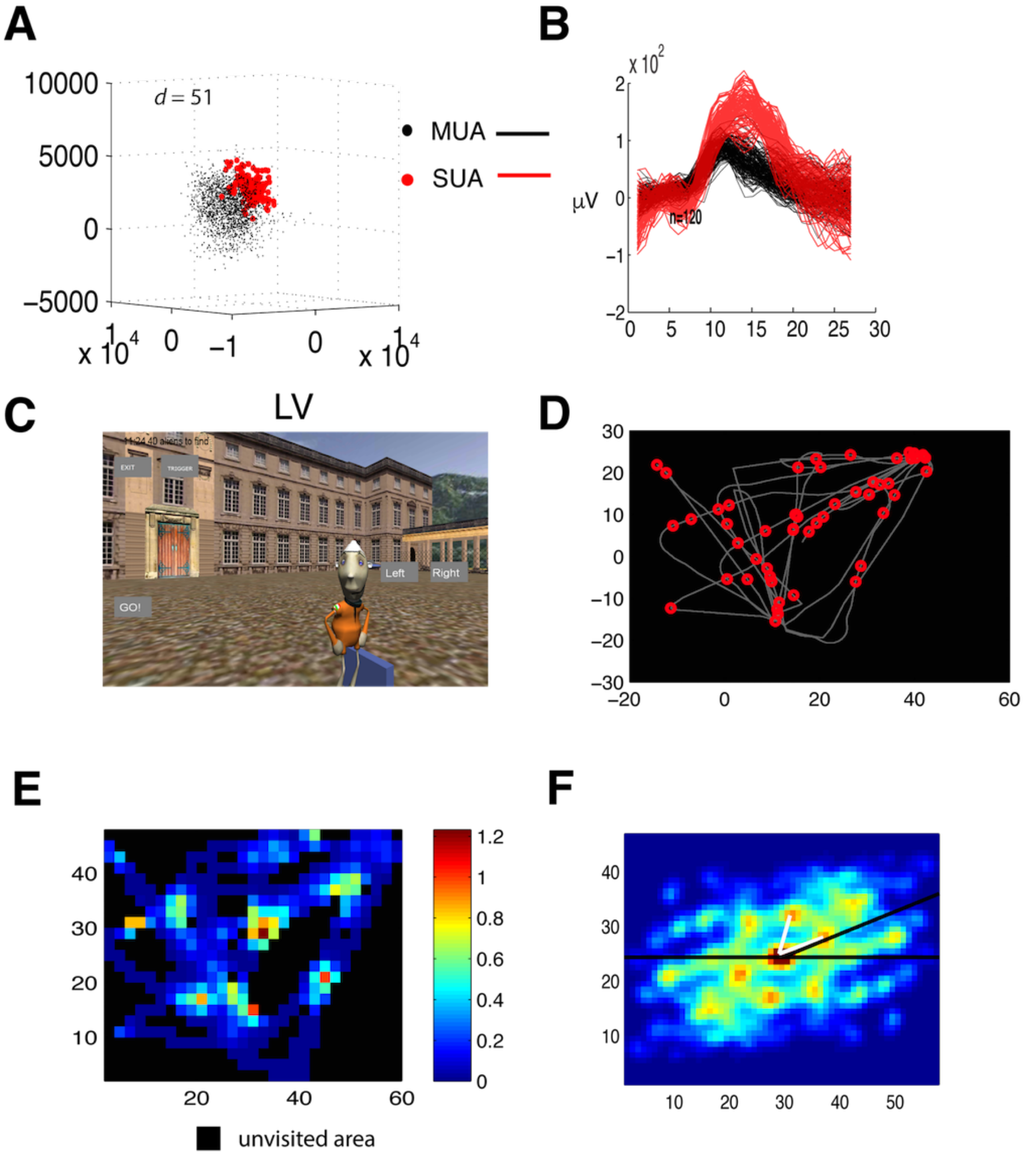

Spatial Autocorrelogram
Bin Size: 2x2m, Grid dist: 12.286m, Grid Angle: 48.4882
Grid Modulation: 0.36322 Grid Spokes: 1 Spoke Angles: 87 Peaks: 14

Spatial Firing Rate Map
Spikes/sec

Bin Size: 2x2m Avg FR: 0.18894 Max FR: 3.937

Fig. S24. Example cell #13. The organization of the panels is the same as in example Cell#01. (A) The spike waveform clustering revealed a single unit (red dots) separated from multiunit activity and noise (black cloud of dots). Cluster separation was quantified by Mahalanobis distance *d.* (B) Corresponding waveforms superimposed. (C) The illustrated cell was followed during a 5 min session in the Louvre environment. (D) The firing locations of the SUA projected on the layout of the environment. Red filled circles represent SUA, gray line is the path taken. (E) Spatial firing rate map of the single putative neuron. (F) Corresponding spatial autocorrelogram with the cardinal angles of the grid spokes. Rotation symmetry is ~60°. Scales are in [m].

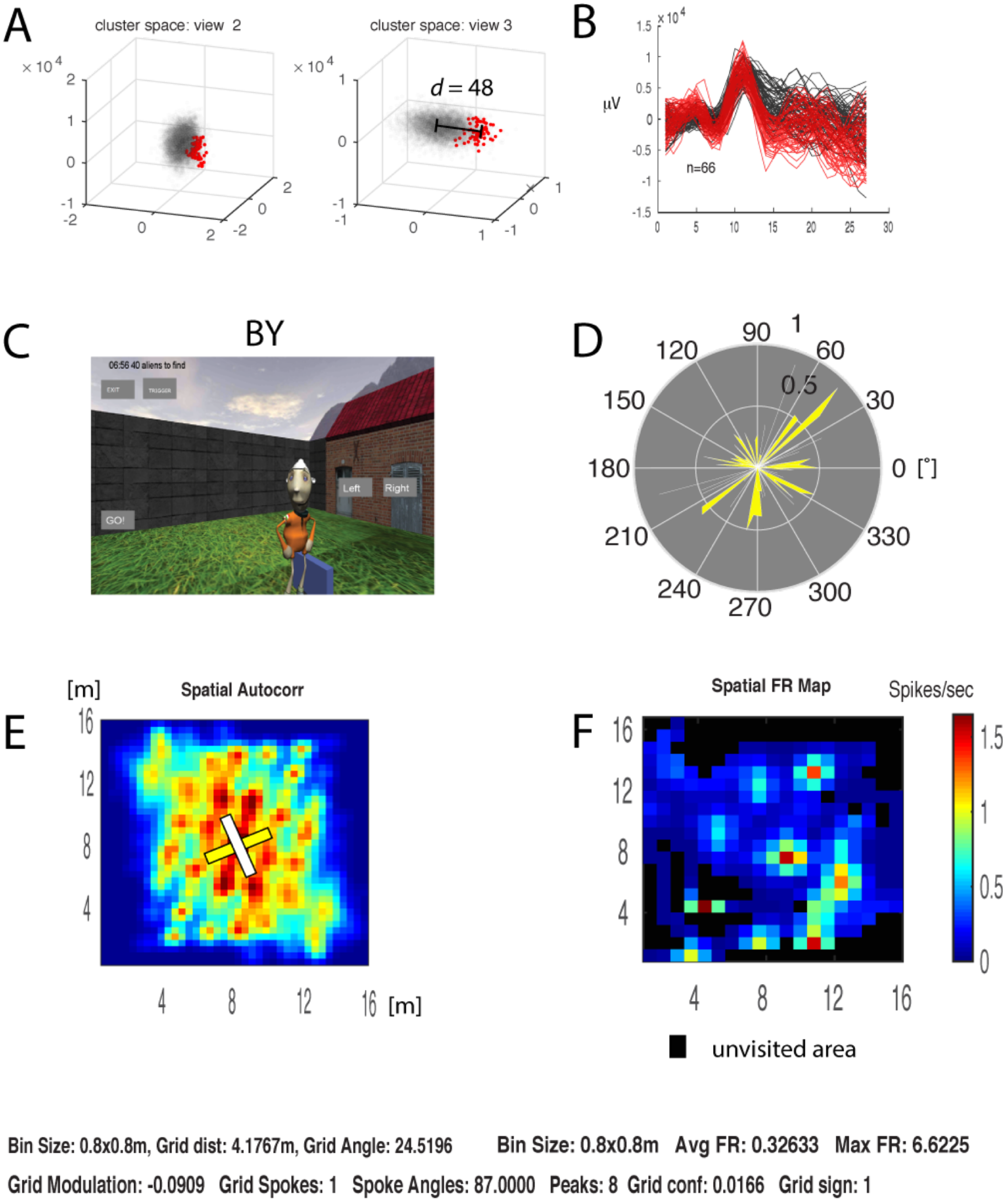

Fig. S25. Example cell #14. The organization of the panels is similar to the example Cell#01 except panel (D) featuring the directional tuning of the single unit activity. (A) The spike waveform clustering revealed a single unit (red dots) separated from multiunit activity and noise (black cloud of dots). (B) Corresponding waveforms superimposed. (C) Screenshot of the navigation game of the backyard (BY) environment. (D) The directional tuning of the cell. (E) Spatial firing rate map of the single putative neuron. (F) Corresponding spatial autocorrelogram with the cardinal angles of the grid spokes. Rotation symmetry is ~90°. Scales are in [m].

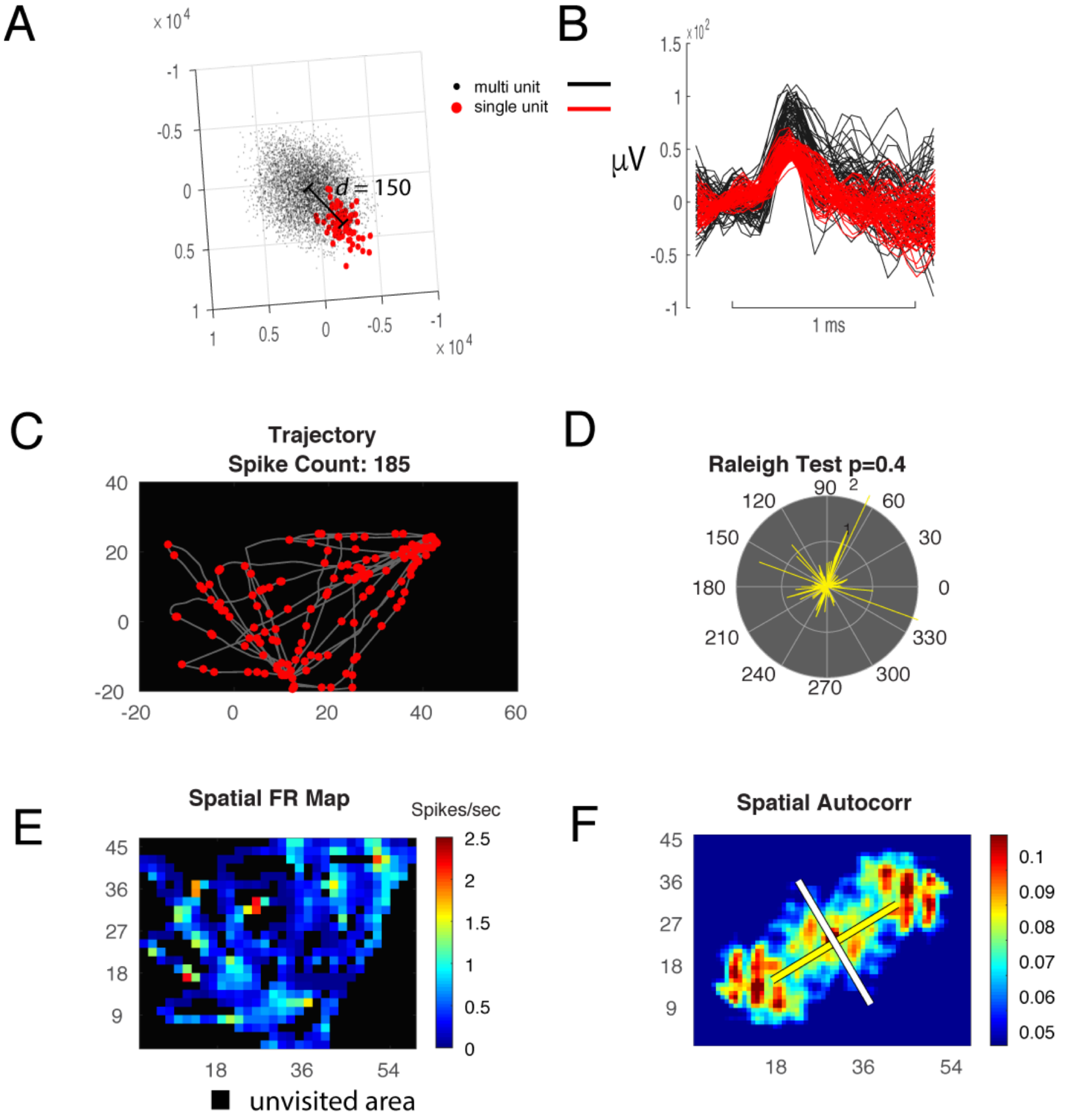

Bin size: 1.8x1.8m, Grid dist: 16.7908m, Grid Angle: 32.4123   Avg FR: 0.6297   Max FR: 11.236
spokes: 1   Spoke Angles: 87.0000   Peaks: 7   Grid conf: -0.0923   Grid sign: 1

Fig. S26. Example cell #15. The organization of the panels is similar to Fig. S11 except panel (D) featuring the directional tuning of the single unit activity. (A) The spike waveform cluster revealed a single unit (red dots) separated from multiunit activity (black cloud of dots). (B) Corresponding waveforms of the single unit and multi-unit activity superimposed. (C) Spikes overlaid on the trajectory of navigation in the LV environment. (D) The directional tuning of the cell. (E) Spatial firing rate map of the single unit activity. (F) Corresponding spatial autocorrelogram with the cardinal angles of the grid spokes. Rotation symmetry is 87°. Scales are in [m].

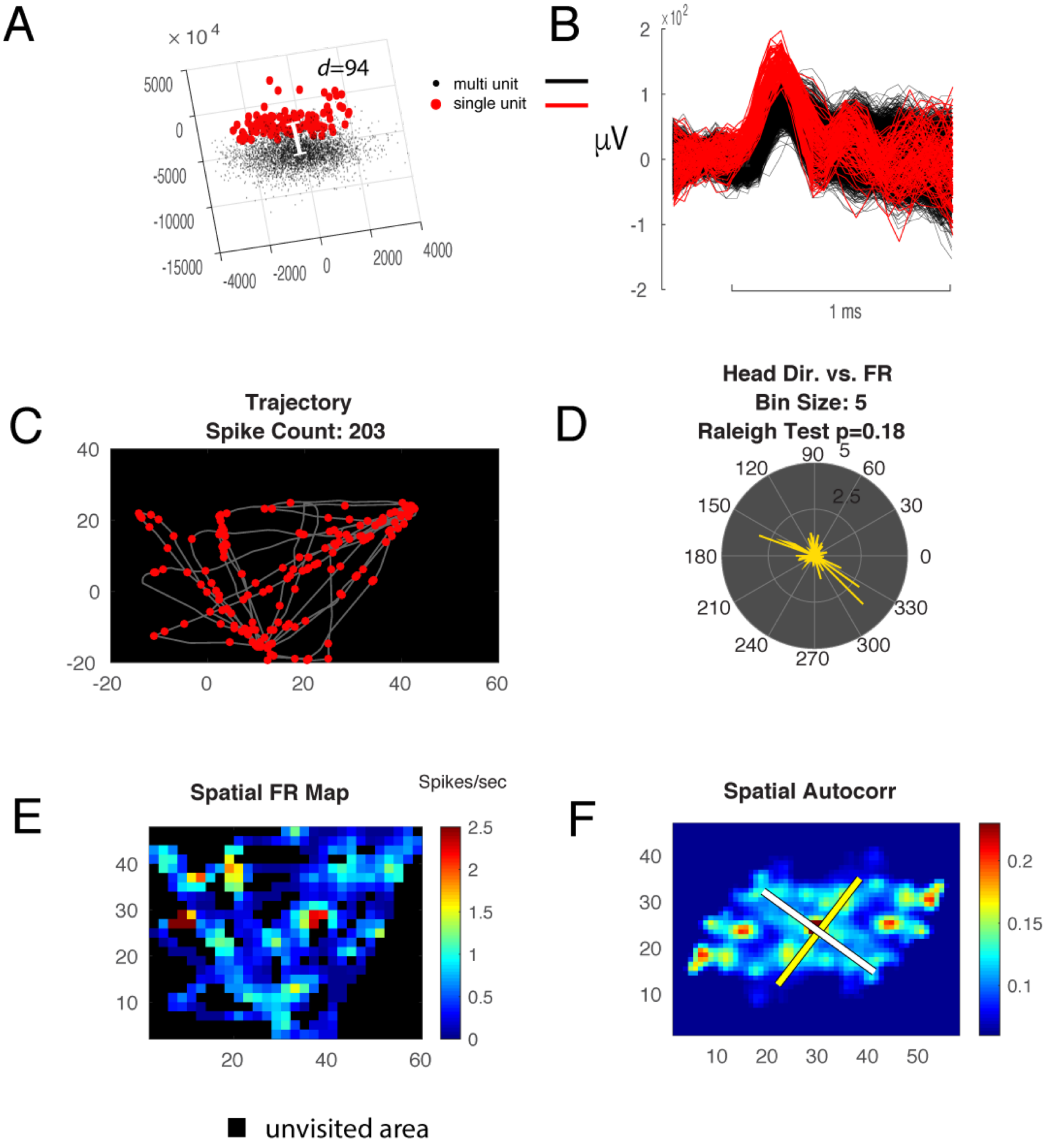

Bin Size: 2x2m, Grid dist: 14.0910m, Grid Angle: 54.6987 Avg FR: 0.69097 Max FR: 30.303

spokes: 1 Spoke Angles: 87.0000 Peaks: 10 Grid conf: -0.1149 Grid sign: 1

Fig. S27. Example cell #16. The organization of the panels is the same as that of Fig. S25. (A) The spike waveform clusters of single unit (red dots) separated from multiunit activity (black cloud of dots). (B) Corresponding waveforms of the single unit and multi-unit activity superimposed. (C) Spikes (red filled symbols) overlaid on the trajectory of navigation in the LV environment. (D) The heading directional tuning of the cell. (E) Spatial firing rate map of the single unit activity. (F) Corresponding spatial autocorrelogram with the cardinal angles of the grid spokes. Rotation symmetry is 87°. Scales are in [m].

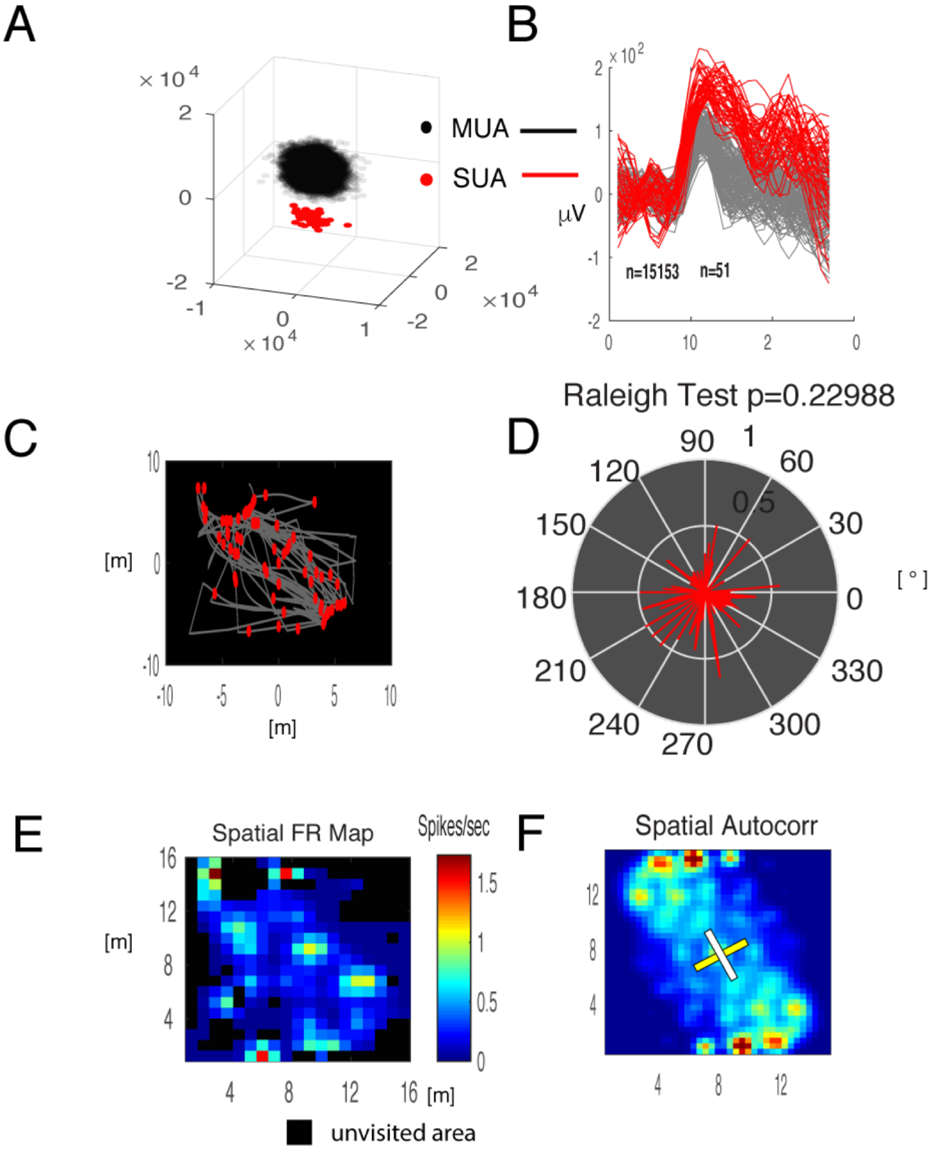

Bin Size: 0.8x0.8m, Grid dist: 4.2615m, Grid Angle: 29.7449   Avg FR: 0.26161   Max FR: 6.8027

Grid Modulation: -0.3603   Grid Spokes: 1   Spoke Angles: 87.0000   Peaks: 4   Grid conf: 0.005   Grid sign: 1

Fig. S28. Example cell #17. The organization of the panels is the same as that of Fig. S24. (A) The spike waveform clustering revealed a single unit (red dots) separated from multiunit activity and noise (black cloud of dots). (B) Corresponding waveforms superimposed. (C) The trajectories of 5 min virtual navigation in the backyard (BY) environment. The firing locations of the SUA projected on the layout of the environment. Red filled symbols represent SUA, gray line is the path taken. (D) The directional tuning of the cell. (E) Spatial firing rate map of the single putative neuron. (F) Corresponding spatial autocorrelogram with the cardinal angles of the grid spokes. Rotation symmetry is ~87°. Scales are in [m].

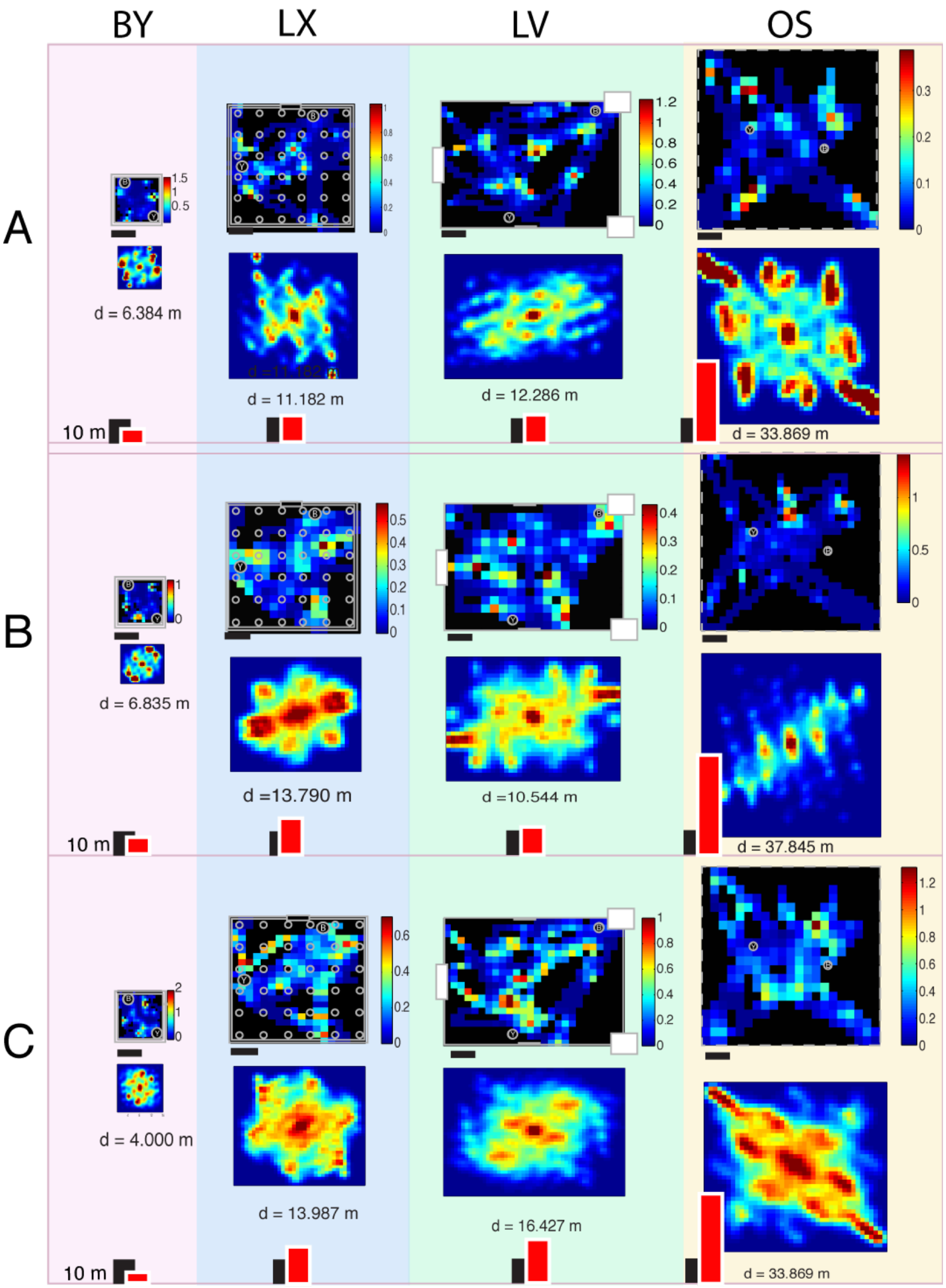

Fig. S29. Examples for scaling of grid distance by environment size. (a-c) Three representative neurons are shown to illustrate the scaling effect on grid sizes in response to exposure to four different environments. The upper rows represent firing rate maps color coded, lower lows heat-maps represent the autocorrelograms computed from the firing rate maps, also color coded (red indicate high autocorrelations). Panels from left to right correspond with the four environments: backyard (BY), Luxor (LX), Louvre (LV) and open environment (OS). The size and aspect rations of the maps proportional to the size of the virtual environments. Red bars under each main panel represent the average grid distance computed from the autocorrelograms relative to a 10 m black reference bar adjacent to them. Grid distances are also indicated numerically.

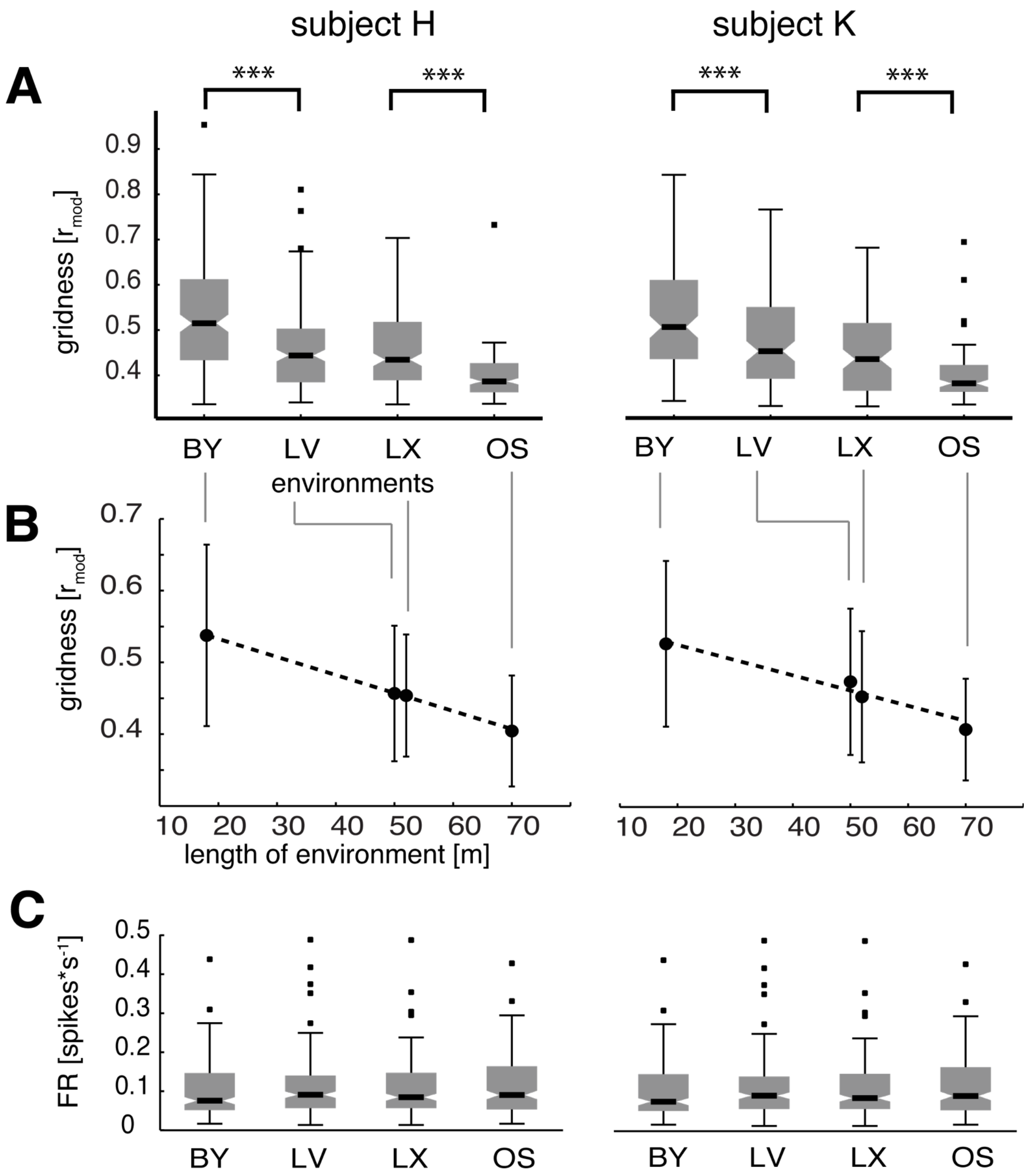

Fig. S30. Variation of gridness and firing rate in the SPC dataset across environments. (A) Gridness decreases with the size of environment. The environments are listed from the smallest (BY=backyard) to the largest (OS=open space). Gridness significantly differs between BY and LV and LX and OS but not between LV and LX (N_{subjH}=384, N_{subjK}=229 segments). (B) The correlation between gridness and the shortest dimension of the environment. Filled symbols represent mean gridness over all days and recordings from the given subject. Both subjects' data displayed significant ($p<0.0001$) negative correlations between gridness and environment size. Dashed lines represent the linear regression model. (C) The average firing rate of cells from recordings during navigation in each of the four environments (complete dataset, N_{subjH}=389, N_{subjK}=435 segments). Dots represent outlier data points.

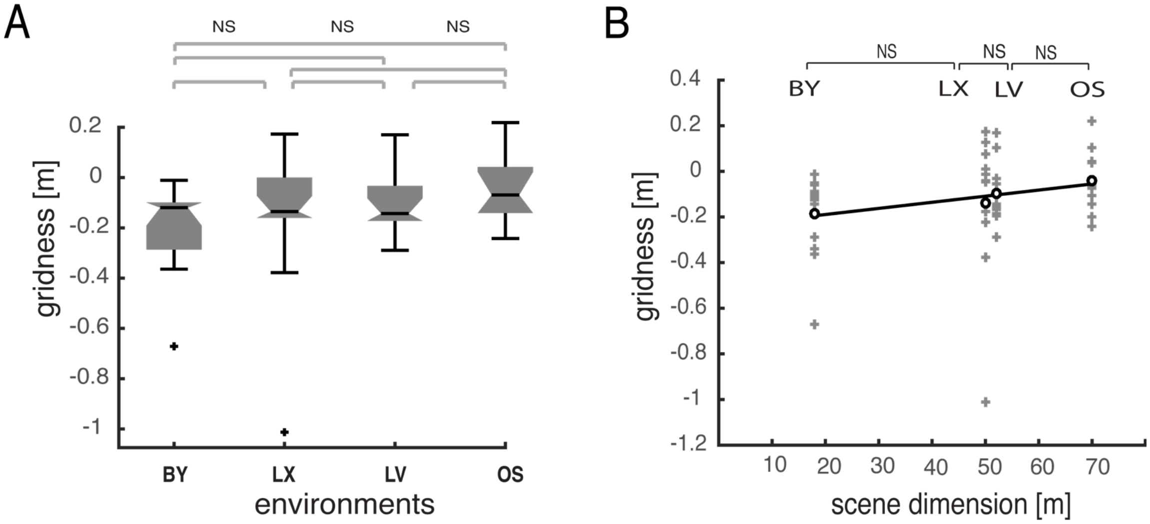

Fig. S31. Variation of gridness across environments in the PGC dataset. (A) Gridness scores grouped according to environments. The environments are arranged according to increasing sizes from the smallest BY (backyard) to the largest OS (open space). Gridness scores were unaffected by the environments. Data were combined from the two subjects (N_{cells}=73 $N_{segments}$=292). (B) Gridness scores as a function of the environment size. Open circles represent mean gridness combined from all days and recordings from both given subjects. Single '+' symbols represent the gridness of a cell recorded in a session within one environment. No significant correlation was observed between gridness and environment size (NS= no significant difference; N_{cells}=73; $N_{segments}$=292). Solid line represents the linear regression model.

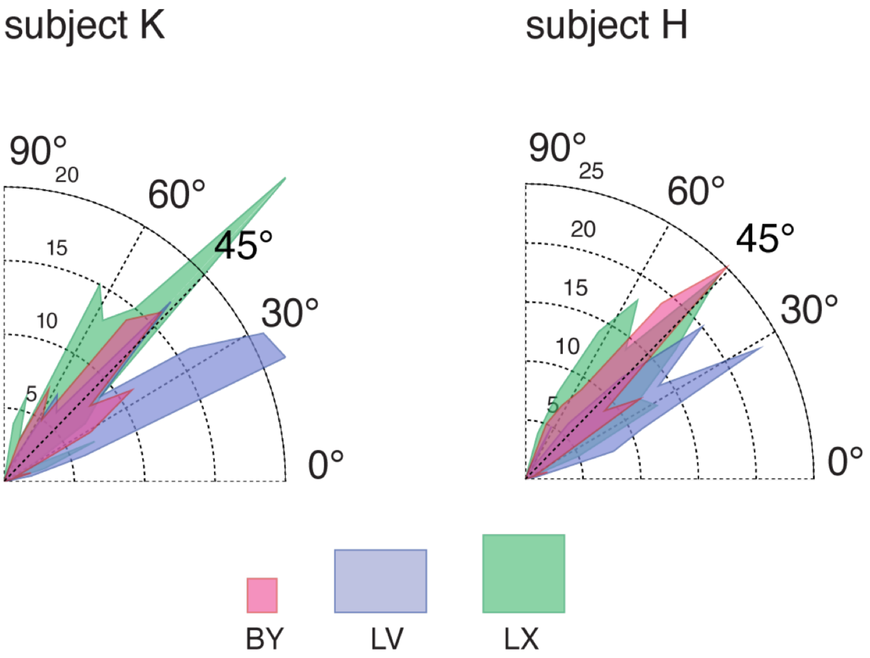

Fig. S32. Polar histograms of grid orientations from the population of SPC neurons from the two subjects. Average grid orientations per sessions combined across days from subject K (left) and subject H (right). Colors correspond to different environments. Note the clusters of angles near 30º, 45º, and 60º. (n_K=376 and n_H=311, Supplemental Table 7.1).

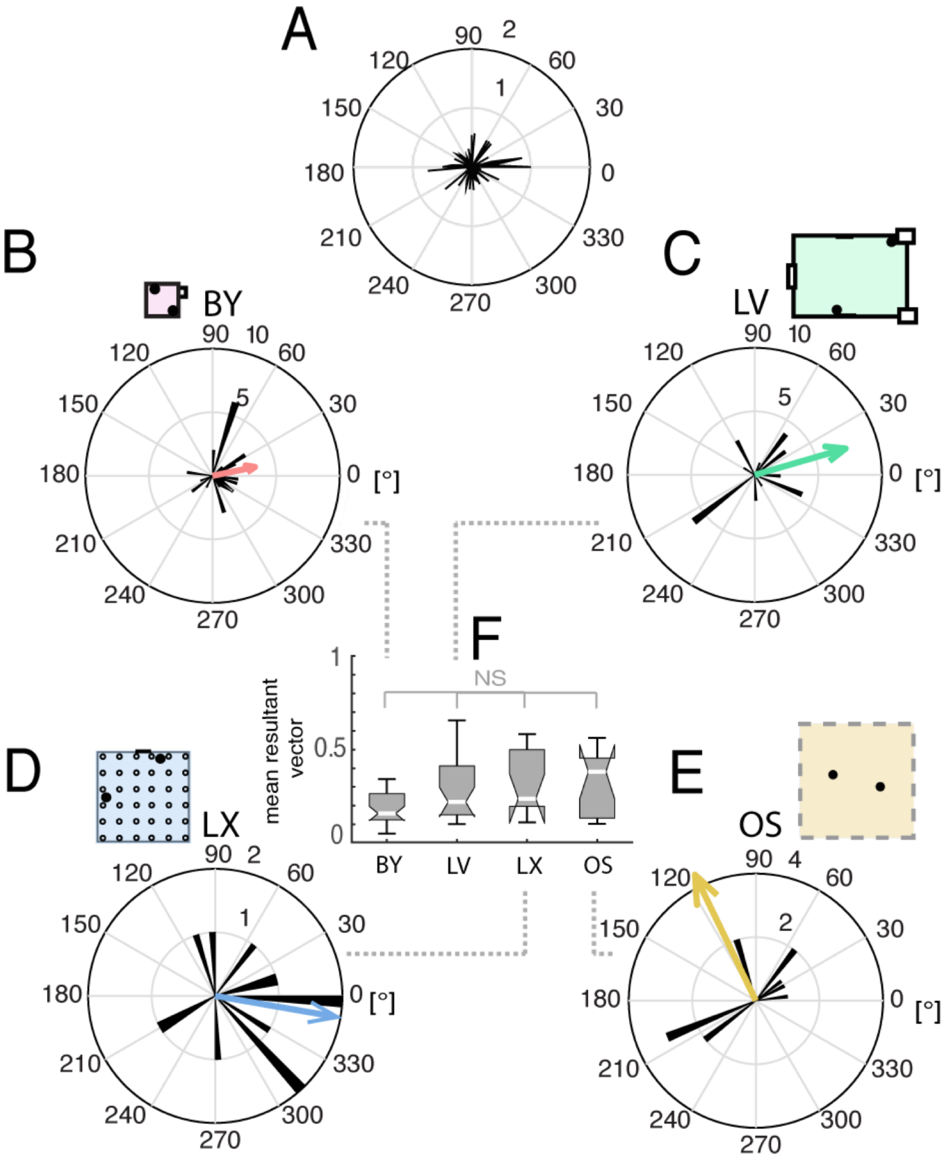

Fig. S33. Direction tuning of neurons across from the PGC$_{\text{hi-conf}}$ dataset across environments. (Data from subject H.) (A) Direction tuning of a neuron from the pPGC dataset during navigation in the BY environment. (B-E) Circular histograms represent the distributions of the mean preferred direction of neurons sorted according to environments and combined over days. The arrows in color represent the mean resultant vectors. The relative length of the arrow proportional to the strength of direction tuning and inversely proportional to the dispersion of directions around the mean. (F) The boxplots represent the mean resultant vectors on the scale of 0 to 1. The differences in mean directions between environments were not significant (ANOVA $F_{(3,81)}$=0.1616, $P_{(n=85)}$= .9219).

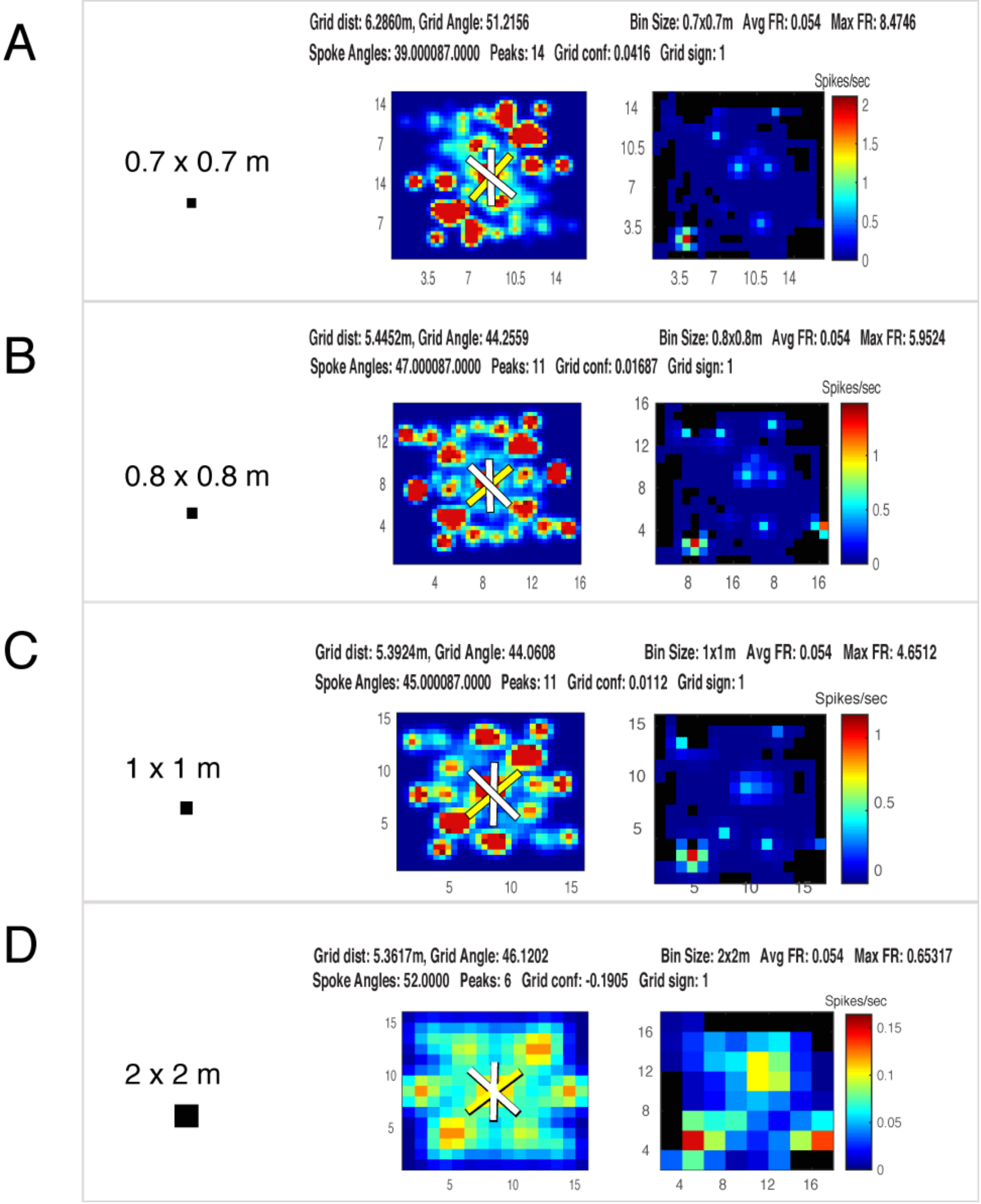

Fig. S34. Effect of spatial binning on grid parameters. A randomly chosen cell was tested by applying different bin sizes from .7 x .7 m to 2.0 x 2.0 m for spatial averaging of firing rates (A-D) Featured are the spatial autocorrelograms (left) and corresponding firing rate maps (right), according to four different bin sizes. While firing rate maps and autocorrelograms graphically change with different bin sizes, the quantitative descriptions of autocorrelograms retain similar values of grid distance (5.3 - 6.2 m), grid orientation (44 - 50º) and grid rotational symmetry (39 - 52º). The exact grid parameters are listed above the panels.

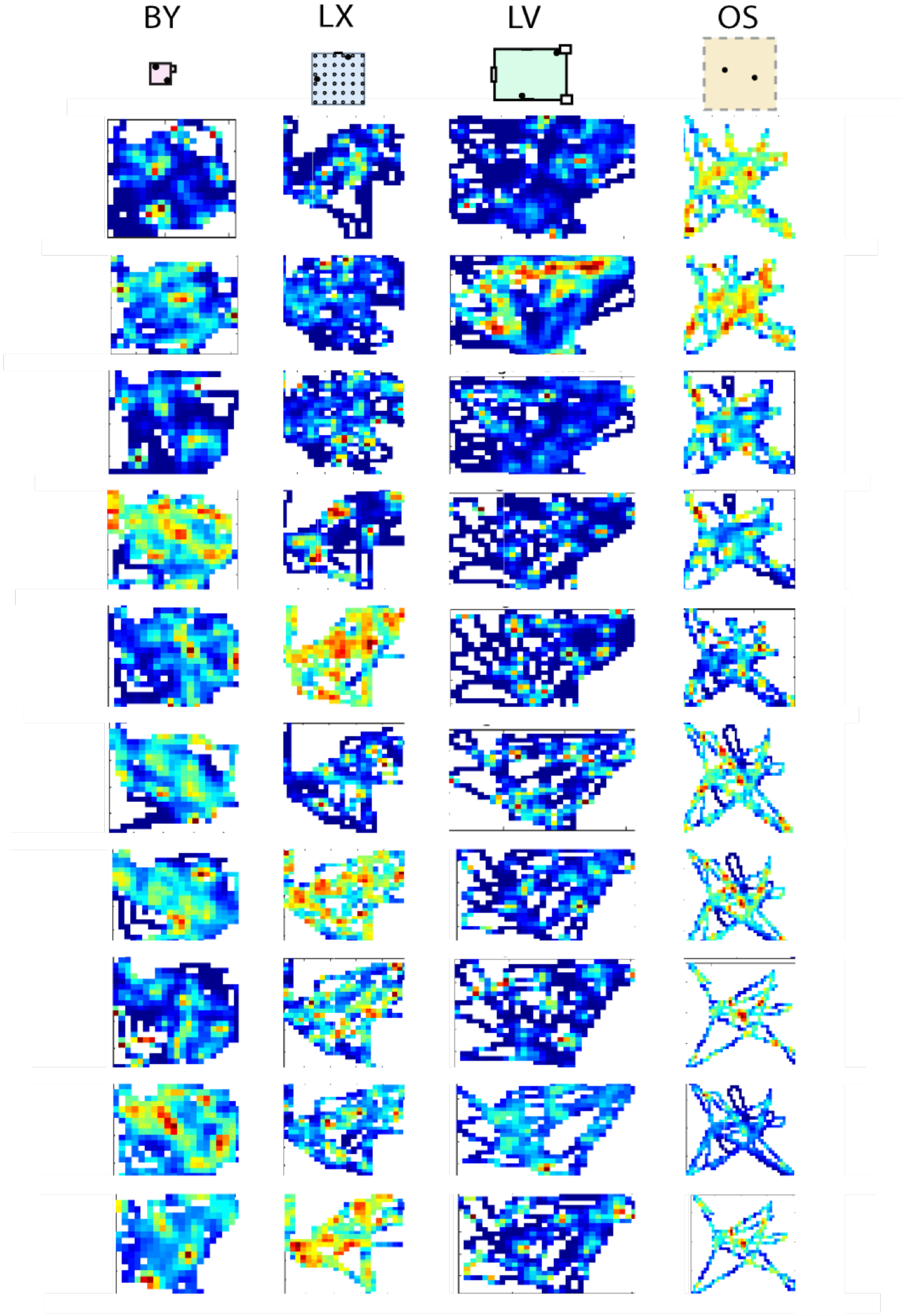

Fig. S35. Examples of single unit activity with spatially periodic activity (SPC). The figure illustrates the firing rate maps of randomly selected examples from the SPC dataset. Each of these examples passed the test of significant spatial periodicity, however may not be included in the PGC category. The examples are organized in columns according to environments. Each heat-map represent the firing rate of single unit activity associated with individual neurons. Firing rates were computed based on 5 min navigation trials in each environment. Color-scale is normalized to the range of the neuron's firing rate.

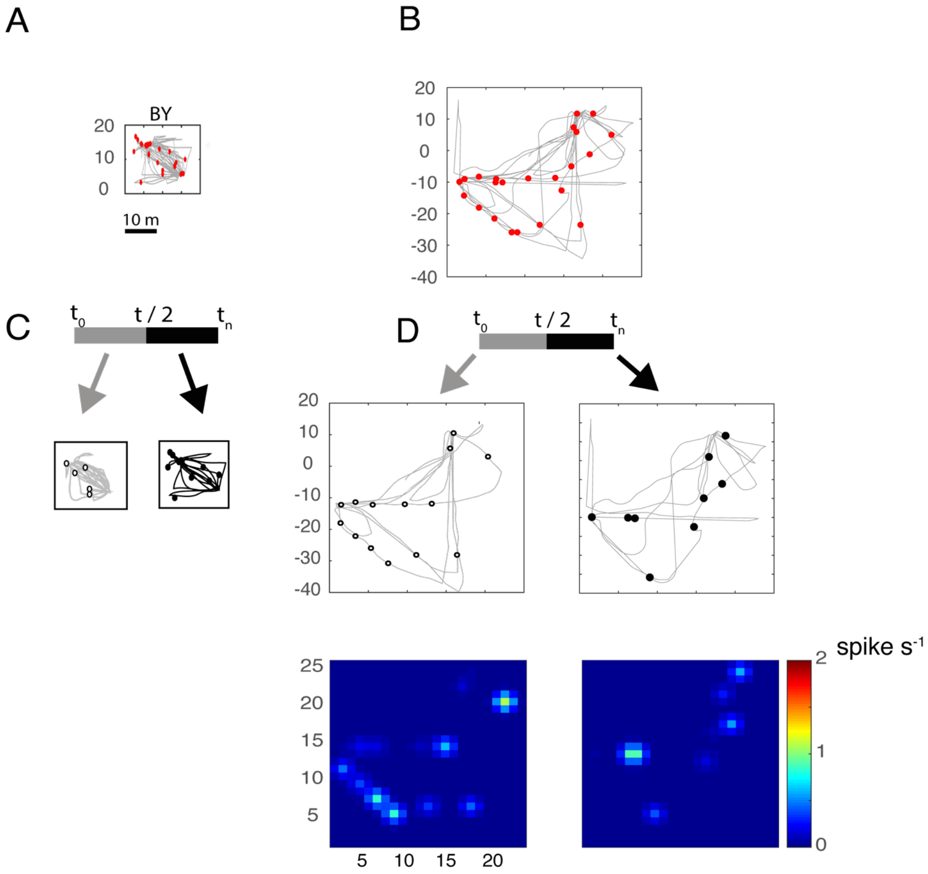

Fig. S36. Example for high spatial coherence and low cross-validation of spatial firing. (A) The spatial mapping of a low-firing-rate single unit activity (0.033 $spike*s^{-1}$) recorded in the BY and LX environments. Note that the single spikes were elicited highly regularly at vertices of a grid-like metric. (C, D) Cross-validation of the firing rate maps of this neuron by grouping the spikes to two equal and non-overlapping intervals according to the gray-black scheme above the left and right panels resulted in non-overlapping firing rate maps. Despite the regular spacing of the firing pattern of the neuron during both intervals, the two firing rate maps display no correlation ($n_{spikes}=23$, $r=-0.0632$, $p>0.05$).

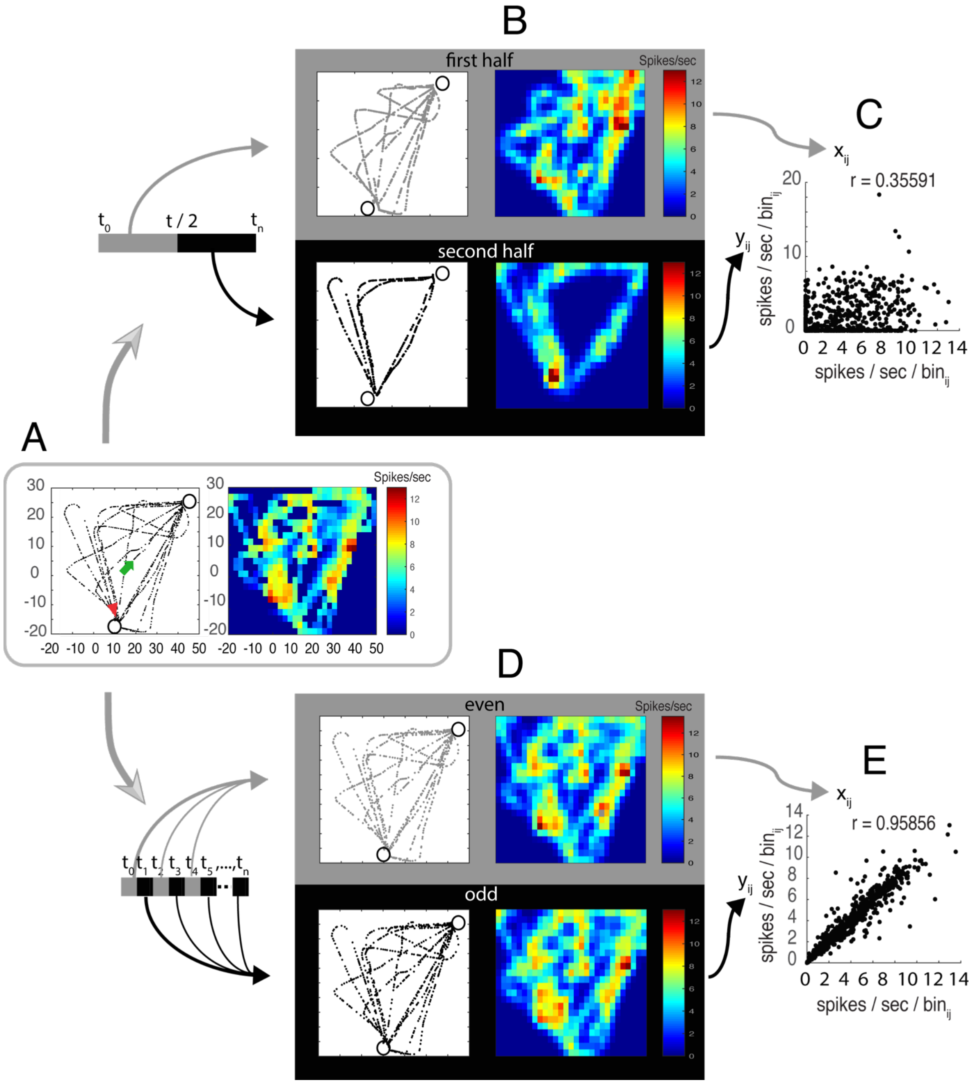

Fig. S37. Two-fold cross-validation and stationarity analysis for testing stability of grids. The two types of stability assessment methods are compared on a putative grid cell example. (A) Trajectory of the avatar in the LV environment during a 5 min navigation session (left panel) and the corresponding firing rate map of a putative grid cell (right panel). (Green arrow: start of path; red arrowhead: end of path; circles: spaceships). (B) The two-fold cross-validation of firing rate maps is shown by splitting data into two equal time intervals symbolized by the half-gray and half-black bar. Panels are arranged as in (A). Panels in gray and black frames represent the trajectory and firing rate map during the first 2.5 minutes and second 2.5 minutes of navigation, respectively. (C) The firing rates in corresponding spatial bins during the first and second intervals are plotted as filled symbols with their (x_{ij}) and (y_{ij}) coordinates, respectively. The Pearson's correlation coefficient is indicated by *r*. (D) Stationarity analysis: the same single unit activity as featured in (A) was temporally sorted and grouped according to even and odd numbered spikes. After grouping, we computed firing rate maps (right panels) separately from the even group (gray) and the odd group (black). Trajectories represent the corresponding path segments. (E) Same representation as in (C), except firing rates in corresponding bins were calculated from odd and even numbered spikes in (D) and plotted as x_{ij} and y_{ij}, respectively. Firing rates were compensated by the 50% subsampling of spikes to match original firing rates. Pearson's *r* is indicated. While both cross-validation and stationarity analysis resulted in highly significant correlations ($p < .00001$), the former in this example resulted in a modest correlation relative to the high correlation of stationarity. The explanation for this discrepancy is in the trajectories. The trajectories of the first and the second half are less overlapping than those of associated with odd and even spikes. See Fig. S5F,G for the population-level cross-validation and stationarity analysis.